Elucidating the Structural Dynamics of SERCA-PLB Regulation by Electron Paramagnetic Resonance

A DISSERTATION
SUBMITTED TO THE FACULTY OF THE GRADUATE SCHOOL
OF THE UNIVERSITY OF MINNESOTA
BY

Jesse Earl McCaffrey

IN PARTIAL FULFILLMENT OF THE REQUIREMENTS
FOR THE DEGREE OF
DOCTOR OF PHILOSOPHY

David D. Thomas, Advisor

August 2014

Acknowledgements

I have been very fortunate to work alongside many talented and exceptional people, who have helped me navigate the transition from physicist to biophysicist. **Dave Thomas**, the leader of our merry band, is a role model by every definition of the term. He has shown me what a physicist can accomplish in biochemistry, with his dedication to well-designed experiments, thorough data analysis, and physical models to explain biochemical observations. I remember sitting in his office on the first day, looking at structures of myosin and SERCA, and being told that his group was going to cure heart disease and muscular dystrophy by using spectroscopy to show how these proteins work on the molecular level. That was a defining moment in my career; I realized that with biophysics, I could really contribute to something that would help people. He has consistently challenged me to become a more thoughtful, aware, and critical scientist, supplying me with all the resources I could need to be successful.

Zach James has been my mentor, teaching me so much about EPR and biochemistry. He is one of the most thorough and innovative scientists I know, and I have always thought his dedicated criticism pairs well with my unbridled optimism. Working together, we achieved so much, experiencing moments of great joy and frustration, and perhaps keeping each other driven for the next experiment. We also spent a great time discussing and debating a variety of topics, from the essence of tasting to our role in the universe. Neither of us ever conceded an argument, but perhaps we learned to appreciate the other side a little bit more. He personally and professionally inspires me, and I am grateful for our friendship.

Ji Li is my fellow physicist in the lab, constantly reminding me of where I have come from. When I have a question about thermodynamics or electrodynamics, he is the first person I consult. He truly enjoys his work, thinking about what all these tiny microscopic proteins are really doing, and is never afraid to tackle complex problems. His 2012 JMB paper is among my all-time favorites; using electrostatics to perturb protein structure is elegant and creative. It's also been fascinating to discuss his experiences as a new father; he really loves watching that little kid do the simplest things.

Octavian Cornea is our lab administrator, and he keeps our lab functioning on a daily basis. He has helped me submit papers, grant applications, troubleshoot program/ network problems, and fill out lots of paperwork. But more than that, he is a great friend, and has given me excellent advice on how to live a good life. Eat well, take care of your body, don't be reluctant to spend your money on the good things, and always remember your priorities. Maybe I'll have as much wisdom as you…when I'm 80-something.

Gianluigi Veglia leads a laboratory that we often collaborate with, and he has been giving me guidance (and a hard time) since the beginning of my graduate career. Learning NMR from a biophysicist trained in chemistry enhanced my understanding of EPR immensely. He has always reminded me that the proteins we study are way more complicated than we might believe, and that I should take the time to truly enjoy my work and explore all of its mysteries. I will never forget his teaching advice: "push students like you'd test drive a Ferrari."

Vincent Noireaux introduced me to the world of biophysics when I took his course, "Introduction to Biopolymer Physics". I was amazed and amused that I could use

basic physics principles like rotational inertia and electrostatics to describe motion at the molecular level. Vincent shares a healthy passion for his research, and did well in guiding me through my graduate career.

Yuichi Kubota was my undergraduate quantum mechanics professor, and continued as a mentor when I entered the graduate program. He was always willing to listen to me grumble about graduate school research, and give me advice that challenged my perspective. He helped me overcome some difficult obstacles, and I am happy now to think of him not only as an instructor, but as a friend.

Several lab veterans were kind enough to train a new student (me) who initially knew nothing about biochemistry except how to poorly run a gel. **Elizabeth Lockamy**, thanks for teaching me how to perform BCAs, activity assays, FRET measurements, and perhaps most importantly, how to survive in the DDT lab. **Kurt Torgersen**, thanks for passing me the EPR baton, and letting me pick it up after dropping it a few times. **Yuri Nesmelov**, thanks for knowing pretty much everything about EPR, especially the things I can't look up through Google Scholar. **Andrew Thompson**, thanks for being the stand-in EPR expert and reminding me how slowly I bike. **Roman Agafonov**, thanks for teaching me to never stop asking why, at least until everyone gets annoyed. **Ryan Mello**, thanks for showing me how to teach EPR to novices. **Greg Gillispie**, thanks for sharing your wisdom on science and life, and the running stories. **Mike Autry**, thanks for being a living encyclopedia and answering every SERCA-PLB question I could possibly ask of you.

I managed to make some friends on other sides of the laboratory as well. **Simon Gruber**, possibly the most laid-back and confident oral presenters I know, with the knowledge to back it up. He explained any fluorescence or cell culture question I had, and knows about every current event I want to discuss. **Daphne Dong** was the frequent target of my well-intentioned teasing, and is an expert in activity assays and PLB phosphorylation. **Megan McCarthy** was a new addition to the lab, encouraging me to eat better (though it didn't work) and to be more decisive in presenting data. **Holly Langer**, thanks for being a great lifetime friend, and someone who was always up for a lunchtime adventure.

The lab continued to be stocked with supplies thanks to several undergrads: **Allison Raney**, **Corrin Laposki**, and **Lindsay Nevalainen**. Our lab manager, **Sarah Blakely** controlled all of them and let me buy anything I needed for my experiments. Plus, she formally hired me, so thanks for that.

And thanks to you, the reader, for going on this 155 page journey with me. ✈

Dedication

To Micki, Todd, Emil, Sharon, Renee, Geigs, Terry, and Ceri.
Thanks for supporting me with all of your love.

"If you grit your teeth and show real determination, you'll always have a chance."
Charles M. Schulz

Abstract

Muscle contraction and relaxation is initiated by changes in intracellular calcium, making adequate calcium transport essential for proper muscle function. A primary calcium transporter is the sarcoendoplasmic reticulum Ca^{2+}-ATPase (SERCA), located within the muscle cell and embedded in an organelle called the sarcoplasmic reticulum (SR). To facilitate muscle relaxation, calcium is sequestered from the cellular cytosol into the SR by SERCA. In cardiac muscle, enhanced regulation of calcium transport is needed to accommodate β-adrenergic stimulation (adrenaline demand), which is provided by the regulatory protein phospholamban (PLB). PLB binds to SERCA and inhibits calcium transport through reduction in calcium affinity. However, a phosphate group can be attached to PLB during adrenaline response (phosphorylation) which relieves PLB's inhibitory effect. The structural mechanisms for SERCA regulation by PLB, particularly with respect to phosphorylation, are not well-resolved. Under the Dissociation Model, PLB phosphorylation relieves SERCA inhibition by dissociating the SERCA-PLB complex. In contrast, the Subunit Model proposes that SERCA inhibition is relieved by a subtle structural change, where the SERCA-PLB complex is preserved.

The primary goal of my thesis work is to elucidate the structural mechanisms of the SERCA-PLB complex using electron paramagnetic resonance (EPR) spectroscopy. The first study (Chapter 3) aims to discriminate between the Dissociation and Subunit models by measuring changes in the rotational diffusion of EPR spin labels rigidly coupled to PLB and SERCA. The second study (Chapter 4) further develops an anisotropic membrane system called bicelles for EPR orientation measurements on PLB

and SERCA. The third study (Chapter 5) uses a combination of oriented bicelles and a novel rigid spin label (bifunctional spin label, or BSL) to measure PLB topology in the lipid membrane, with comparison to previous structural measurements by NMR and x-ray crystallography. Ongoing studies (Chapter 6) reconstitute both spin-labeled PLB and SERCA in bicelles to make PLB orientation measurements by EPR, as affected by PLB phosphorylation and binding of SERCA.

Table of Contents

List of Figures

List of Equations

List of Tables

List of Symbols and Abbreviations

5-DSA	5-DOXYL-stearic acid
A	actuator domain (SERCA)
AAV	adeno-associated virus
ADP	adenosine diphosphate
AFA	Cys36Ala & Cys41Phe & Cys46Ala (PLB Mutant)
ATP	adenosine triphosphate
BCA	bicinchonic assay
BSL	3,4-bis-(methanethiosulfonyl-methyl)-2,2,5,5-tetramethyl -2,5-dihydro-1h-pyrrol 1-yloxy spin label
C	center field peak height (STEPR)
$C_{12}E_8$	octaethylene glycol monododecyl ether
Ca^{2+}	calcium ion (+2 charge)
CaMKII	calcium/calmodulin-dependent protein kinase II
DCM	dilated cardiomyopathy
DHexPC	1,2-dihexanoyl-sn-glycero-3-phosphocholine
DMPC	1,2-dimyristoyl-sn-glycero-3-phosphocholine
DOPC	1,2-dioleoyl-*sn*-glycero-3-phosphocholine
DOPE	1,2-dioleoyl-sn-glycero-3-phosphoethanolamine
D_R	rotational diffusion rate constant
E	energy
E1	high calcium affinity state (SERCA)
E2	low calcium affinity state (SERCA)
EGTA	ethylene glycol tetraacetic acid
EPR	electron paramagnetic resonance
ESI-MS	electron spray ionization mass spectrometry
F	force
FRET	fluorescence resonance energy transfer
FTR	Förster transfer recovery
g	electron g factor
H	magnetic field strength or high field peak height (STEPR)
HEPES	4-(2-hydroxyethyl)-1-piperazineethanesulfonic acid
HPLC	high performance liquid chromatography
IASL	iodoacetamide spin label
ICM	ischemic cardiomyopathy
IPTG	isopropyl thiogalactose
I_{ST}	integrated intensity parameter (STEPR)
k_{Ca}	calcium concentration for half maximal activity
L/P	molar lipid to protein ratio
L	low field peak height (STEPR)
LC	long chain (lipid)
M	transmembrane domain (SERCA)
MOMD	microscopic order macroscopic disorder

MSL	maleimide spin label
MTSL	methanethiosulfonate spin label
N	nucleotide-binding domain (SERCA)
NCX	sodium calcium exchanger
NMR	nuclear magnetic resonance
P	phosphorylation domain (SERCA)
PKA	protein kinase A
PLB	phospholamban
PMCA	plasma membrane calcium adenosine triphosphatase
PO_4^{3-}	phosphate
POPC	1-palmitoyl-2-oleoyl-sn-glycero-3-phosphocholine
q	bicelle long chain / short chain lipid ratio
R	relaxed state (PLB)
RCF	relative centrifugal force
RyR	ryanodine receptor
S	order parameter
SC	short chain (lipid)
SDS	sodium dodecyl sulfate
SERCA	sarco(endo)plasmic reticulum calcium adenosine triphosphatase
SPPS	solid phase peptide synthesis
SR	sarcoplasmic reticulum
STEPR	saturation transfer EPR
T	hyperfine splitting constant or tense state (PLB)
T_1	spin-lattice relaxation time constant
T_2	spin-spin relaxation time constant
TM	transmembrane
TOAC	2,2,6,6-tetramethyl-N-oxyl-4-amino-4-carboxylic acid
V_1	derivative absorption first harmonic in-phase EPR
V_2'	derivative absorption second harmonic out-of-phase EPR
V_{max}	maximal ATPase activity
Δ_L	low field linewidth
β	Bohr magneton
β-OG	n-octyl-β-D-glucoside
μ	magnetic dipole moment
ν	radiation frequency
τ_{EX}	exchange time constant
τ_R	rotational correlation time

Chapter 1: Calcium-Regulated Muscle Physiology

1.1 Mechanics of Muscle Contractility

Muscle is a soft tissue present in most animals, and is responsible for executing motor function in the body. It is comprised of thin (actin) and thick (myosin) filaments that slide between each other, enabling the muscle to extend and contract as needed to accomplish movement. This is referred to as the sliding filament model, proposed in 1954 by Andrew and Hugh Huxley and co-workers [2, 3]. Specifically, myosin forms cross-

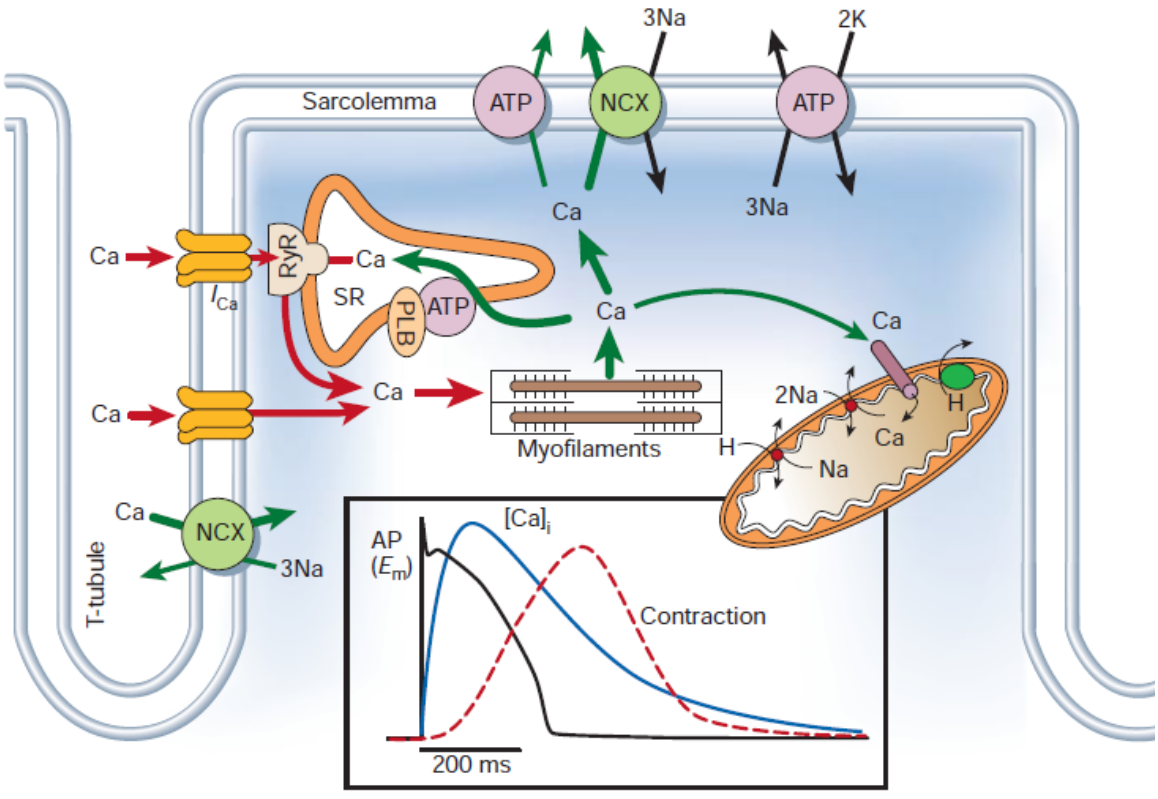

Fig. 1. Functional model of calcium transport. Calcium transported by the L-type calcium channels (I_{Ca} in figure) during action potential stimulates release of calcium from the sarcoplasmic reticulum (SR) by the ryanodine receptors (RyR) into the cellular cytosol, followed by myofilament contraction. To facilitate muscle relaxation, calcium is taken back into the SR by the calcium ATPase SERCA (ATP in figure), which is regulated by phospholamban (PLB). Figure reprinted from [1].

bridges with the actin filament, and through hydrolysis of adenosine triphosphate (ATP), undergoes conformational changes that contracts the muscle fiber [4]. The ability of myosin to bind to the actin filament is regulated by tropomyosin, a coiled coil protein which lines the actin filament, and may either block or reveal the myosin-binding sites on actin [5]. The troponin complex, comprised of troponin C, T, and I, regulates the position of tropomyosin on the actin filament. In particular, troponin I shifts conformation when calcium is bound to it, exposing the myosin binding sites and leading to muscle contraction [6]. Calcium is therefore an essential component of proper muscle contractility regulation.

1.2 Intracellular Calcium Transport

Free calcium (Ca^{2+}) is an essential signaling chemical for many biochemical processes, including bone production, programmed cell death, and muscle contractility [7]. Fig. 1 shows the essential components of intracellular calcium transport. Calcium is transported into the cell through the L-type calcium channel, located in the sarcolemmal t-tubules. The L-type calcium channel is voltage-dependent, responding to action potentials propagated across the sarcolemma. Calcium transported by the L-type calcium channel stimulates the ryanodine receptor (RyR), a calcium transporter embedded in the sarcoplasmic reticulum (SR), to release micromolar calcium from the SR into the cellular cytosol, activating calcium-dependent processes such as muscle contraction. To reverse these processes, calcium must be removed from the cytosol. It can be removed from the cell through the plasma membrane calcium ATPase (PMCA) and the sodium calcium

exchanger (NCX); however, 70% of calcium removal is accomplished by the sarco-endoplasmic reticulum calcium ATPase (SERCA) [8]. SERCA is embedded in the SR membrane, hydrolyzing ATP to pump calcium from the cytosol into the SR. In cardiac muscle cells, SERCA activity is allosterically regulated by phospholamban (PLB) [9, 10].

1.3 SERCA: The SR Calcium ATPase

SERCA is a P-type calcium ATPase, autophosphorylating during its catalytic cycle of hydrolyzing ATP to transport calcium from the cellular cytosol into the SR. It is embedded in the SR membrane, and is encoded by three genes: ATP2A1 (SERCA1), ATP2A2 (SERCA2), and ATP2A3 (SERCA3) [12]. SERCA1a is primarily expressed in fast-twitch skeletal muscle [13], SERCA2a is primarily expressed in cardiac and slow-twitch skeletal muscle [14], and SERCA3a is primarily expressed in non-muscle tissue such as epithelial and endothelial cells [15]. SERCA1a is well-studied due to its abundance and ease of purification. It is also ~84% homologous to the cardiac variant SERCA2a, and possesses similar interactions with PLB [16, 17]. The studies performed in this thesis use the SERCA1a isoform, purified from rabbit skeletal muscle, and SERCA1a will be referred to as SERCA subsequently.

SERCA comprises four structural domains (Fig. 2) [11]. The transmembrane (M) domain contains 10 TM helices (M1-M10), forming the calcium channel between the cytosol and SR, as well as the two calcium-binding sites. Site I is coordinated with Glu 771 (M5), Asp 800 (M6), Glu 908 (M8), Asp 768 (M5), Thr 799 (M6), as well as two water molecules. Site II is coordinated with Glu 309 (M4), Val 304 (M4), Ala 305 (M4),

Ile 307 (M4), Asp 800 (M6) and Asn 796 (M6) [12, 18]. The phosphorylation (P) domain is directly above the M domain. During SERCA's catalytic cycle, residue Asp356 is phosphorylated, inducing conformational changes within SERCA that facilitate calcium transport. The actuator (A) domain is adjacent to the P domain, and is responsible for translating calcium and phosphorylation-dependent conformational changes throughout SERCA. The nucleotide-binding (N) domain is above the P domain, containing the

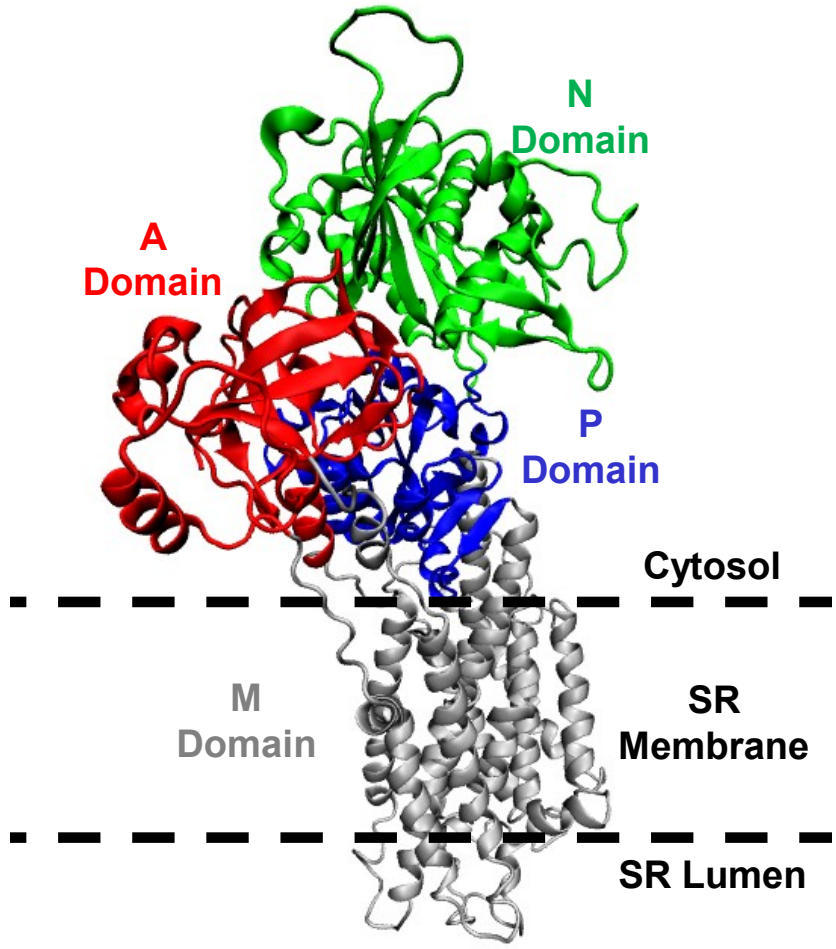

Fig. 2. SERCA1a E2 crystal structure (1IWO) [11]. SERCA is a calcium ATPase, hydrolyzing ATP to transport calcium ions from the cytoplasm into the SR. The transmembrane domain (M, grey) contains 11 transmembrane helices, forming the calcium channel and calcium binding sites. The nucleotide-binding domain (N, green) contains an ATP binding site near Phe 487 for ATP hydrolysis. The phosphorylation domain (P, blue) is autophosphorylated at Asp 351 during ATP hydrolysis. The actuator domain (A, red) facilitates structural transitions throughout SERCA during ATP hydrolysis for calcium transport.

ADP/ATP pocket formed by Phe 487, Lys 492, Lys 515, Thr 440, and Glu 442 [19].

The catalytic cycle of SERCA is comprised of biochemical states with low (E2) and high (E1) calcium affinities, as well as phosphorylated (P) states (Fig. 3). Starting

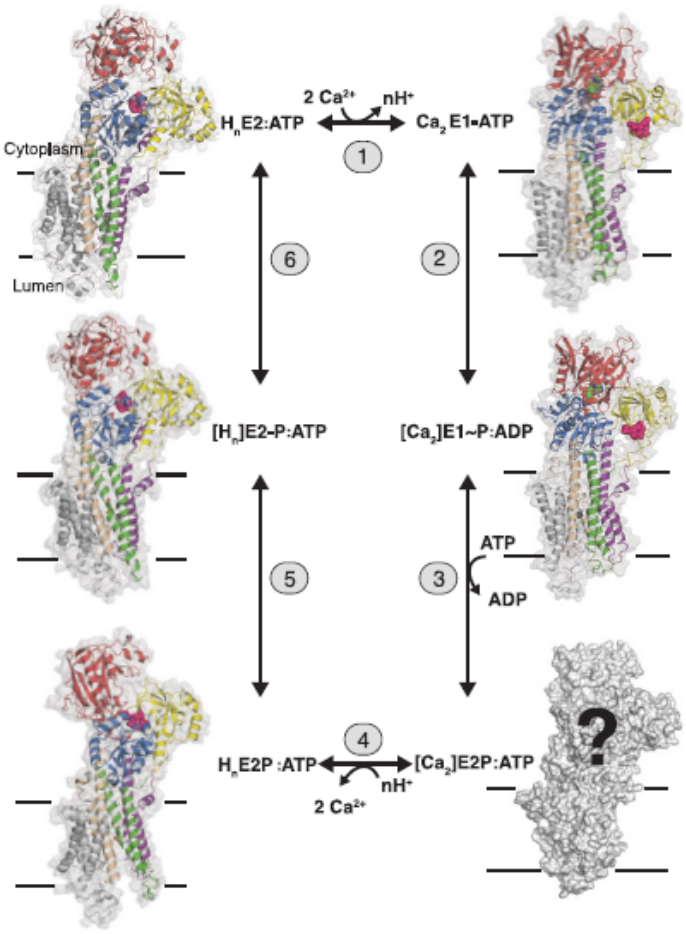

Fig. 3. SERCA enzymatic cycle. During its enzymatic cycle, SERCA binds calcium, transitioning from low calcium affinity E2 to the high calcium affinity E1. ATP is hydrolyzed and SERCA is autophosphorylated at Asp 351, reducing SERCA's calcium affinity. Calcium is then released into the SR, ADP is released, and SERCA is dephosphorylated. Figure reprinted from [12].

from the $[H_n]$E2-ATP state, two calcium ions bind to SERCA while protons from the previous cycle are expelled into the cytosol, forming the $[Ca_2]$E1-ATP state. Subsequent ATP hydrolysis causes SERCA phosphorylation at Asp351, forming the $[Ca_2]$E1P-ADP

state and shifting the TM helices to occlude Ca from the cytosol. Release of ADP and binding of ATP forms the [Ca_2]E2P-ATP state, where the TM helices open to the SR lumen. Now in a low-affinity calcium state, Ca is released from SERCA through the M domain into the SR in exchange for 2-3 protons ([H_n]E2P-ATP). Proton occlusion forms [H_n]E2-P-ATP, and subsequent release of the inorganic phosphate P_i (dephosphorylation) returns SERCA to the [H_n]E2-ATP state.

The structures corresponding to these biochemical states have slowly been determined, primarily by X-ray crystallography. The first high-resolution SERCA structure was determined by Chikashi Toyoshima and co-workers in the year 2000, using X-ray crystallography on crystals of SERCA in native SR in the calcium-bound state [20]. Subsequent work by Toyoshima, Poul Nissen, and others has crystallized SERCA in additional biochemical states, using calcium and inhibitors to stabilize those states. The end result is a high-resolution model for SERCA in each of its biochemical states, with the [Ca_2]E2P-ATP state recently determined by Jones and co-workers (Fig. 3) [21].

1.4 PLB: The Regulatory Peptide

PLB is a regulatory peptide consisting of 52 residues and three structural domains (Fig. 4) [10]. Domain Ia (residues 1-16) is a dynamic amphipathic helix at and above the SR membrane. It is connected by a highly dynamic loop region (residues 17-22) to a transmembrane helix that extends above the SR membrane surface (domain Ib, residues 23-30), and down to the bottom surface (domain II, residues 31-52). Domain Ib is also

dynamic, while domain II is restricted, exhibiting microsecond uniaxial rotational diffusion with minor nanosecond off-axial dynamics [23-26]. Domain Ia also contains three arginines, conferring +3 charge to PLB's amphipathic helix. This is known to influence protein-protein interactions and dynamics [27]. Domains Ib and II are electrically neutral (zwitterionic), while PLB retains a total +3 charge from domain Ia.

PLB also exists in multiple oligomeric, or self-associative, states (Fig. 5). The

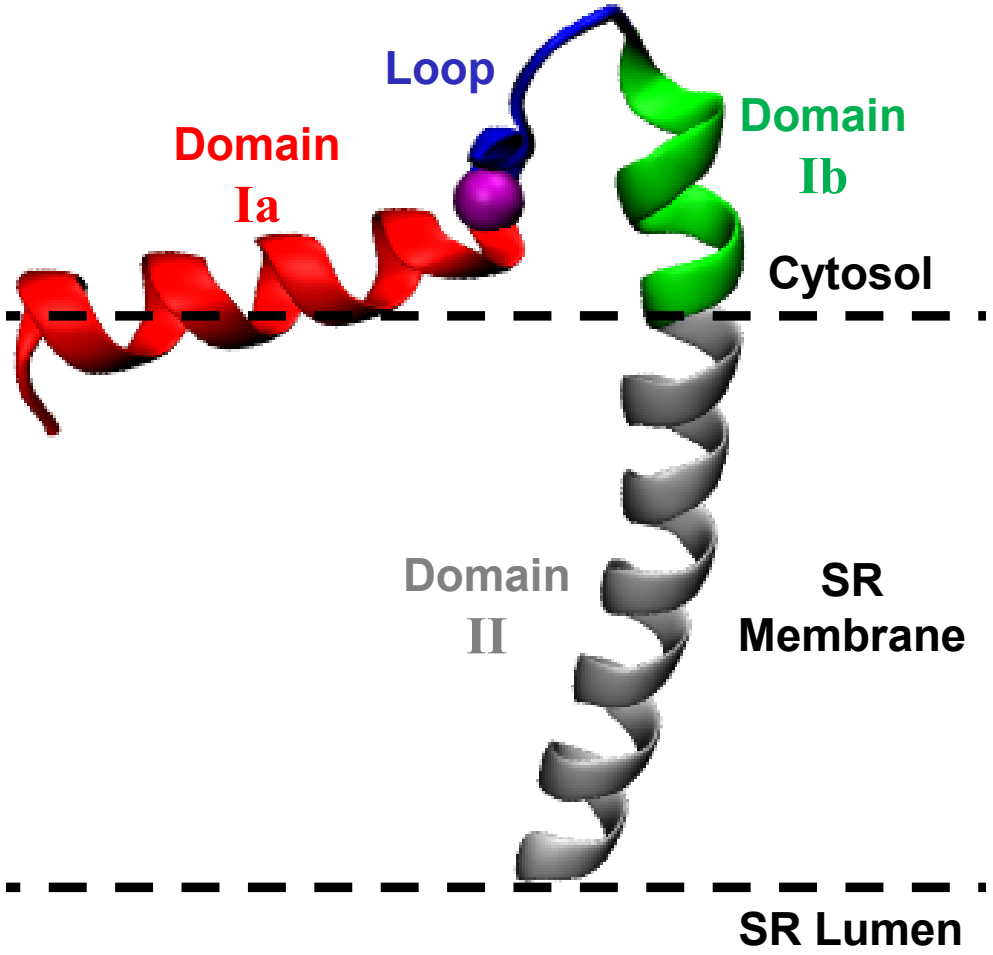

Fig. 4. PLB tense state high-resolution structure determined by hybrid NMR [22]. PLB is a single-pass transmembrane regulatory peptide. Domain Ia (residues 1-16, red) is α-helical and partially embedded in the SR membrane when PLB is in its ground state. An unstructured loop region (residues 17-22) connects domain Ia to domain Ib (residues 23-30), which is typically also α-helical. Domain II (residues 31-52) forms an α-helix spanning the SR membrane.

greatest populated of these states include the monomer, a single protomer of PLB, and the pentamer, containing five protomers of PLB [28-30]. While the PLB monomer is the primary inhibitor of SERCA [31], the pentamer functions as a reservoir for PLB protomers in the system [30, 32, 33]. The pentamer is stabilized by a number of leucine and isoleucine residues in domain II, forming a leucine/isoleucine zipper between adjacent PLB protomers [34]. This pentamer is relatively stable, requiring high temperature to dissociate in sodium dodecyl sulfate (SDS) gel electrophoresis [29]. PLB was measured to equilibrate between the monomer and pentamer on a timescale slower than minutes by Förster Transfer Recovery (FTR) [35]. To simplify PLB structural measurements, the monomeric mutant Cys36Ala/Cys41Phe/Cys46Ala (AFA) PLB is used to destabilize oligomeric interactions, while maintaining similar SERCA inhibitory potency [36].

An important post-translational modification to PLB is phosphorylation, where a phosphate group (PO_4^{3-}) is covalently attached to a residue [37, 38]. Phosphorylation can have dramatic effects on protein structure and dynamics, due to changes in electrostatics and hydrophobicity [39]. PLB is known to be phosphorylated at Ser16 by protein kinase A (PKA), and at Thr17 by Ca^{2+}/calmodulin-dependent protein kinase II (CaMKII) [40]. These site-dependent modifications are proposed to have distinct functional effects on PLB [41, 42]. In addition to altering the dynamics of the amphipathic helix [23, 25], Ser16 phosphorylation shifts the monomer-pentamer equilibrium towards the pentamer [30, 43, 44], and reduces PLB inhibitory potential [37, 38]

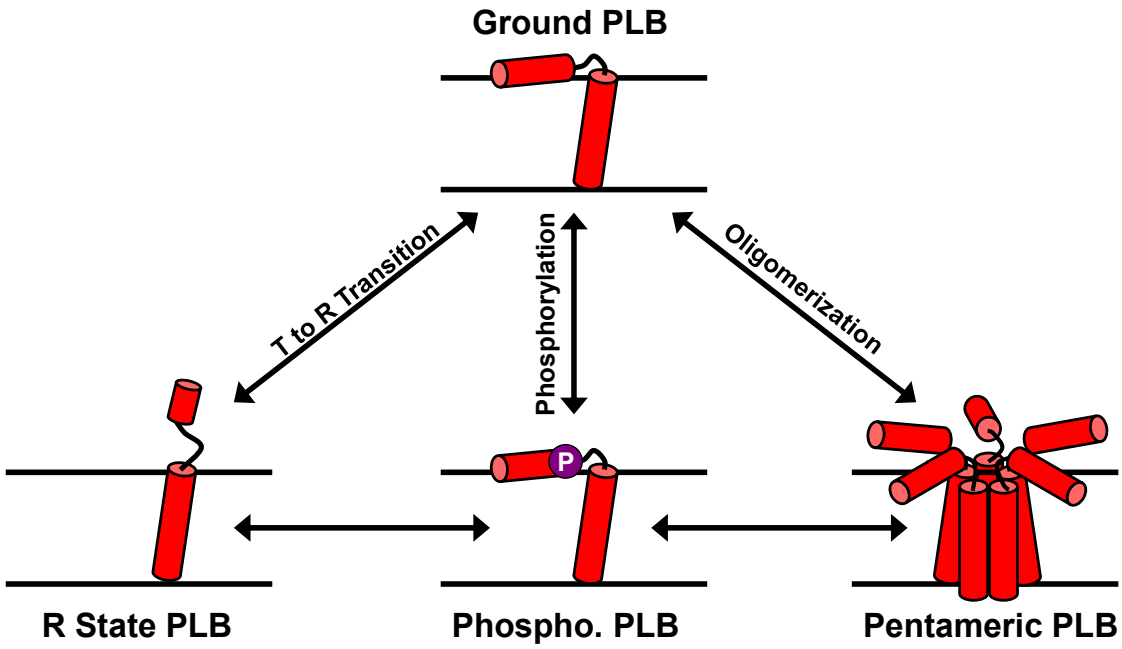

Fig. 5. Structural and biochemical states of PLB. The unphosphorylated, monomeric, T-state PLB is referred as the ground state (top, center). From this ground state, it may exchange into the R state (bottom, left), become phosphorylated at Ser16/Thr17 (bottom, center), or self-oligomerize into a pentamer (bottom, right). These are three distinct transitions that may occur exclusively or concurrently. For example, complete PLB phosphorylation increases the R state and pentamer populations, though unphosphorylated R-state and pentameric PLBs still exist in the system.

PLB also exists in several structural states, characterized primarily by the dynamics of the amphipathic helix (Fig. 5). In the rigid ***T*** state, the helix is partially embedded in the SR membrane, and is relatively immobile. In the contrasting ***R*** state, the helix is free above the SR membrane, and experiences large-amplitude nanosecond motion [25, 45, 46]. Partial unwinding of domains Ia and Ib are also observed in the ***R*** state, with relatively little change in domain II [26, 46, 47]. PLB is in equilibrium between the ***T*** and ***R*** states on the millisecond timescale [47]. Ser16 phosphorylation has been shown to shift the ***T-R*** equilibrium towards the ***R*** state [25, 45]. Recent NMR measurements by the Veglia laboratory suggest additional structural states, characterized by further unwinding of domains Ia and Ib [48, 49]. These are the excited states ***T′*** and ***R′***

for ***T*** and ***R***, respectively, and are observed to increase in population with increasing temperature and S16 phosphorylation [48, 49].

1.5 The SERCA-PLB Complex

PLB was first proposed as a regulator of SERCA in the mid-1970s primarily by Arnold Katz and co-workers, resulting from observations of increased SERCA activity after PKA-induced phosphorylation of cardiac SR containing SERCA and PLB [50].

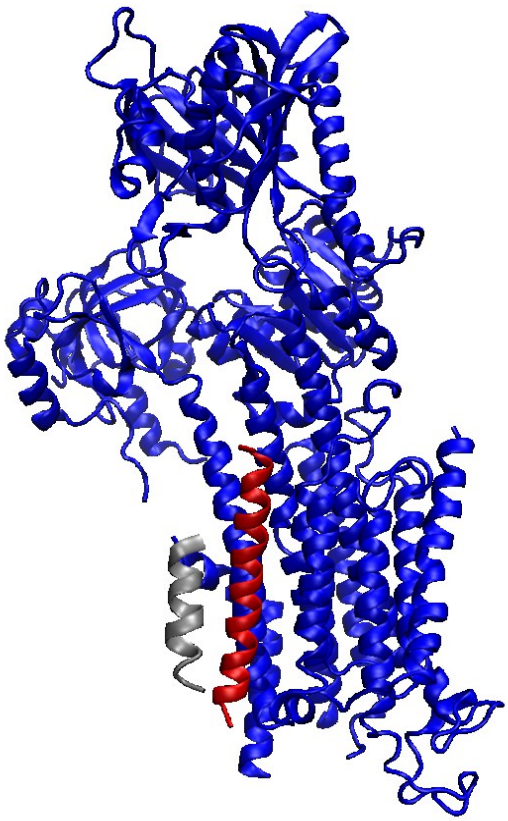

Fig. 6. SERCA-PLB crystal structure (4KYT) [21]. Larry Jones and co-workers co-crystallized rabbit SERCA1a with a superinhibitory mutant PLB4 (N27A, N30C, L37A, V49G) with increased binding affinity for SERCA in the E2 state without bound calcium. The protein density corresponding to SERCA1a (blue) is consistent with previous high-resolution SERCA structures [11, 51]. Density proposed to correspond to the PLB TM helix (red) is consistent with cross-linking studies [52, 53]. Grey density is not well-understood, and may correspond to domain Ia of PLB or the TM helix of another protein.

Since then, the functional consequences of PLB binding to SERCA have been well-elucidated [54, 55]. PLB reduces the apparent calcium affinity of SERCA, thereby inhibiting the rate of calcium transport across the SR membrane [56]. This inhibition can be relieved in two ways: (1) by additional calcium, which directly overcomes the reduction in calcium affinity, or (2) phosphorylation of PLB at Ser16 [38, 46]. While these effects are known functionally, the structural basis for their efficacy remains controversial. Cross-linking [57] and immunoprecipitation [51] experiments revealed a disruption in the SERCA's M domain PLB binding groove (M2, M4, M6, and M9) after added calcium or Ser16 phosphorylation of PLB by PKA, as well as decreased binding affinity. These results suggested a model where additional calcium or PLB phosphorylation causes a dissociation of the SERCA-PLB complex (Dissociation Model, [58]), thus relieving the inhibitory effects of PLB on SERCA and restoring maximum calcium affinity and transport. However, numerous fluorescence spectroscopic studies [59, 60] observe no significant change in distance between SERCA and domain Ia of PLB after added calcium or PLB phosphorylation, suggesting that the complex is preserved. EPR dynamics measurements of PLB's domain Ia in the presence of SERCA also find restricted motion after phosphorylation, suggesting a population where PLB remains bound to SERCA [25]. These observations are better explained by a model where additional calcium or PLB phosphorylation relieves inhibition by causing a subtle structural change within the SERCA-PLB complex, while PLB remains bound to SERCA as a subunit (Subunit Model). However, these spectroscopic measurements have not been made for PLB's TM helix, the site of SERCA inhibition.

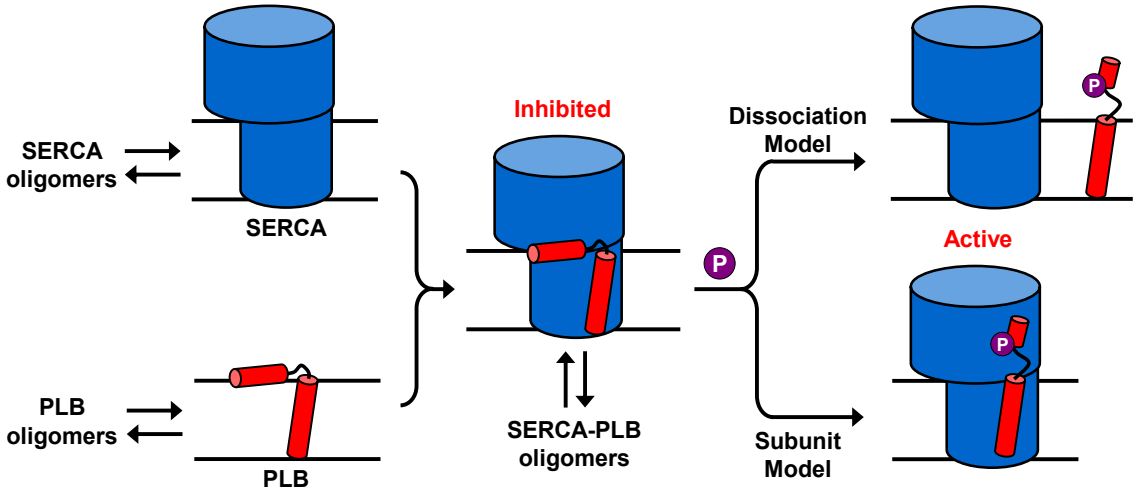

Fig. 7. Scheme for SERCA and PLB homo/hetero-oligomerization. Both SERCA (blue) and PLB (red) form homo-oligomers (left). SERCA and PLB also bind together to form an inhibited hetero-complex (center). This complex also forms its own homo-oligomers, further reducing SERCA activity. Phosphorylation of PLB in the SERCA-PLB restores activity, but the structural mechanism responsible for this relief of inhibition is not clear. In the proposed dissociation model, PLB phosphorylation causes dissociation of the complex (right, top). In the proposed subunit model, PLB phosphorylation causes a subtle structural change within the complex (right, bottom). Figure adapted from [61].

1.6 Physiological Relevance of the SERCA-PLB Complex

An important question to answer before launching into structural studies of the SERCA-PLB complex is, "Why is this research scientifically and socially relevant?" The answer is that understanding the structural mechanisms of calcium transport is essential for treating several debilitating conditions, including heart disease, muscular dystrophy, and diabetes. Fig. 8 shows data correlating decreased SERCA activity and SR calcium (likely due to inadequate SERCA function) with heart failure phenotypes [62, 63]. Studies in mice with muscular dystrophy (mdx) also demonstrate low SERCA activity and high cytosolic calcium [64, 65]. Obese and diabetic mice have insufficient SERCA, and respond poorly to additional glucose [66, 67]. In contrast, overexpression of SERCA

improves cardiac contractility in heart failure phenotype rats [68], reverses muscle degradation in mdx mice [69], and also improves cardiac contractility in diabetic mice [70].

Roger Hajjar has led an effort to overexpress SERCA in humans by intracoronary infusion of an adeno-associated viral (AAV) vector containing SERCA2a DNA (MYDICAR) [71-74]. This AAV treatment has proven successful in delaying death in animal heart failure models (rodent, pig, and sheep), and is currently being tested in Phase 1 and 2 clinical trials in humans (CUPID), with positive initial results. One year after percutaneous intracoronary injection of MYDICAR, parameters of cardiac contractility such as ejection fraction and VO_2 max are increased, with decreased incidence of complications leading to hospitalization [71, 74]. Despite the early success

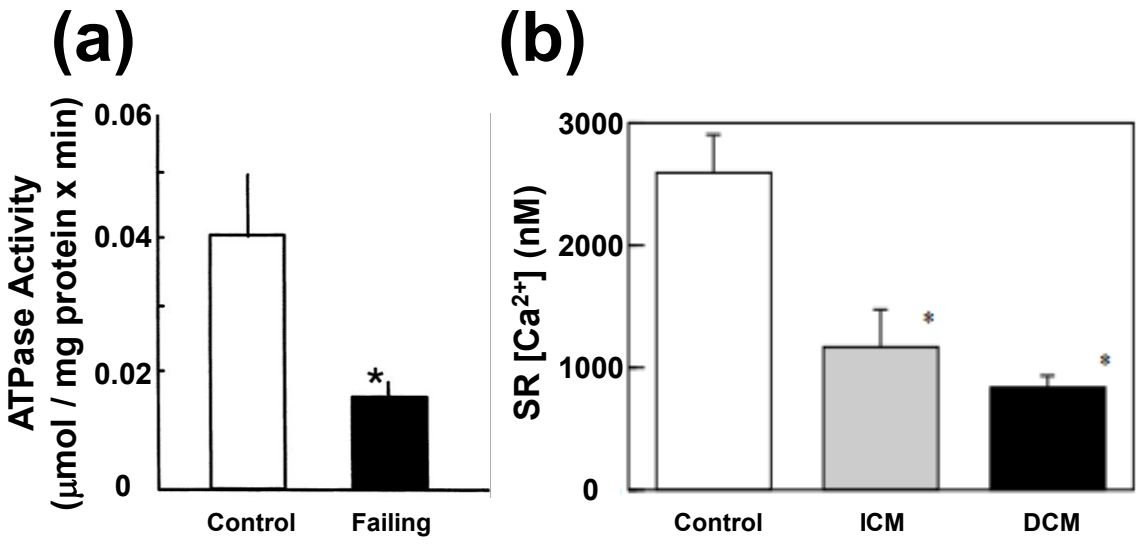

Fig. 8. Impact of heart failure on calcium transport. (a) SERCA activity measurement by pyruvate/NADH coupled enzyme assay and (b) SR calcium content measurement by calcium-binding fura-2 fluorescence on human left ventricle SR samples collected from healthy (control) and heart failure (failing, ischemic cardiomyopathy and dilated cardiomyopathy) patients. Heart failure patients demonstrate lower ATPase activity and lower SR [Ca], indicative of insufficient SERCA activity. Figures adapted from [62] and [63].

of this method, a number of limitations are clear. Approximately 80% of adults exhibit immune response of varying intensity to the AAV vector [75], AAV vector may only be administered once per person due to development of AAV-specific antibodies [71], and while it is injected directly into the heart, it diffuses to other organs including the liver and spleen [76].

An alternative to overexpressing SERCA is to directly activate endogenous SERCA. This is more difficult than overexpression because subtle and precise structural perturbation is required to force SERCA into an active conformation. In general, this requires further understanding of the structure-function relationship for the SERCA-PLB complex through its enzymatic cycle. This is well-developed for SERCA alone (see Fig. 3), but not for the SERCA-PLB complex. High-resolution crystal structures of the SERCA-PLB complex have begun to emerge, and they have been invaluable in hypothesizing the structural basis for SERCA inhibition, particularly for the PLB TM helix. However, crystal structures are often acquired under several non-physiological conditions: in detergent or non-native lipid, frozen at low temperature and lacking intrinsic dynamics that plays a role in function, or bound to inhibitors that perturb structure. Additionally, they often fail to resolve protein segments with considerable dynamics, such as PLB's amphipathic helix (domain Ia). Detailed structural studies of the SERCA-PLB complex at physiological conditions are needed to complete the model begun by crystal structures of the SERCA-PLB complex structure-function relationship as it exists in live cells.

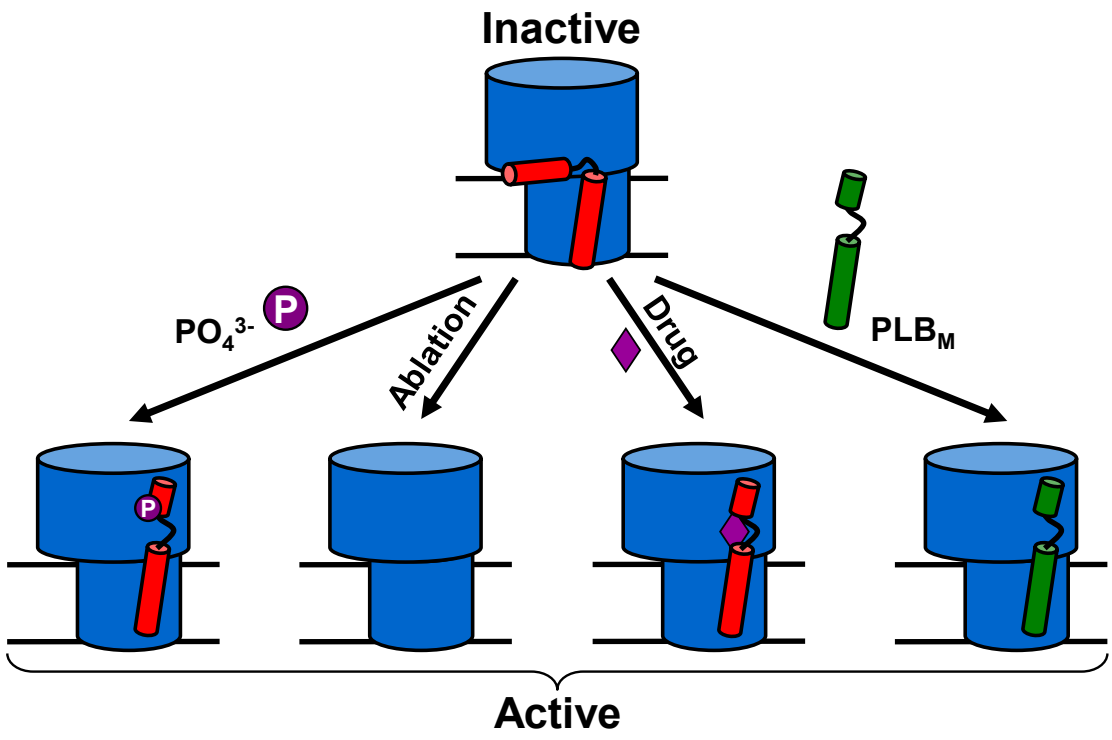

Fig. 9. Schemes for SERCA activation. The physiological method of activation is phosphorylation of PLB (left) during adrenaline response. PLB could also be ablated from the system (mid-left). A small molecule drug could stabilize a non-inhibitory conformation of PLB on SERCA (mid-right). Also, a PLB mutant with similar binding affinity but reduced inhibitory potency could be introduced (right).

What methods do we have available for activating SERCA? Fig. 9 shows several different schemes to activate SERCA. One direct method is to remove PLB from the SR (ablation), thus eliminating its inhibitory effect on SERCA. This has been done by knocking out the gene responsible for PLB expression in mice and human models. While increased SR calcium and increased cardiac contractility were measured in isolated mice and human myocytes [77], mice subjects still suffered from heart failure [78, 79]. Additionally, ablation of PLB removes cardiac muscle regulation by β-adrenergic stimulation, rendering the heart unable to respond to stress-induced adrenaline [77].

A less drastic alternative to PLB ablation is reduction of PLB inhibitory potential through mutation. The goal is to engineer a PLB mutant with similar binding affinity to

SERCA such that it can compete with endogenous wild-type SERCA, but adopts an alternate, less inhibitory, conformation upon SERCA [26, 60, 80]. Several PLB mutations have been characterized, including the superinhibitory and lethal Arg9Cys [81, 82], the phosphomimetic Ser16Glu [82, 83], and the monomeric Cys36Ala/Cys41Phe/Cys46Ala (AFA) [36]. Notably, work by the Veglia lab has demonstrated correlation between inhibitory potential, binding affinity, and dynamics using nuclear magnetic resonance (NMR) on PLB with mutations at positions 16 and 21 in the cytoplasmic helix and loop regions respectively [82].

Another method is to use a small molecule (drug) with affinity for the SERCA-PLB binding interface to allosterically alter the SERCA-PLB conformation to a less inhibitory structure. This could be accomplished through perturbation of the structure of SERCA or PLB within the complex, and similar to the previous method, should not significantly alter the binding affinity of PLB. To discover these small molecule drugs, broad-range screening experiments are performed using pre-existing drug libraries. These screening experiments test hundreds of small molecules quickly, in order to identify those that perturb protein structure, called 'hits'. Preliminary pilot studies using fluorescence resonance energy transfer (FRET) between SERCA and PLB (IAEDANS-SERCA and DABCYL-PLB) [84] and within SERCA (RFP-GFP-SERCA) [85] have identified several compounds that alter SERCA-PLB structure, including CDN1001, CDN1033, CDN1134, and CDN1163. Subsequent experiments further characterize these hits through detailed functional and structural studies, in order to elucidate the mechanism of these small molecules (unpublished results and in-progress studies by the Thomas lab).

Additionally, chemical engineers are currently designing derivatives in the hopes of obtaining a small molecule with higher efficacy [84, 85].

1.7 Thesis Outline and Significance

The primary aim of my thesis work is to determine the structural basis for SERCA regulation by PLB, including inhibition and phosphorylation-induced relief of inhibition (see Fig. 7). This is to support the therapeutic treatments described in the previous section, with particular emphasis on PLB mutants and small molecule drugs, which aim to perturb SERCA-PLB structure towards an active conformation. While it is true that effective mutants and drugs can be discovered without a structural basis, this structural information will make targeted research possible, expediting development and leading to treatments with higher efficacy and specificity. In my work, I probe the conformation of PLB within the active and inactive SERCA-PLB complex using EPR spectroscopy, which I will demonstrate in Chapter 2, is an excellent tool to measure protein structure and dynamics under physiological conditions.

The first goal of my thesis work was to resolve the structural effect of Ser16 PLB phosphorylation on the SERCA-PLB complex, in terms of the competing Dissociation and Subunit models (Chapter 3). Finding strong evidence to support the Subunit Model, I continued to further probe the structural mechanism of SERCA inhibition relief by PLB phosphorylation. To do so, I optimized a reconstitution system (bicelles) in which I could study changes in protein orientation at physiological conditions (Chapter 4). I implemented this system to measure PLB topology using a bifunctional spin label (BSL),

which was corroborated by molecular dynamics simulations (Chapter 5). Having validated the technique, I then pursued measurements of PLB topology in the presence of SERCA, which is an ongoing study (Chapter 6). In Chapter 7, I summarize the main conclusions of my thesis work, and outline future studies that follow from the research presented here.

Chapter 2: Electron Paramagnetic Resonance

2.1 Electron Spin Label and Site-Directed Spin Labeling

Electron Paramagnetic Resonance (EPR) is a spectroscopic experiment designed to measure the local environment, structure, and dynamics of molecules and proteins through a free radical (unpaired electron). With the exception of metal complexes and a few other compounds, most molecules lack an unpaired electron. To perform EPR

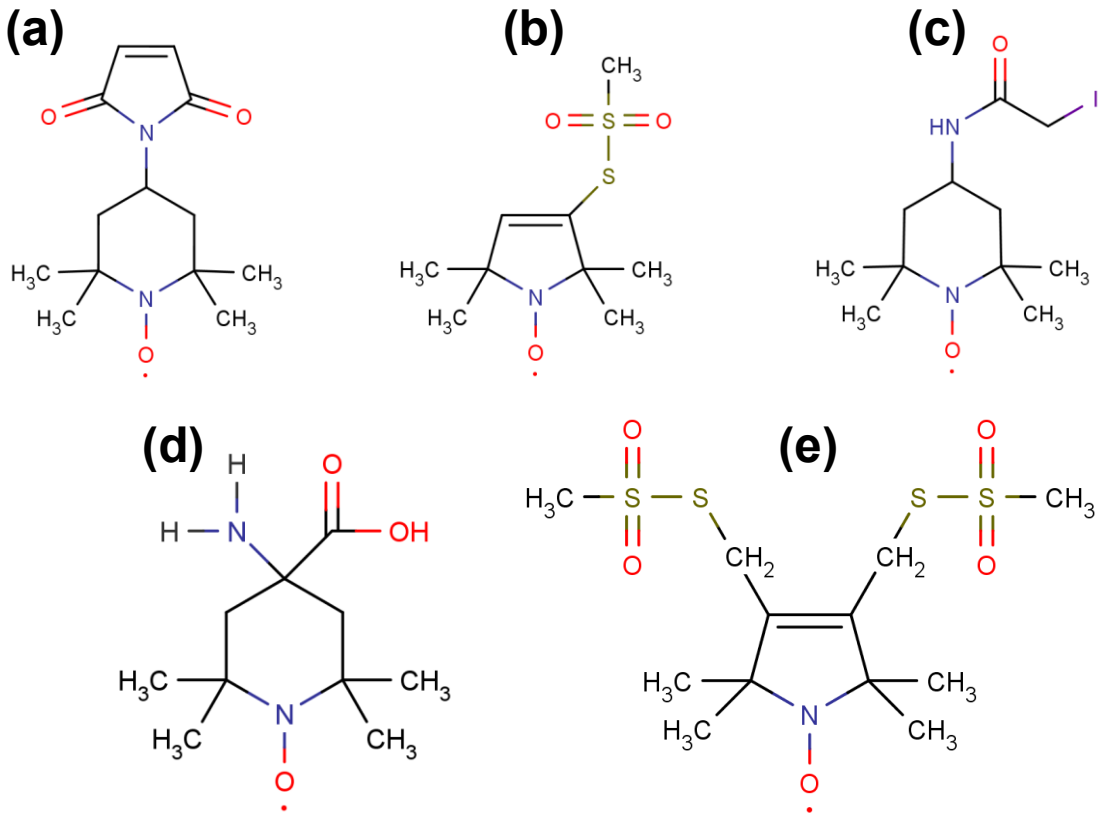

Fig. 10. Common EPR spin labels for site-directed spin labeling. The maleimide spin label (a), methanethiosulfonate spin label (MTSL, b), and iodoacetamide spin label (IASL, c) all attach monofunctionally to the sulfhydryl group on a single cysteine. The 2,2,6,6-tetramethyl-N-oxyl-4-amino-4-carboxylic acid spin label (TOAC, d) is directly incorporated as a synthetic amino acid within a protein's sequence, while the 3,4-bis-(methanethiosulfonyl-methyl)-2,2,5,5-tetramethyl-2,5-dihydro-1h-pyrrol-1-yloxy spin label (BSL, e) attaches to two free cysteines by disulfide bonding.

experiments on these species, a spin label containing an unpaired electron can be attached to the molecule (Fig. 10). Most electron spin labels are comprised of a five or six membered aromatic ring, with a nitroxide bond containing the unpaired electron in a p orbital. Methyl groups stabilize the nitroxide bond, while atoms on the other side of the aromatic ring accommodate attachment to the protein.

There are several ways to attach spin labels to proteins [86]. The most common method is attachment to a single cysteine residue (monofunctional spin label). Cysteines contain a sulfhydryl group (SH) that can react with double bonds within aromatic rings (C=C, maleimide, Fig. 10a), a sulfonyl group (SO_2CH_3, methanethiosulfonate, Fig. 10b) or an iodo group (I, iodoacetamide, Fig. 10c). The reacted cysteine may be endogenous, or mutated into the protein sequence. The process of attaching a spin label to a specific residue on a protein is called site-directed spin labeling (SDSL) [87]. Cysteine is a relatively uncommon amino acid, so there is typically little to no problem with specificity. However, with site-directed mutagenesis, cysteines can be mutated into a protein sequence, or native cysteines can be mutated out, prior to protein expression in cells. However, choosing a suitable location can be problematic, since protein structure and function must be preserved. Monofunctional attachment is common because it requires only a single cysteine, and thus is less likely to significantly affect the protein. Its primary limitation is the length and flexibility of the linker segment attaching the spin label to the host protein. These perturbations in distance and motion can complicate measurements of protein structure and dynamics; however this is not always the case, and

is typically site-dependent. Many studies have utilized monofunctional spin labels with excellent success [87-89].

Another method involves attachment to two cysteine residues (bifunctional spin label). This class of spin label was developed by Toshiaki Arata and co-workers, as a way to restrict the label dynamics often encountered with monofunctional spin labels [90]. The bifunctional spin label is best attached on a segment of protein with rigid backbone dynamics, such as an alpha helix, where the periodic structure facilitates attachment at two specific residues (residue *i* and *i+4*, for example) (Fig. 10d) [91]. In contrast to a monofunctional spin label, a bifunctional spin label is substantially immobilized [92, 93], though its linker does introduce some distance perturbations. Additionally, optimizing the chemical reaction to obtain homogeneous bifunctional attachment (as opposed to partial monofunctional attachment, or protein cross-linking) requires substantial effort [94, 95], and is not possible for all proteins.

The last method incorporates the spin label as a synthetic amino acid into the protein structure. This technique was developed by Clovis Nakaie as a way to directly couple a spin label into the peptide backbone [96]. The 2,2,6,6-tetramethyl-N-oxyl-4-amino-4-carboxylic acid (TOAC) attaches with an amine group and carboxylic acid on the alpha carbon of the aromatic ring, similar to a natural amino acid (Fig. 10e). This results in a spin label which is rigidly bound to the protein and contains essentially no linker region, making it ideal for protein measurements [23, 97]. The primary limitation with a synthetic spin label like TOAC is that the protein must be synthesized and the spin label inserted during synthesis, typically using a method called solid-phase peptide

synthesis (SPPS). This technique requires extensive optimization, and is applicable only to proteins with ~50 residues or less [98].

2.2 The Zeeman Effect

The origin of the EPR measurement is the Zeeman Effect, an atomic interaction discovered by Pieter Zeeman and characterized by Hendrik Lorentz in 1897 [99]. Zeeman placed a Bunsen burner within a magnetic field produced by an electromagnet, and observed the emission lines of sodium chloride change wavelength as a function of magnetic field strength. With the assistance of Lorentz, he proposed that as ions from the salt were released from combustion, they experienced force from the magnetic field, altering their vibration and thus their emission wavelength. The force F on a molecule with magnetic dipole moment μ in a magnetic field H is:

$$\vec{F} = \vec{\nabla}(\vec{\mu} \cdot \vec{H}) \qquad \text{Eq. 1}$$

The net energy resulting from the force in Eq. 1 is thus:

$$E = -\int \vec{F} \cdot d\vec{l} = -\vec{\mu} \cdot \vec{H} \qquad \text{Eq. 2}$$

In EPR, our molecule of interest is an unpaired electron. Its magnetic moment is generated by its spin, an intrinsic quantum mechanical property. This spin does not correspond to actual movement of charge (if it did, the electron would have to rotate at a velocity faster than light [100]), but is a property similar to mass or electric charge. The electron has a spin quantum number s = ½. Its total spin angular momentum S is then given by:

$$S = \sqrt{s \cdot (s+1)} \cdot \hbar \qquad \text{Eq. 3}$$

where ħ is the reduced Planck constant (ħ = h / 2π), and h is Planck's constant. Therefore, for the electron with spin ½, its total spin angular momentum is $\sqrt{3/4} \cdot \hbar$. Its spin angular momentum in any single direction is given by:

$$S_z = \hbar \cdot m_s \qquad \text{Eq. 4}$$

where m_s is the secondary spin quantum number. Therefore, for the electron with spin ½, $S_z = \pm \hbar/2$. The reason that $|S_z| < S$ is due to the uncertainty principle, which places a lower limit on the spin angular momenta in the x and y directions [100]. Generally, we choose the z direction to coincide with our experimental setup, such as the magnetic field direction. From this result, we can calculate the electron magnetic moment due to its spin angular momentum:

$$\mu_z = -g \cdot \beta \cdot \frac{S_z}{\hbar} \qquad \text{Eq. 5}$$

where g is the electron's spin g factor, relating its magnetic moment to its spin angular momentum, and β is the Bohr magneton. Therefore, for the electron, $\mu_z = \pm g \cdot \beta / 2$. Combining this result with Eq. 2, we obtain:

$$E = \pm \frac{1}{2} \cdot g \cdot \beta \cdot H \qquad \text{Eq. 6}$$

where H is now the magnitude of $\vec{H}$ defined along the z direction (the applied magnetic field strength). From Eq. 6, we see that the unpaired electron can occupy one of two energy levels. The difference in energy is given in Eq. 7:

$$\Delta E = E_+ - E_- = g \cdot \beta \cdot H \qquad \text{Eq. 7}$$

It is the energy structure in Eq. 7 that allows us to perform EPR spectroscopy, using photons of energy hν (where ν is the radiation frequency) to excite spin transitions from the lower (ground) to the upper (excited) electron spin states, and to stimulate spin transitions from the excited to ground state (Fig. 11). When the supplied radiation possesses the correct energy to excite these transitions, the system is in resonance. This condition is specified by the resonance equation obtained from setting Eq. 7 equal to hν:

$$H_{RES} = \frac{h \cdot \nu_{RES}}{g \cdot \beta} \qquad \text{Eq. 8}$$

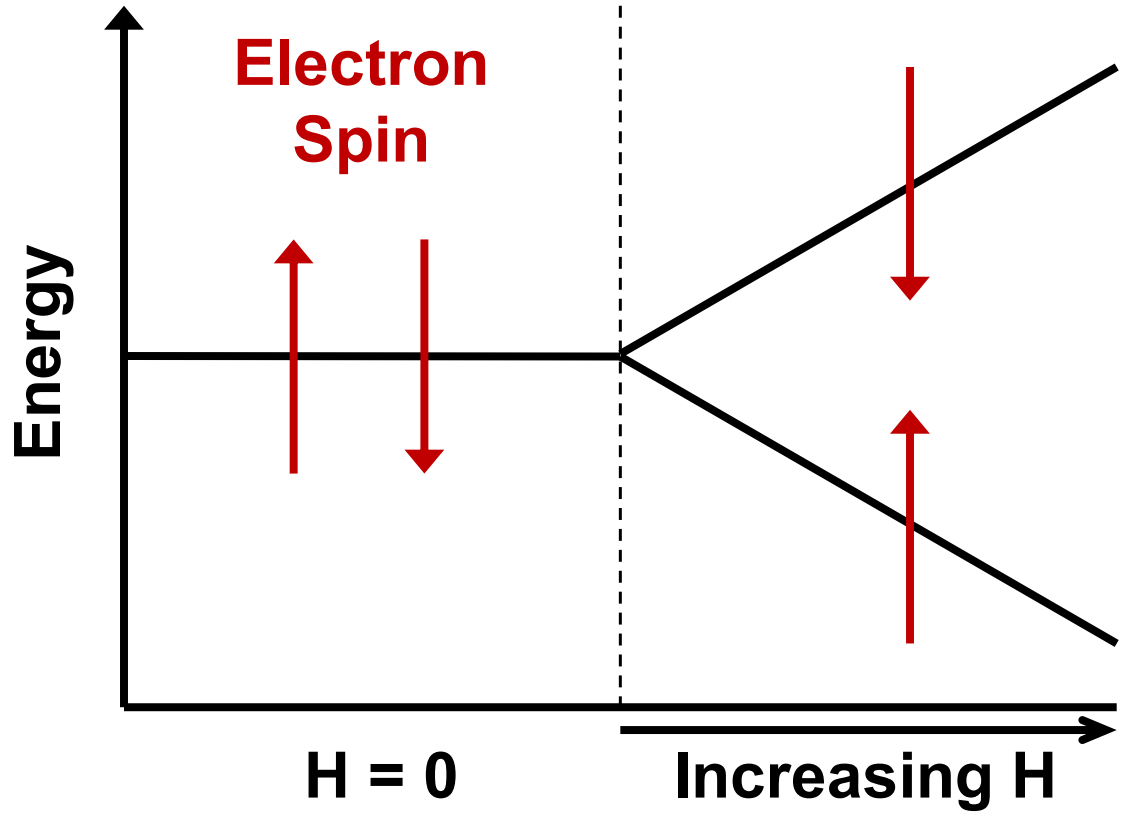

Fig. 11. The Zeeman effect. An unpaired electron has two spin states ($m_s = \pm ½$). In the absence of a magnetic field (left), there is no difference in energy between $m_s = +½$ and $m_s = -½$. However, when a magnetic field is applied, the Zeeman effect breaks the energy degeneracy between these two states, such that E(+½) is greater than E(-½). The difference in energy is proportional to the magnetic field strength (see Eq. 7).

where H_{RES} and ν_{RES} correspond to the magnetic field strength and radiation frequency, respectively, required to achieve resonance. In theory, either may be varied to achieve resonance, though in practice, the radiation frequency is held constant while the magnetic field is varied [101]. The populations of electrons in the ground and excited states are defined by the Boltzmann distribution:

$$\frac{N_+}{N_-} = EXP\left(\frac{-\Delta E}{k_B T}\right) \qquad \text{Eq. 9}$$

where EXP(x) is the exponential function (e^x). At Boltzmann equilibrium, there is always an excess population in the ground state. For spectroscopy in general, this excess population is very small ($\Delta N_{EPR} \sim 0.15\%$, $\Delta N_{NMR} \sim 0.01\%$). The ground state population excess allows for radiation to promote electrons to the excited state. This radiation shifts the spin system away from Boltzmann equilibrium, and if it is sufficiently intense, can eliminate the excess population in the ground state. When this occurs, the spin system is saturated, and can no longer absorb radiation. Electrons in the excited state will naturally relax back to the ground state by T_1 (spin-lattice) relaxation, a process where excited state electrons release energy to the surrounding lattice of atoms. T_1 relaxation is described by Eq. 10:

$$\left.\frac{N_+}{N_-}\right|_t = \left(\left.\frac{N_+}{N_-}\right|_{EQ}\right) - \left(\left.\frac{N_+}{N_-}\right|_{SAT}\right) \cdot EXP\left(\frac{-t}{T_1}\right) \qquad \text{Eq. 10}$$

where t corresponds to time t, EQ corresponds to Boltzmann equilibrium, and SAT corresponds to the change in population induced by radiation. Most conventional EPR experiments are done in the absence of significant saturation; however there are exceptions (see Section 2.6). In addition to T_1 relaxation, there is also T_2 relaxation (spin-

spin), involving the exchange of spin states between two electrons. Since there is no net energy change due to T_2, it does not contribute to saturation. However it does contribute to spin coherence, and affects the ensemble of spin states. Thus, T_2 is entropic relaxation, while T_1 is enthalpic relaxation.

2.3 The EPR Spectrometer

A conventional EPR spectrometer consists of four primary components: the microwave source, the resonator, the electromagnet, and the detector diode (Fig. 12).

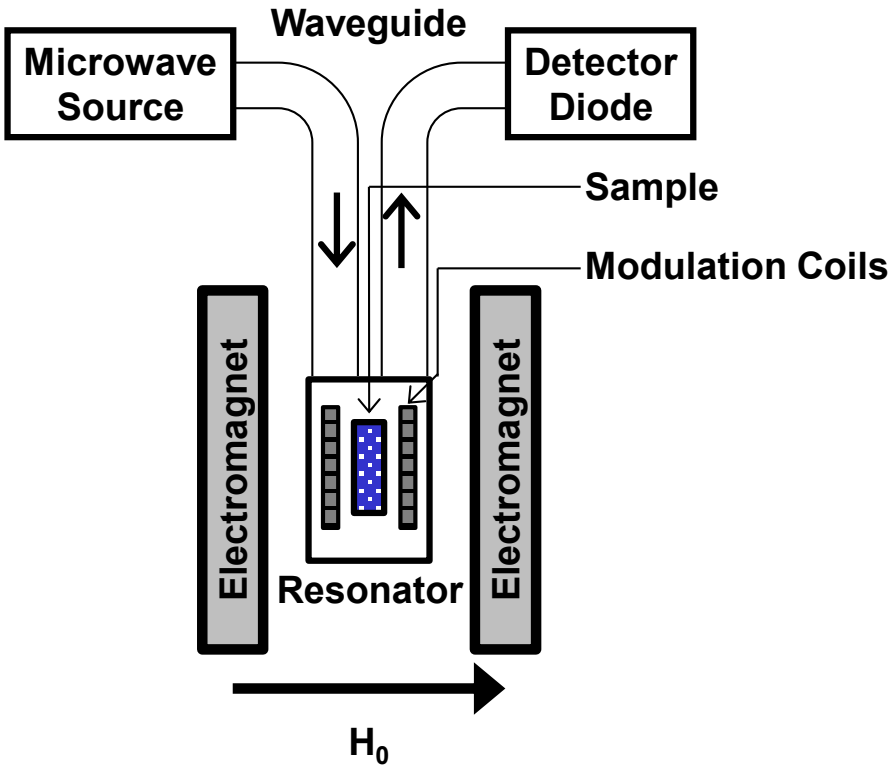

Fig. 12. Diagram of a continuous wave EPR spectrometer. Microwaves are produced at the source by a Gunn diode (left), traveling through the waveguide to the resonator (center) where they produce a standing wave across the sample (dotted blue). As microwaves are absorbed by the sample, others are reflected from the resonator back up the waveguide to the detector (right). The electromagnet sweeps the magnetic field strength, while the modulation coils within the resonator generate an oscillating magnetic field, allowing for derivative absorption detection and phase-sensitive detection.

Within the microwave source, microwaves are generated by a Gunn diode. In it, electrons are accelerated from anode to cathode through semiconductor material, acquiring sufficient kinetic energy to reach an energy band above the conduction band. Relaxation from this band generates microwave radiation [102]. These microwaves are directed via waveguides to two components: (1) the microwave detector, to keep it in its linear operating regime (bias level), and (2) the resonator, a metal cavity designed to expose the sample to standing microwaves (~mW power). The sample containing unpaired electrons will absorb some microwaves, causing a change in the microwave power reflected back from the resonator. These reflected microwaves travel back through the waveguide, and to the detector diode (Schottky) within the microwave bridge, where they are rectified into an electrical signal. During the EPR experiment, an electromagnet generates a magnetic field at the sample. This field is swept from low to high strength (~ 3300 G to 3400 G for nitroxide spin labels at X-band microwave radiation), with superimposed field modulation (~1 G amplitude at 100 kHz frequency for conventional EPR). The magnetic field modulation allows detection of derivative microwave absorption, enhancing EPR spectral lineshape sensitivity, and enabling phase-sensitive detection, where all signals not matching the modulation frequency are rejected before post-acquisition processing.

2.4 Hyperfine Interaction

The resonance equation (Eq. 8) demonstrates that absorption and emission will occur for a specific magnetic field strength and radiation frequency. In practice, the radiation frequency is completely defined by the microwave source used in the

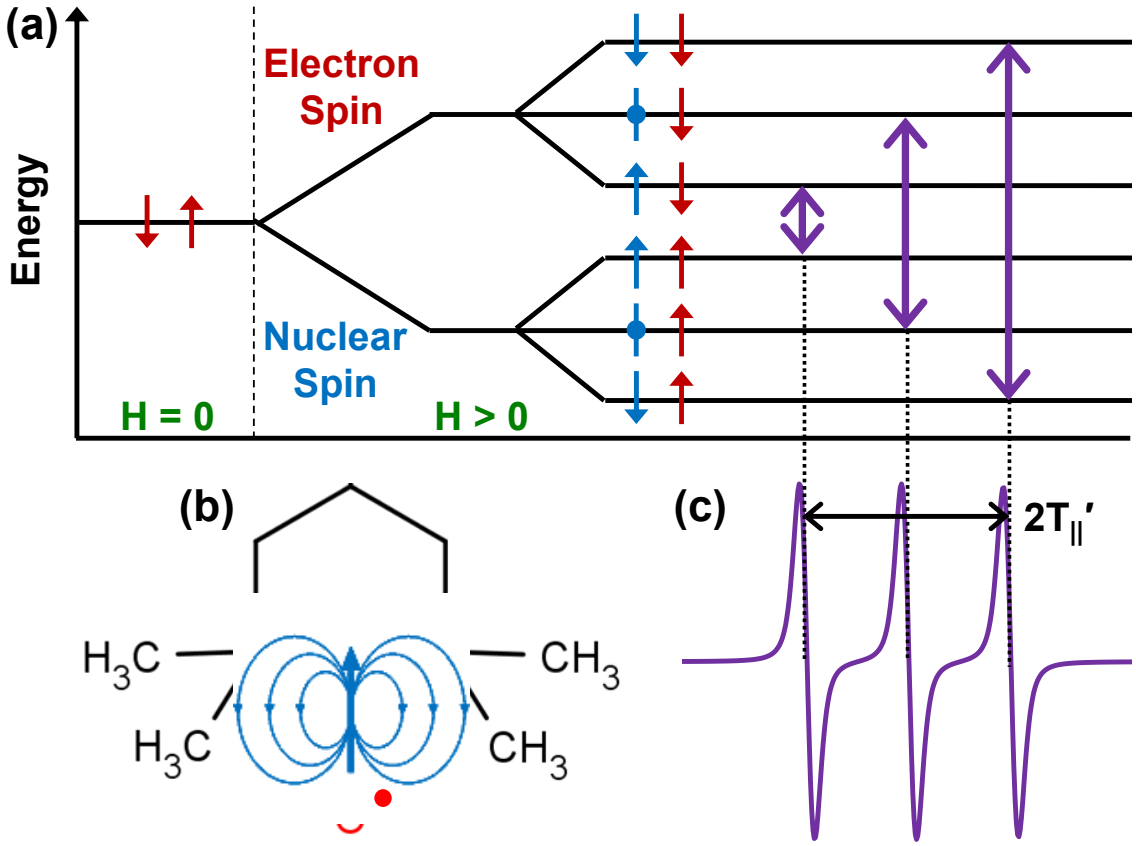

Fig. 13. The hyperfine interaction. (a) In addition to the Zeeman interaction breaking the spin degeneracy (Fig. 11), the hyperfine interaction splits the spin energy levels further, such that three spin transitions are possible (purple, right). The nitrogen nucleus within the electron spin label generates a magnetic field (blue) experienced by the unpaired electron (red) in addition to the external magnetic field (green) (b). The three spin transitions (purple) lead to the typical nitroxide spectrum, with three lines separated by $2T_{||}'$ (c).

experimental setup. However, the magnetic field strength is not completely defined by the electromagnet; there are several magnetic field sources within the sample itself. The source that typically exerts the strongest field on the unpaired electron is the nitrogen nucleus within the nitroxide bond of the spin label. ^{14}N accounts for 99.64% of naturally occurring nitrogen, and possesses a nuclear spin of I = 1. Therefore, it may adopt a spin state of m_I = -1, 0, or +1 along the axis of the external magnetic field, generating an additional magnetic field that can increase or decrease the total magnetic field experienced by the unpaired electron (Fig. 13). The interaction of the nitrogen magnetic

field with the unpaired electron is called the hyperfine interaction, and further splits the two-state system caused by the Zeeman interaction (Fig. 11) into a six-state system (Fig. 13). Quantum selection rules state that the nitrogen nuclear spin cannot change during an electron transition, resulting in three unique resonances (Fig. 13). Therefore, the resonance equation (Eq. 8) can be rewritten to reflect the dependence on nitrogen nuclear spin:

$$H_{RES} = \frac{h \cdot \nu_{RES}}{g \cdot \beta} - m_I T \qquad \text{Eq. 11}$$

where m_I is the nitrogen secondary spin quantum number, and T is the hyperfine splitting constant. Since there are three possible values for m_I (-1, 0, +1), there are three possible values for H_{RES}, resulting in the typical nitroxide three line spectrum (Fig. 13c).

2.5 Orientation Sensitivity

As the unpaired electron's p orbital within the spin label is anisotropic, it defines a coordinate system called the probe frame (Fig. 14). Within this frame, the nitrogen p orbital is along the z direction, and the nitroxide bond is along the x direction. This probe frame is relevant because the direction of the magnetic field within the frame alters the resonance condition (Eq. 11). That is, both the electron g tensor and the hyperfine tensor are anisotropic. Defining the magnetic field direction in the probe frame using the spherical angles θ (polar) and ϕ (azimuthal):

$$H_{RES}(\theta, \phi) = \frac{h \cdot \nu_{RES}}{g(\theta, \phi) \cdot \beta} - m_I T(\theta, \phi) \qquad \text{Eq. 12}$$

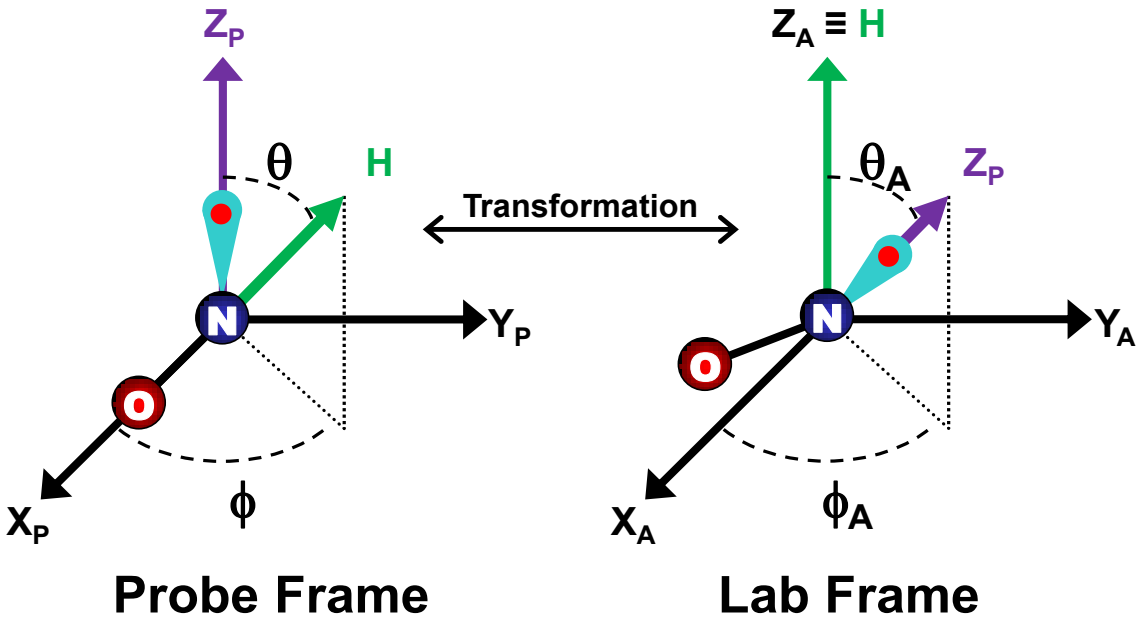

Fig. 14. EPR coordinate systems. The most common reference frame is the probe frame (left), defined by the spin label. The z axis is parallel to the p orbital containing the unpaired electron (cyan with red dot), while the x axis is parallel to the nitroxide bond (N-O). The magnetic field **H** is then described as a vector within this frame by the polar angle θ and the azimuthal angle ϕ. Another common frame is the lab frame (right), where the magnetic field defines the z axis. In this frame, the label principal axis (z_P) is described by the angles θ_A and ϕ_A.

Thus, Eq. 12 shows that the effective g and T values that define magnetic resonance depend upon the magnetic field direction (θ,ϕ), as shown in Fig. 15. These dependencies are shown in Eq. 13 and Eq. 14:

$$g(\theta,\phi) = g_x sin^2\theta cos^2\phi + g_y sin^2\theta sin^2\phi + g_z cos^2\theta \qquad \text{Eq. 13}$$

$$T(\theta,\phi) = \left[T_x^2 sin^2\theta cos^2\phi + T_y^2 sin^2\theta sin^2\phi + T_z^2 cos^2\theta\right]^{1/2} \qquad \text{Eq. 14}$$

Since g and T have different dependencies on the spherical angles θ and ϕ, there is no combination of θ and ϕ that would simultaneously yield the isotropic g and T values, which are:

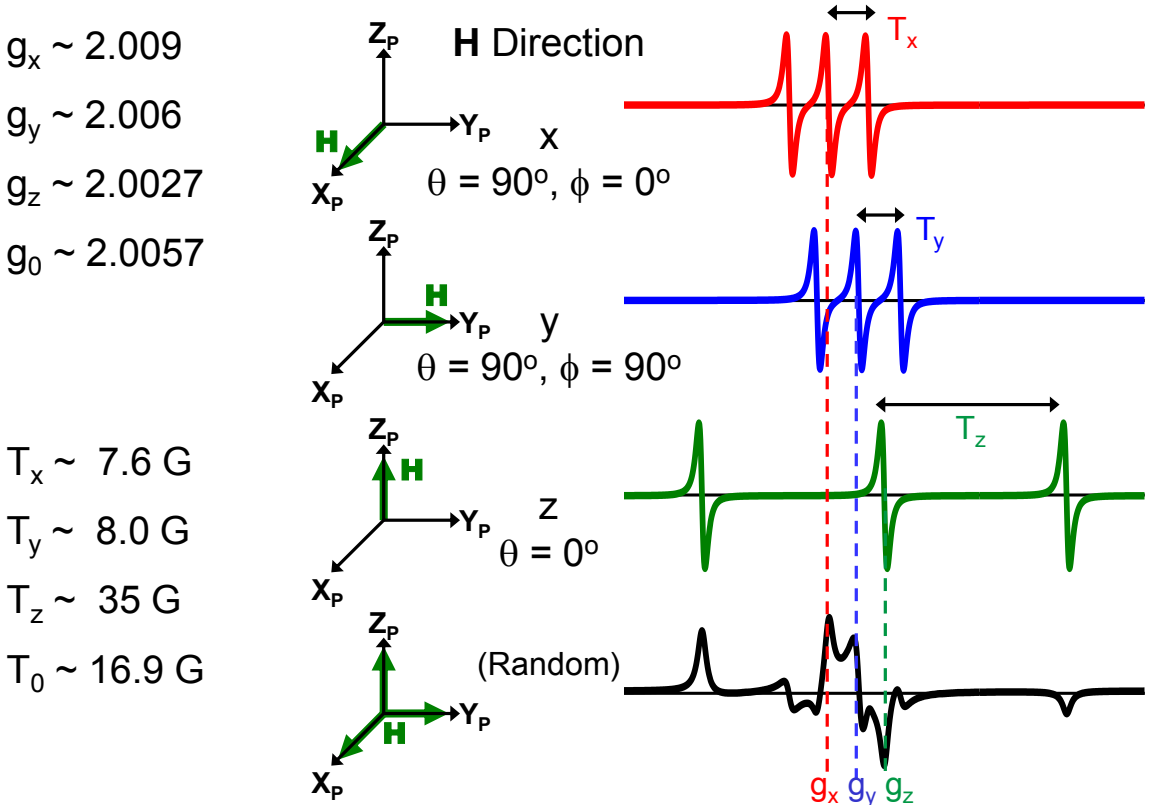

Fig. 15. EPR orientation dependence. Both the center (electron g) and splitting (hyperfine T) of the EPR spectrum are sensitive to the orientation of the label relative to the magnetic field. See also Eq. 13 and Eq. 14 for calculation of the effective g and T values.

$$g_0 = \frac{g_x + g_y + g_z}{3} \qquad \text{Eq. 15}$$

$$T_0 = \frac{T_x + T_y + T_z}{3} \qquad \text{Eq. 16}$$

As such, EPR does not have the orientational ambiguity of fluorescence measurements, which yield isotropic values for the magic angle of $\theta \approx 54.7^{o}$ (Fig. 15) [103]. This makes EPR well-suited for measuring orientation distributions of spin labels, provided the experiment is done on a well-ordered system. This involves choosing relatively immobile residues on proteins, and choosing an anisotropic protein environment with a well-defined symmetry axis, such as a muscle fiber, substrate-supported lipid bilayer, or bicelles.

2.6 Rotational Diffusion Sensitivity

As a result of its sensitivity to orientation, EPR is also sensitive to rotational diffusion, which typically occurs as Brownian motion. In characterizing rotational diffusion, we refer both to the rate and amplitude of motion (Fig. 16). The rate of rotational diffusion is described by the diffusion rate constant D_R. This can be estimated with the Stokes-Einstein formula, which for a globular protein takes the form:

$$D_R = \frac{k_B T}{8\pi \cdot \eta \cdot r^3} \qquad \text{Eq. 17}$$

where k_BT is the thermal Boltzmann factor, η is the surrounding viscosity, and r is the protein radius. For membrane-bound proteins with a cylindrical transmembrane region, Eq. 17 takes the form:

$$D_R = \frac{k_B T}{4\pi \cdot \eta \cdot r^2 \cdot h} \qquad \text{Eq. 18}$$

where h is the height of the membrane. From the diffusion rate constant, we can define another common parameter called the rotational correlation time: τ_R. The rotational correlation time is related to the diffusion constant by Eq. 19:

$$\tau_R = \frac{1}{6 \cdot D_R} \qquad \text{Eq. 19}$$

τ_R is the time required for the protein to diffusion one radian in a given direction. For proteins free in solution, $\tau_R \sim$ ns, while for proteins embedded in membrane, $\tau_R \sim \mu$s.

In addition to the rate of rotational diffusion as characterized by τ_R, the amplitude of rotational diffusion can be characterized by the order parameter S:

$$S = \frac{1}{2}(3 < cos^2\beta > -1) \qquad \text{Eq. 20}$$

where β is the angle between an axis upon the object (such as the spin label's principal axis) and the sample's symmetry axis (lipid bilayer normal, muscle fiber axis, etc). For a low value of S (~ 0), $<\cos^2\beta>$ ~ 1/3, indicating an isotropic distribution for β, and isotropic rotational diffusion. For a high value of S (~ 1), $<\cos^2\beta>$ ~ 1, indicating singular values for β (0^o or 90^o) and corresponding axial rotational diffusion. S can also be

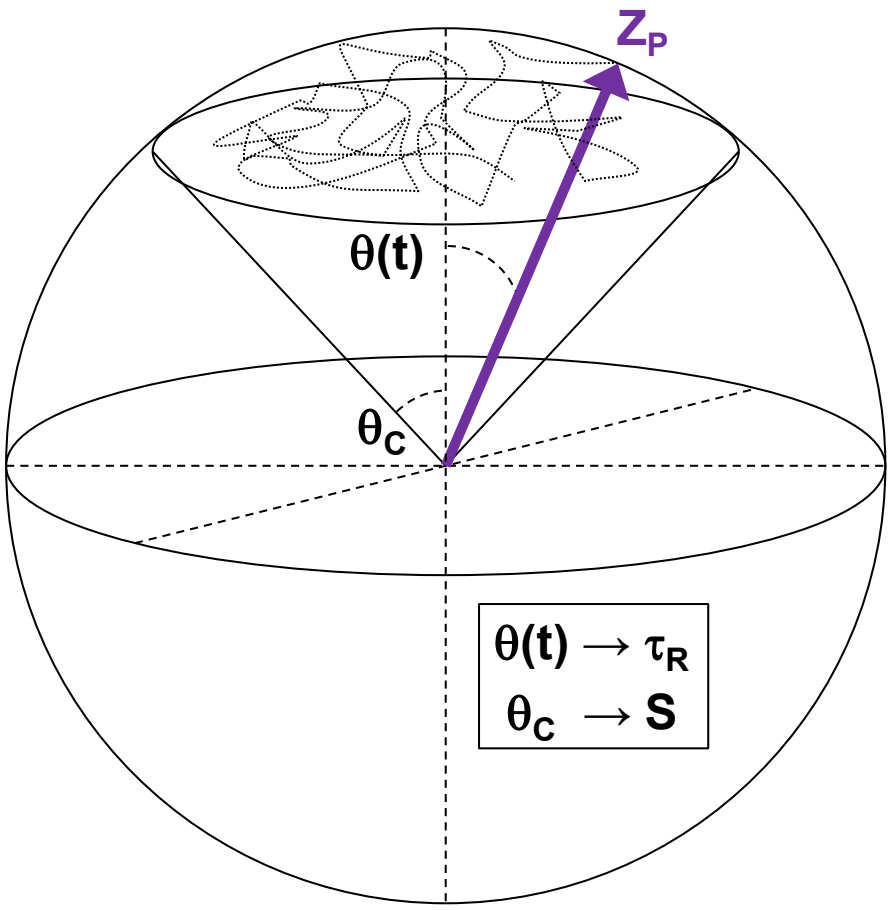

Fig. 16. Rate and amplitude of rotational diffusion. The rate of rotation diffusion describes the spin label's (z_P) change in angular displacement (θ) as a function of time. This is typically referred to by the correlation time τ_R. The amplitude of rotational diffusion describes the spin label's maximum angular displacement (θ_C) over its entire trajectory. Often this is referred to by a cone angle, but this is one of several model-dependent interpretations for anisotropy.

calculated directly from spectral measurements, as shown in Eq. 21:

$$S \equiv \frac{observed\ anisotropy}{maximum\ anisotropy} = \frac{T_{||}' - T_0}{T_{||} - T_0} \qquad \text{Eq. 21}$$

where $T_{||}'$ is the splitting for the sample of interest (intermediate splitting), T_0 is the splitting for the sample undergoing rapid, isotropic rotational diffusion (minimum splitting), and $T_{||}$ is the splitting for the sample under full immobilization with an isotropic orientation distribution (maximum splitting) (see also Fig. 13).

Briefly, rotational diffusion can be considered as exchange of different orientation states. Indeed, an EPR spectrum containing all orientation states as static (powder) is much different than an EPR spectrum containing all orientation states with dynamic exchange. The reason for this is that exchange between different orientation states affects

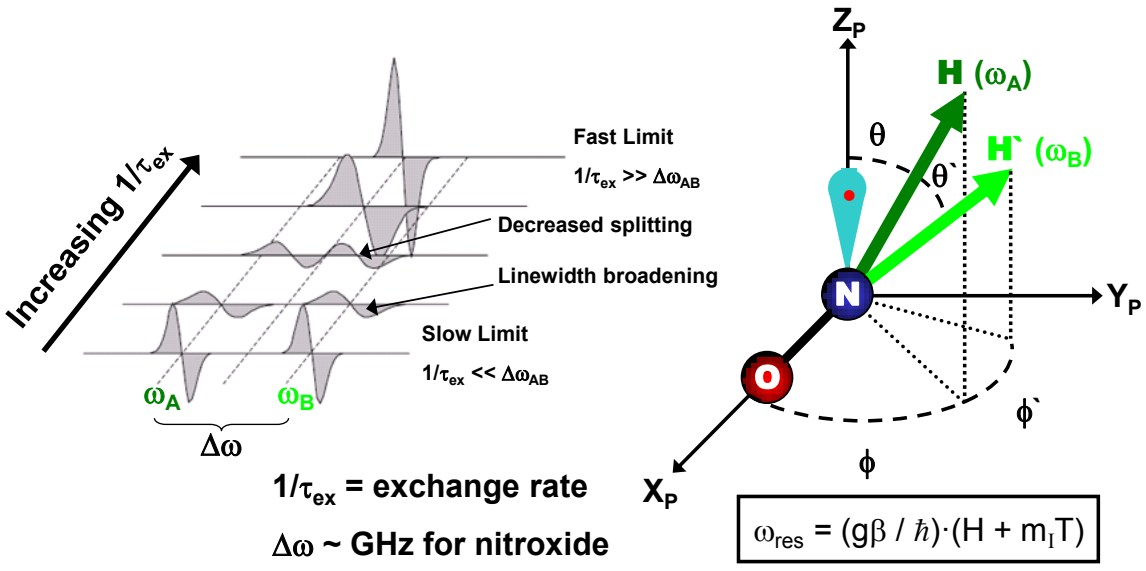

Fig. 17. Chemical exchange between orientation states. For a simple system with two orientation states, there are two resonance points, at ω_A and ω_B. At the slow limit, where there is very little rotational diffusion of the sample and no exchange ($1/\tau_{ex}$) between these two states, resonance occurs only at ω_A and ω_B. As the rate of rotational diffusion increases (relative to the difference between ω_A and ω_B), the resonance points begin to broaden and shift position, until at the fast limit (where the exchange rate is much greater than the difference between ω_A and ω_B), the two orientation states are no longer distinct, and instead we observe a single averaged resonance point.

both the positions (motional narrowing) and widths (linewidth broadening) of the resonance lines (Fig. 17). Rotational diffusion on the order of T_2, the transverse relaxation parameter related to resonance linewidth, will cause motional narrowing and linewidth broadening. Thus, conventional EPR is sensitive to rotational diffusion when ps $< \tau_R <$ μs (Fig. 18, left).

For rotational diffusion slower than microseconds, the conventional EPR spectrum is at the rigid limit, and loses sensitivity to changes in rotational diffusion. However, this slow rotational diffusion is especially relevant for membrane proteins like

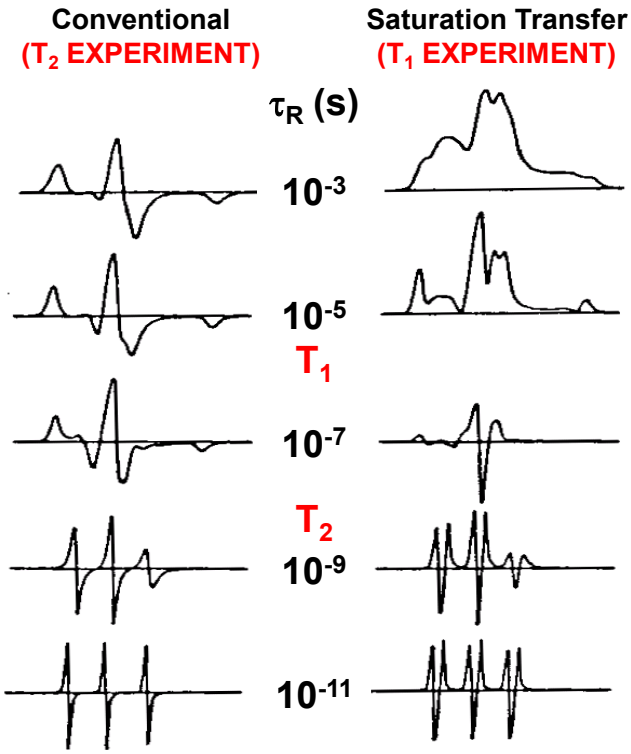

Fig. 18. EPR spectral sensitivity to rotational diffusion. Conventional EPR relies on T_2 relaxation for spectral resolution, so it has sensitivity to rotational diffusion on the order of T_2 (τ_R ~ ps to ns). Rotational diffusion slower than this is at the slow limit for conventional EPR, and no longer can affect the spectrum. In contrast, saturation transfer (ST) EPR relies on T_1 relaxation, so it does have sensitivity to slow rotational diffusion (τ_R ~ μs to ms). When used together, conventional and saturation transfer EPR can measure a broad range of dynamics.

PLB and SERCA. To detect this diffusion, we can use a technique called saturation transfer EPR. In contrast to a conventional EPR experiment, saturation transfer EPR uses high microwave power (~20 mW) to induce significant saturation in the sample, perturbing it from Boltzmann equilibrium. The equilibrium is restored by enthalpic T_1 relaxation, where $T_1 \sim 10$ μs. However, rotational diffusion on the order of T_1 also contributes to the apparent relaxation rate. The rotational diffusion causes saturation to diffuse to other positions in the spectrum (orientations), relieving the saturation induced at the instantaneous spectral position in the experiment, but not of the entire sample (as only T_1 relaxation will truly relieve saturation). As a result, rotational diffusion where ps $< \tau_R <$ ms can be resolved by saturation transfer EPR (Fig. 18, right). In order to enhance sensitivity to this slow rotational diffusion, microwave radiation that is 90^o out of phase with the magnetic field modulation (which is reduced from 100 kHz to 50 kHz) is selectively detected, making the signal intensity lower than that of conventional EPR. Thus, conventional EPR is traditionally used for ps $< \tau_R <$ μs and saturation transfer EPR is traditionally used for μs $< \tau_R <$ ms (Fig. 18).

2.7 Anisotropic Membrane Systems

Measuring the orientation distribution of a spin label attached to a protein requires that the protein be uniformly oriented with respect to a well-defined axis, such as the external magnetic field. In the case of membrane proteins, they must be reconstituted in a different membrane system, as lipid vesicles contain the membrane protein in many different orientations. The ideal environment is an extended, flat patch of lipid bilayer,

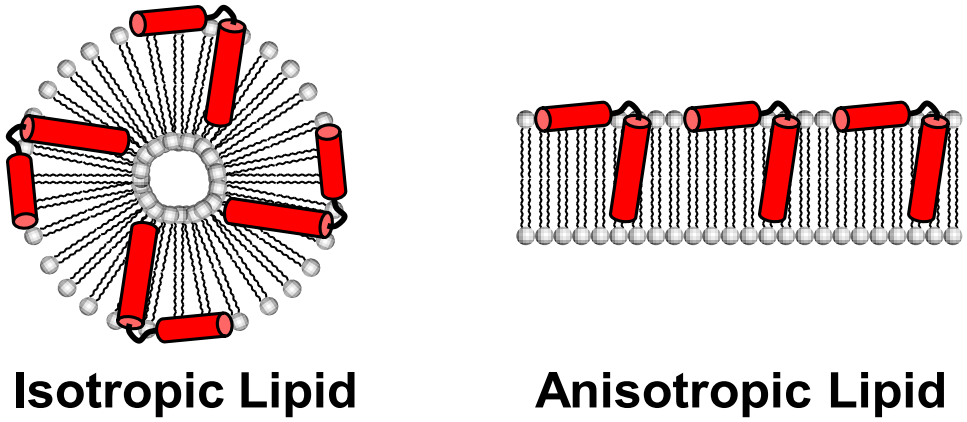

Fig. 19. Isotropic vs anisotropic lipid environments. Proteins (red) are typically reconstituted in isotropic lipid environments like micelles or vesicles (left), resulting in an isotropic protein orientation distribution. In contrast, an anisotropic lipid environment like a substrate-supported bilayer or bicelle (right) results in an anisotropic protein orientation distribution, suitable for protein topology measurements.

which is as similar to the native environment as possible without any membrane curvature.

The most straightforward anisotropic membrane is a substrate-supported lipid bilayer. In this technique, lipids are deposited onto a substrate such as metal or glass, and carefully rehydrated under high humidity to gradually build lipid bilayers upon the substrate. Typically, multiple layers parallel to the substrate surface are obtained, producing an anisotropic membrane. This method is advantageous in that essentially any combination of lipids can be used, such that the protein can be reconstituted in a native-mimicking bilayer. However, the rehydration technique is not amenable to proper complex protein folding, and calls into question whether the environment is completely rehydrated.

Another popular anisotropic membrane is a bilayered micelle, or bicelle. A bicelle is a disc-like lipid structure with a flat patch of long chain (LC) lipid bilayer, and a rim of short chain (SC) lipids to protect the hydrophobic core of the bicelle. Bicelle

characteristics can be altered by the molar ratio of LC lipid to SC lipid (q ≡ [LC] / [SC]); for a bicelle of q ~ 3, its diameter is approximately 30 nm. In an isotropic solution, bicelles freely tumble and function much like vesicles. Due to the regular ordering of the lipid headgroups in the LC lipid bilayer, they possess negative total magnetic susceptibility, and thus can be uniformly aligned in a magnetic field. This magnetic susceptibility can be altered by lanthanide, which chelates to the lipid headgroups and increases or decreases the magnetic susceptibility. This allows alignment of the bicelles with their membrane normal either parallel or perpendicular to the magnetic field axis. Another aspect affecting the alignment properties of bicelles is temperature, which

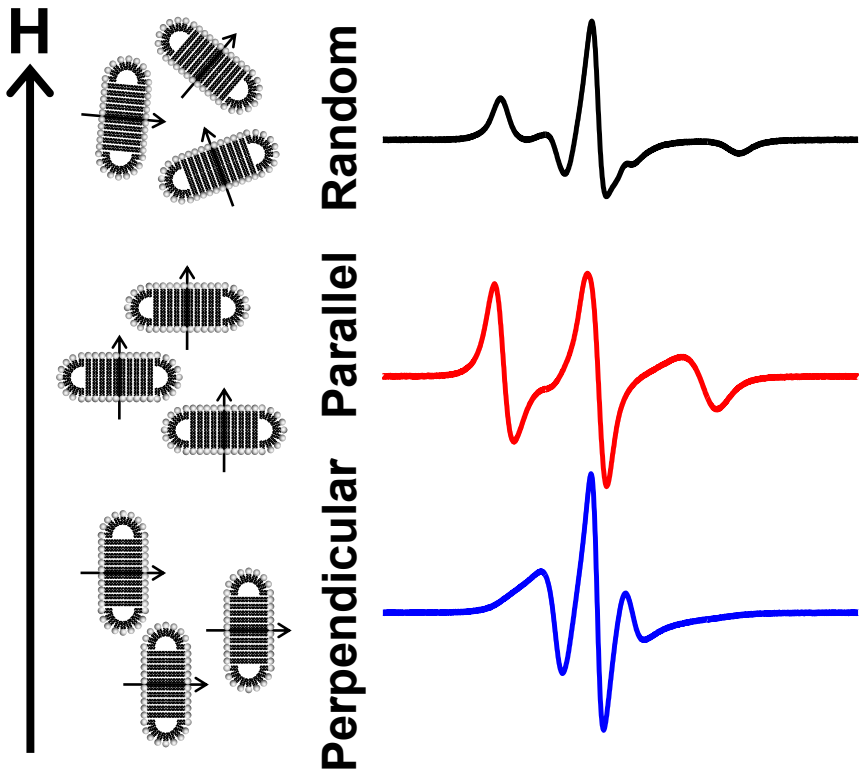

Fig. 20. Oriented bicelle EPR. Spectra of the lipid spin label 5-DOXYL-stearic acid (5-DSA) in bicelles with their membrane normal aligned randomly, parallel, or perpendicular to the spectrometer magnetic field. Substantial changes in lineshape occur based on orientation.

influences the phases of both the constitutive lipids and the bicelles as macromolecules in solution. Above the isotropic phase where bicelles exist as disc-like structures, they begin to fuse together in the nematic and smectic phases, forming large sheets of LC lipid with pores lined by SC lipid. This is commonly referred to as the "Swiss-cheese model".

When spin-labeled proteins are reconstituted in bicelles, the changes in EPR spectra due to alignment are quite distinctive. Fig. 20 shows EPR spectra of the 5-DOXYL-stearic acid lipid spin label in bicelles that are randomly oriented (top), aligned with their membrane normal parallel to the instrument magnetic field (middle) and perpendicular to the magnetic field (bottom). There are substantial changes in splitting, which can be measured to calculate the Euler angles between the spin label's principal axis and the membrane normal:

$$T'_{||} = \left[T_{||}^2 \cdot cos^2\beta_D + T_{\perp}^2 \cdot sin^2\beta_D\right]^{1/2} \qquad \text{Eq. 22}$$

where $T_{||}'$ is the half width of the EPR spectrum, $T_{||}$ and $T_{\perp}$ are the parallel and perpendicular hyperfine tensor values, and β_D is the angle between the spin label's principal axis and the principal diffusion axis (typically taken to be the membrane normal) [104]. An equivalent and perhaps more integrated approach is to determine β_D through direct simulation of the experimental EPR spectra (see Section 2.9). This method also has the distinct advantage of accounting for protein wobble through variation of the order parameter S, which both improves fit convergence and provides greater detail on the orientation distribution of the protein.

2.8 Multifrequency EPR

The most common experimental setup for continuous wave EPR is to use microwave radiation frequency of ~9.5 GHz with a magnetic field strength of ~3500 G (X-band). However, Eq. 11 indicates that many combinations of radiation frequency and magnetic field strength will allow for resonance. Indeed, early EPR experiments used frequencies and field strengths ten times less than these [105]. Using higher frequencies and field strengths often affords greater spectral resolution and sensitivity [106], however there are technical limitations in terms of resonator composition and standing wave quality that impact its usefulness. These problems are gradually being overcome, with Q-band (35 GHz) and W-band (95 GHz) measurements becoming more accessible [107, 108].

The difference in resolution is apparent from EPR spectra acquired at different frequency bands (Fig. 21). While the spectral spitting defined by $T_{\parallel}'$ is relatively unaffected by radiation frequency, the central resonance position as defined by the electron g factor becomes more sensitive to spin probe orientation with increasing radiation frequency. This can be understood by the resonance equation (Eq. 12). The first term in Eq. 12, which defines the EPR spectrum's central resonance position, is linearly dependent on radiation frequency. In contrast, the second term, which defines the low and high field resonance positions, is independent of radiation frequency. The end result is that at higher radiation frequency, EPR spectra corresponding to different probe orientations overlap less, such that g and T can be determined with greater accuracy.

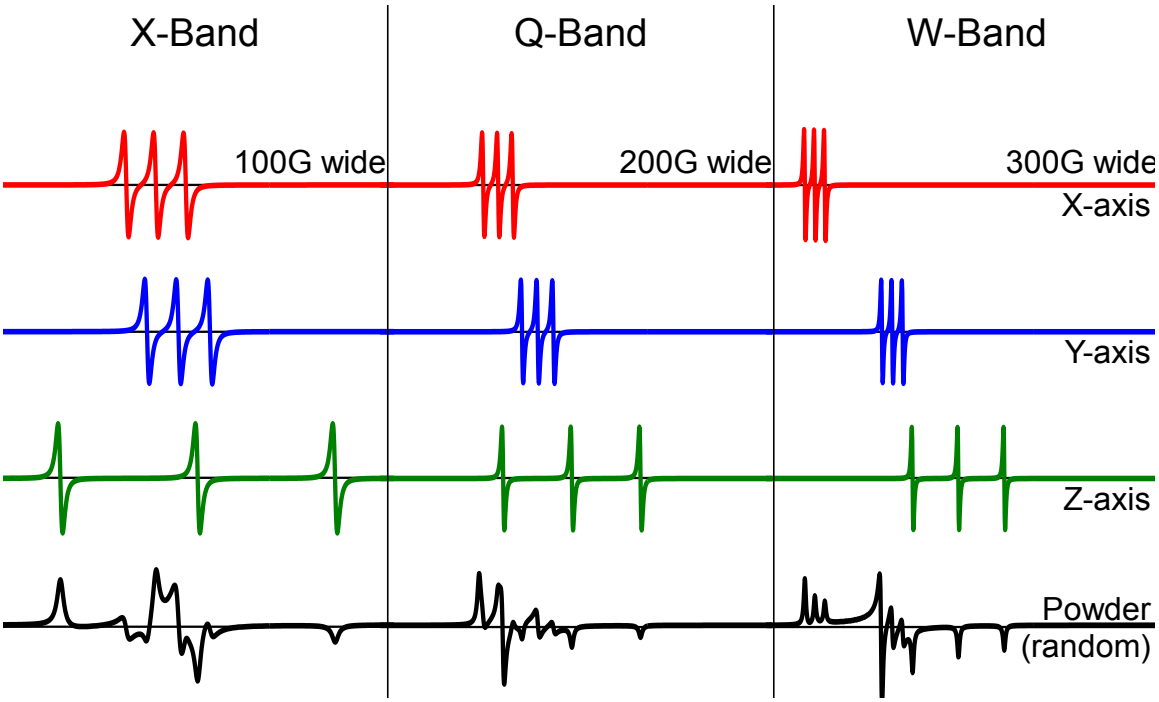

Fig. 21. Multifrequency EPR. Simulated spectra of a typical nitroxide label with magnetic field oriented along the label's x (red), y (blue), and z (green) axis, along with isotropic orientation (black) at X, Q, and W microwave frequency bands. As the microwave frequency is increased, the oriented components overlap less and less. This is also observed by the increasing complexity (number of lines) in the powder spectrum (bottom). Therefore, higher frequency bands possess greater orientation sensitivity.

2.9 EPR Data Analysis

EPR spectra can be analyzed in several different ways, depending on the type of experiment and conclusions desired. The most qualitative analysis involves noting general changes in EPR lineshape, indicative of some structural transition taking place in the sample. While this is useful during acquisition to verify sample preparation and compare previous hypotheses, more rigorous analysis is certainly possible (Fig. 22).

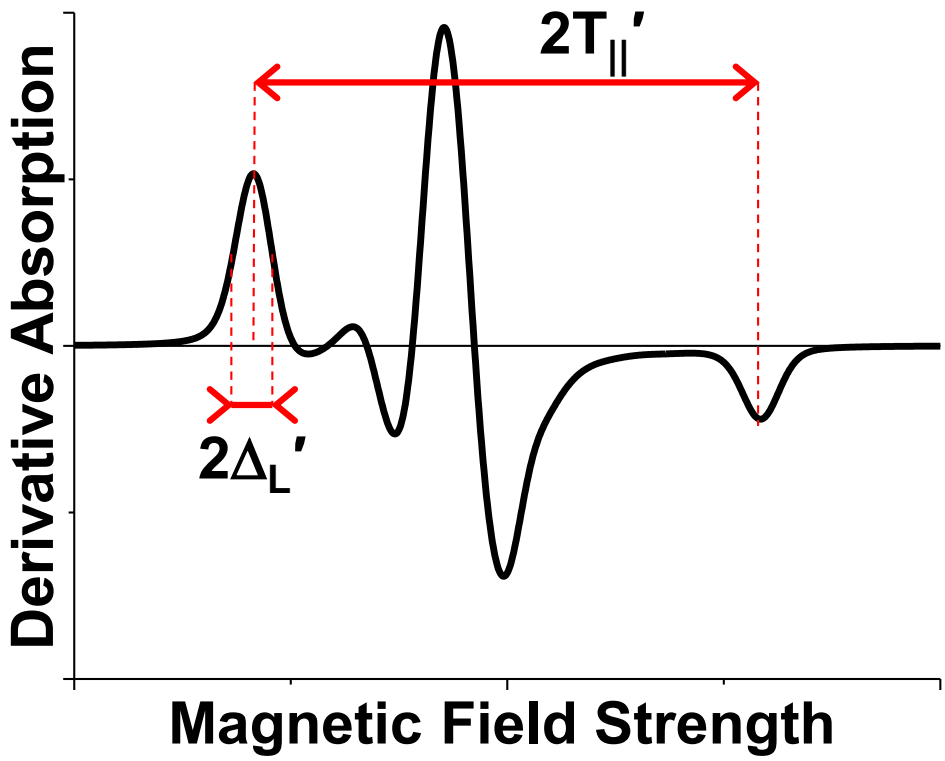

Fig. 22. EPR spectrum lineshape measurements. A conventional EPR spectrum is typically characterized by the splitting between the low and high field resonances ($2T_{||}'$) and the linewidth of the low field resonance ($2\Delta_L'$). These measurements can be used to determine rotational mobility and spin-spin interactions.

Measuring the distance in magnetic field units between the low and high resonance lines (splitting) is a way to calculate spin label mobility, as an increase in the rate of rotational diffusion will cause this splitting to decrease:

$$\tau_R = (5.4 \times 10^{-10} s)\left[1 - T_{||}'/T_{||}\right]^{-1.36} \qquad \text{Eq. 23}$$

where $T_{||}'$ is the splitting for the sample of interest, and $T_{||}$ is the splitting of an immobilized version of the sample. Eq. 23 is an empirical formula valid for spin-labeled proteins exhibiting slow, restricted motion [109].

Also of interest is the width of the resonance lines (linewidth), although unlike the splitting, the linewidth is affected by multiple phenomena, including the rate of rotational

diffusion and presence of neighboring spin labels via spin-spin interaction. In the case of dilute spin label, an equation similar to Eq. 23 can be used in conjunction with the linewidth (as measured from the low field resonance line as half width at half maximum Δ_L'):

$$\tau_R = (1.16 \times 10^{-8} s)[1 - \Delta_L'/\Delta_L]^{-0.943} \qquad \text{Eq. 24}$$

where again, the primed quantity refers to the sample as perturbed by rotational diffusion, and the unprimed quantity refers to the immobilized sample. Eq. 24 is valid for slow, restricted motion as well, although Eq. 23 is typically used instead of Eq. 24, due to possible effects from spin-spin interactions.

Determining the order parameter S from EPR spectra is commonly accomplished using Eq. 21, assuming the protein undergoes rapid restricted motion [110]. The spectral splitting corresponding to the protein sample of interest ($2T_{\|}'$), a fully immobilized protein sample ($2T_{\|}$), and a rapid isotropic protein sample ($2T_0$) are required, so typically multiple samples of the same protein must be prepared. Freezing or lyophilizing the protein can be used to obtain $T_{\|}'$, while heating or truncating the protein in solution can be used to obtain T_0.

Saturation transfer EPR spectra are analyzed based on peak height ratios and integrated intensity. These have been measured previously for spin-labeled hemoglobin, a well-characterized globular protein with a known rotational correlation time based on the Stokes-Einstein formula (Eq. 17) [111]. This spin-labeled hemoglobin was mixed into solutions containing a specific amount of glycerol to produce a desired viscosity, and thus a variety of rotational correlation times. The peak height ratios were measured from the

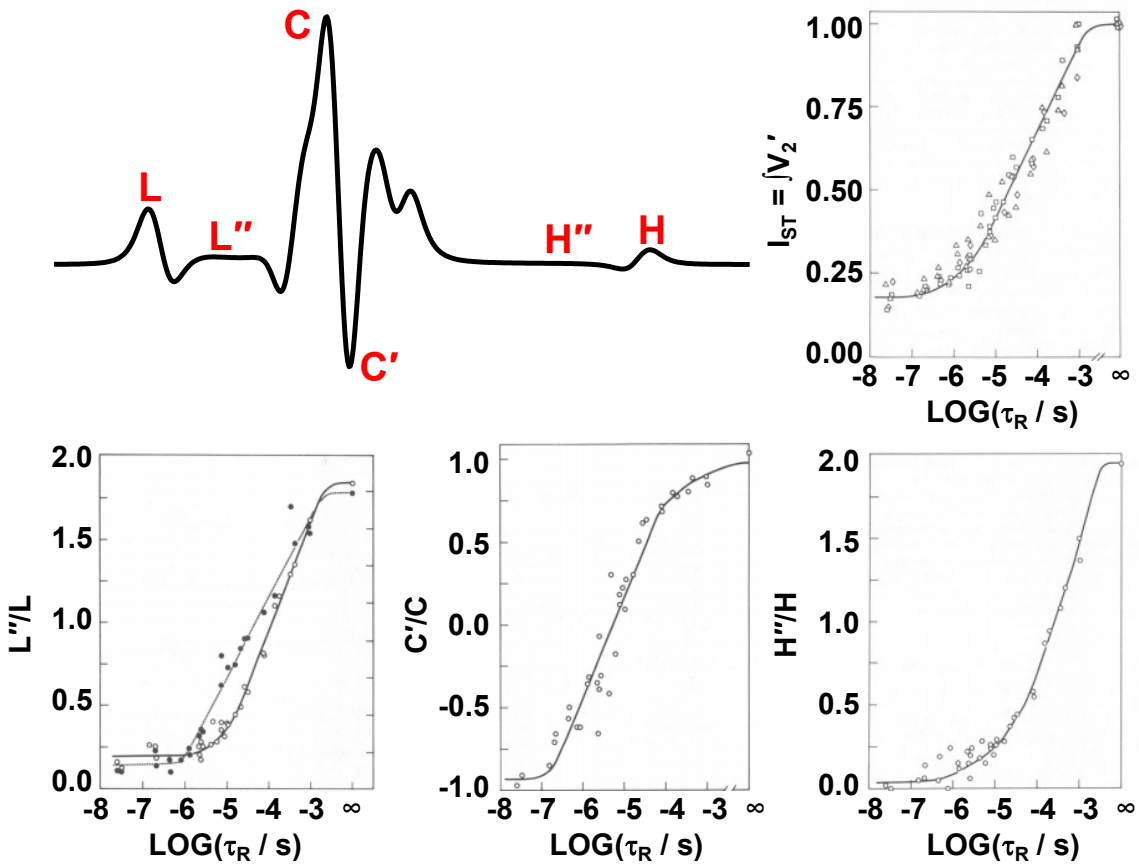

Fig. 23. Measuring rotational diffusion from saturation transfer EPR. STEPR spectra are analyzed by measuring intensities at specific locations in the spectrum (red, top left) or the integral of the spectrum (integrated intensity, I_{ST}). These values are then compared to correlation time plots obtained with standard samples of maleimide spin labeled hemoglobin in glycerol to determine the rotational correlation time for the sample of interest. Figures adapted from [111].

saturation transfer EPR spectra, and plotted against the calculated rotational correlation times. Using these plots, a sample with an unknown rotational correlation time can be determined from the peak height ratios or the integrated intensity measured from the saturation transfer EPR spectrum. The integrated intensity parameter is commonly used in STEPR analysis, due to its minimal sensitivity to orientation anisotropy and well-defined value, though C′/C is also common due to even less sensitivity to orientation anisotropy [112].

Precisely determining the rate and amplitude of rotational diffusion, as well as orientation distributions, requires analysis of EPR spectra beyond lineshape measurements. In these cases, we can fit EPR spectra through least-squares minimization and spectral simulation [113]. For a rigid limit (τ_R > 100 ns) sample containing one or several orientations, the simulation is relatively straightforward, as there are static and well-defined magnetic parameters corresponding to non-exchanging states, at least on the EPR timescale defined by T_2 relaxation. Additionally, if the diffusion is much faster than T_2, then we recover an isotropic case with complete averaging and a single state. The simulation becomes more complicated when rotational diffusion on the order of T_2 is present, due to multiple states and incomplete rotational averaging generating additional

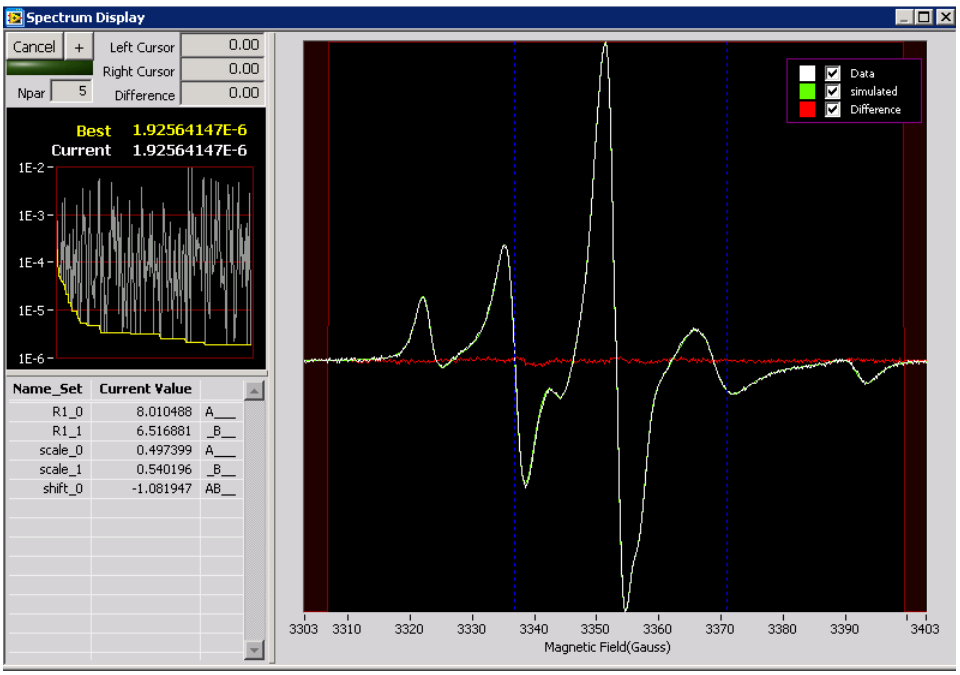

Fig. 24. Fitting of EPR spectra by simulation. Conventional EPR spectra of nitroxide spin labels can be simulated and fit by least squares minimization (right). Key parameters of the EPR spectrum, including electron g, hyperfine T, rotational diffusion τ_R, order parameter S, and probe orientation θ, ϕ (left) can be systematically varied to produce the best fit. Screenshot from MultiComponent by Christian Altenbach [89].

states. However, several dedicated EPR simulation programs have been developed by Jack Freed, David Schneider, and David Budil [110, 113, 114]. These programs utilize Sturm-Lioville theory along with parallelized matrix calculations.to quickly simulate these slow, but not immobilized, EPR spectra. As a result, we can simulate conventional EPR spectra of nitroxide spin labels in the fast, intermediate, and slow limits.

Fitting EPR spectra by simulation can be challenging due to the number of variables in the fit. A typical EPR simulation model will contain ~10 parameters unique to the sample, including but not limited to electron g tensor, hyperfine T tensor, rotational diffusion tensor, and order parameter. Assumptions are often employed to constrain these fits, including previous measurements on similar samples (frozen, randomly oriented, etc), and physical considerations like axial or isotropic symmetries. Additionally, only a few parameters are varied at one time, and correlation matrices produced by the fitting software can be consulted to control for overparameterization. Global fitting of several related sample spectra (parallel/perpendicular bicelles, X/Q-band, etc) is also a common tactic. Several models are often compared, as the concept of a ‘best’ model is somewhat elusive. Despite these shortcomings, this is perhaps the most quantitative method of EPR data analysis.

Chapter 3. Protein-Protein Interactions in Calcium Transport Regulation Probed by Saturation Transfer Electron Paramagnetic Resonance

Zachary M. James[Δ], Jesse E. McCaffrey[Δ], Kurt D. Torgersen, Christine B. Karim, and David D. Thomas[*]

Department of Biochemistry, Molecular Biology, and Biophysics, University of Minnesota, Minneapolis, MN 55455

Δ ZMJ and JEM contributed equally to this work
* To whom correspondence should be addressed: ddt@umn.edu

Published in *Biophysical Journal*, Vol. 103, pp. 1370 – 78.

3.1 Summary

We have used electron paramagnetic resonance (EPR) to probe the homo- and hetero-oligomeric interactions of reconstituted sarcoplasmic reticulum Ca-ATPase (SERCA) and its regulator phospholamban (PLB). SERCA is responsible for restoring calcium to the sarcoplasmic reticulum to allow muscle relaxation, while PLB inhibits cardiac SERCA unless phosphorylated at Ser16. To determine whether changes in protein association play essential roles in regulation, we detected the microsecond rotational diffusion of both proteins using saturation transfer EPR (STEPR). Peptide synthesis was used to create a fully functional and monomeric PLB mutant with a spin label rigidly coupled to the backbone of the transmembrane helix, while SERCA was reacted with a Cys-specific spin label. STEPR revealed that sufficiently high lipid/protein ratios minimized self-association for both proteins. Under these dilute conditions, labeled PLB was substantially immobilized following co-reconstitution with unlabeled SERCA, reflecting their association to form the regulatory complex. Ser16 phosphorylation slightly increased this immobilization. Complementary measurements with labeled SERCA showed no change in mobility following co-reconstitution with unlabeled PLB, regardless of its phosphorylation state. We conclude that phosphorylating monomeric PLB can relieve SERCA inhibition without changes in the oligomeric states of these proteins, indicating a structural rearrangement within the heterodimeric regulatory complex.

3.2 Introduction

Muscle relaxation is induced by the active transport of Ca^{2+} from the cytoplasm into the sarcoplasmic reticulum (SR). The SR Ca^{2+}-ATPase (SERCA) is a 994-residue enzyme that transports two Ca^{2+} into the SR lumen per ATP hydrolyzed (Fig. 25, left) [12], resulting in muscle relaxation. In cardiac and slow-twitch muscle, SERCA activity

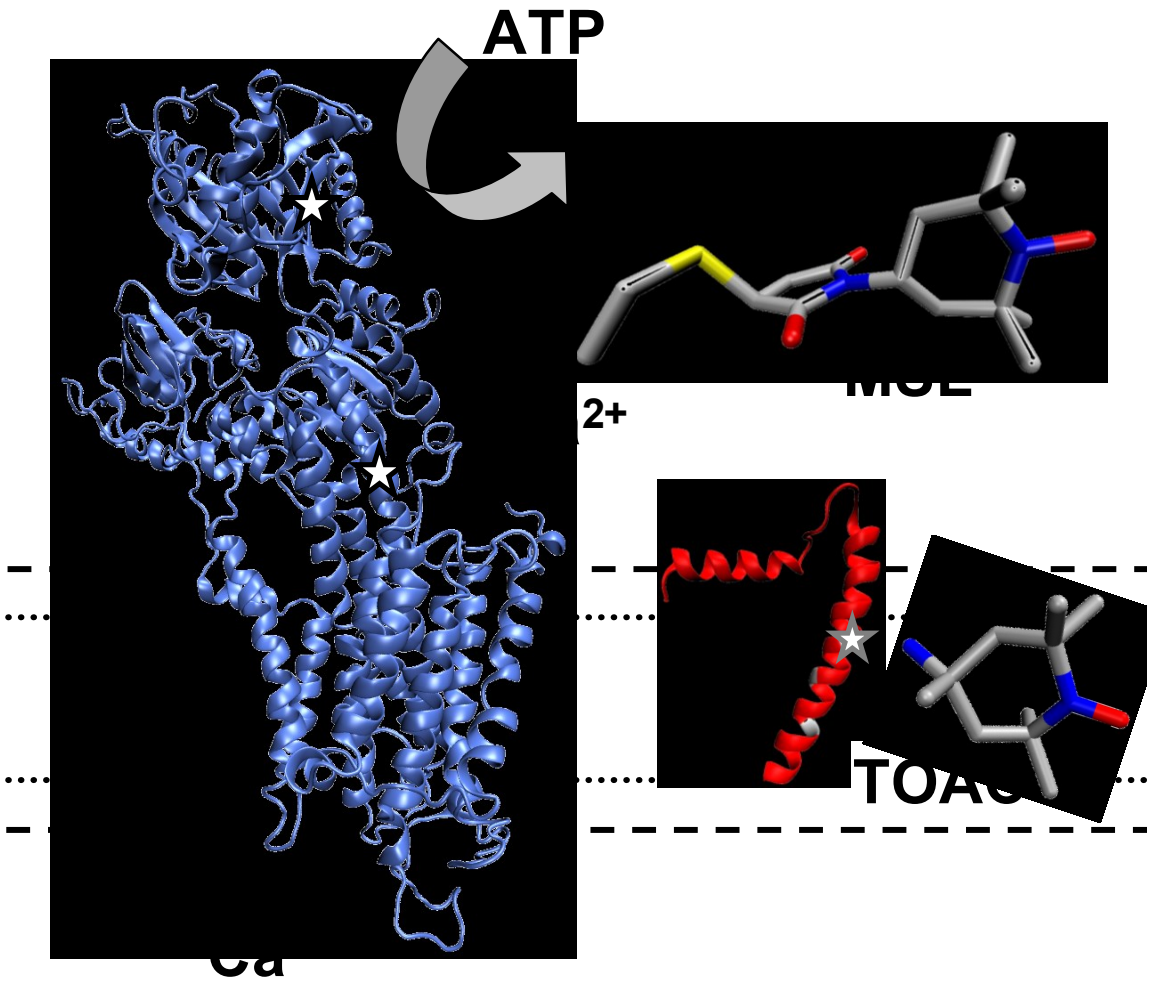

Fig. 25. Structural models of SERCA (left, crystal structure 1IWO [11]) and monomeric PLB (right, hybrid NMR structure 2KB7 [22]). All experiments in this study were conducted with the monomeric form of PLB. The amino acid TOAC (bottom right), containing a nitroxide spin label rigidly coupled to the α-carbon, is incorporated at position 36 (gray star) on PLB; PLB residues 41 and 46 (gray) are mutated to Phe and Ala. For unlabeled PLB, position 36 is Ala. For spin-labeled SERCA, MSL (top right) is attached at Cys 344/Cys 364 (black star) [115].

is allosterically regulated by phospholamban (PLB) [10], a 52-residue membrane protein consisting of a 30-residue transmembrane helix and a 16-residue cytosolic helix connected by a short, flexible loop [116] (Fig. 25, right). PLB inhibits SERCA by decreasing its apparent Ca^{2+} affinity (increasing K_{Ca}) [56]. SERCA inhibition is relieved physiologically either by micromolar [Ca^{2+}] or through PLB phosphorylation at S16 by protein kinase A [38], and can also be relieved by PLB point mutations [26, 117, 118].

The regulatory mechanism of the SERCA-PLB complex has considerable therapeutic relevance, since inadequate calcium transport has been strongly linked to heart failure [119]. Emerging treatments aim to improve cardiac performance by increasing SERCA activity through increased SERCA expression [120], allosteric activation of SERCA by small molecules [84], or reduced PLB inhibitory potency [80, 121]. Elucidating this mechanism would provide a roadmap for the rational design of PLB mutants and drugs designed to activate SERCA.

However, this regulatory mechanism remains controversial. Cross-linking [57] and immunoprecipitation [51] studies suggest that dissociation of the SERCA-PLB complex is required (Fig. 26, Dissociation Model), while spectroscopic studies suggest that PLB remains bound to SERCA following activation by Ser16 phosphorylation [25, 59, 60], Ca^{2+} addition [122], or PLB loss-of-function mutations [60, 80], indicating that a structural rearrangement within the complex can relieve inhibition (Fig. 26, Subunit Model). Furthermore, recent studies have identified multiple PLB conformations within the regulatory complex that correlate with different inhibitory states [25, 27].

3.2.1 Oligomeric interactions

Distinguishing these regulatory mechanisms is made more difficult by the variety of protein-protein interactions in this system. While the fundamental inhibitory complex is proposed to be a SERCA-PLB heterodimer [10, 30, 123] (Fig. 26, center), both proteins form homo-oligomers that can affect SERCA function (Fig. 26). SERCA may form functioning dimer and trimer states [124, 125], while larger aggregates lead to inhibition [126, 127]. Numerous studies have examined the oligomeric state of SERCA in native [128-130] and reconstituted [126] membranes, and several have investigated the role of the lipid/protein molar ratio (L/P) in modulating SERCA aggregation [127, 131, 132], all based on the proportionality between oligomeric size and rotational correlation time [133]. In cardiac SR, SERCA inhibition and aggregation are both relieved by micromolar Ca^{2+} or PLB phosphorylation [134]. Native PLB equilibrates between monomers and homopentamers, and the latter can be destabilized by mutation (typically

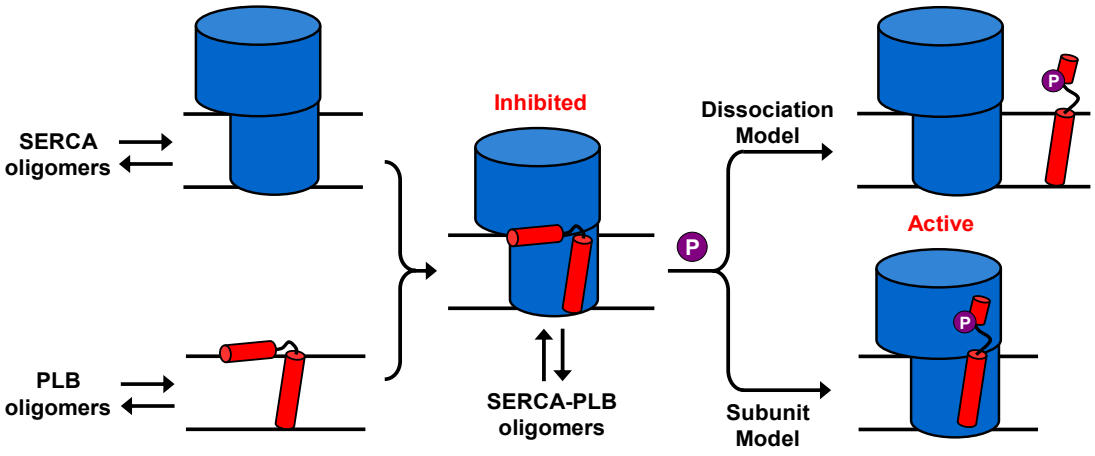

Fig. 26. Oligomeric interactions of SERCA and PLB. Both proteins have homo-oligomeric interactions (left), and bind to form an inhibited SERCA-PLB complex (center). Phosphorylation of PLB relieves inhibition (right), which may occur through dissociation of the complex (Dissociation Model), or a structural rearrangement within the complex (Subunit Model).

leading to increased SERCA inhibition) or stabilized by phosphorylation (leading to decreased SERCA inhibition). Thus inhibition depends, at least in part, on the concentration of PLB monomer [30]. To simplify analysis and focus on SERCA-PLB interactions, we have used (a) a monomeric PLB mutant (AFA-PLB, referred to below as PLB) [24] in which oligomerization is eliminated by replacing Cys residues 36, 41, and 46 with Ala, Phe, and Ala, respectively, and (b) sufficiently high lipid:protein molar ratios (L/P) to minimize self-association of both SERCA and PLB. Thus we are able to focus solely on the heterodimeric interactions between these two proteins.

In the present study, we have characterized the hetero-oligomerization of PLB and SERCA using electron paramagnetic resonance (EPR), while minimizing the homo-oligomerization of both proteins. Rotational motions detected by EPR can be sensitive to oligomeric interactions, since the rotational correlation time (τ_R) of the spin-labeled protein is proportional to the protein's transmembrane volume [133]. However, conventional EPR is sensitive only to correlation times in the nanosecond range, which is appropriate for rotation of aqueous proteins, but not membrane-embedded proteins, where the viscosity (and thus τ_R) is orders of magnitude greater. Even in fluid lipid bilayers, τ_R values for most integral membrane proteins are in the microsecond range. These slow rotational motions are best measured by saturation transfer EPR (STEPR) [135, 136], which requires the use of spin probes that are immobilized on the labeled protein. In the present study, PLB rotational motion was detected by incorporating the spin label TOAC (2,2,6,6-tetramethylpiperidine-1-oxyl-4-amino-4-carboxylic acid) into the peptide backbone at position 36 in the transmembrane helix (Fig. 25), while SERCA

rotational dynamics was detected after covalent reaction with a maleimide spin label (MSL). Both labels have been shown to be rigidly attached to their respective proteins, making them sensitive to rigid-body rotational diffusion that directly reflects the size of the oligomeric complex [23, 128]. We used STEPR to first find conditions where homo-oligomerization was minimized, and then to detect the formation of SERCA-PLB hetero-oligomers so as to discriminate between the Dissociation and Subunit models (Fig. 26).

3.3 Methods

3.3.1 Peptide synthesis

C36TOAC, C41F, C46A, PLB (36-TOAC-AFA-PLB) and C36A, C41F, C46A PLB (AFA-PLB) were synthesized as described previously [23, 98, 137]. Fmoc-TOAC was purchased from Toronto Research Chemicals (North York, Ontario) and Fmoc-protected amino acids were purchased from EMD Chemicals (Philadelphia, PA). Peptides were purified by reverse-phase HPLC on a preparative C8 column (Grace Vydac, Hesperia CA) using H_2O + 0.1% trifluoroacetic acid and isopropanol as mobile phases. Peptides were characterized by mass spectrometry and SDS-PAGE. Protein concentrations were quantified using a bicinchoninic acid (BCA) assay (Thermo Fisher Scientific, Rockford IL).

3.3.2 SERCA purification and spin labeling

SR vesicles were prepared from rabbit fast-twitch muscle [138], then resuspended to 25 mg/mL total protein in SR buffer (30 mM MOPS, 0.3 M sucrose, pH 7.0). SERCA

was purified by reactive red chromatography [139], omitting reducing agents. For spin labeling, SERCA was diluted to 10 mg/mL with SR buffer, to which 300 μM MSL was added from a 50 mM stock in dimethylformamide. After stirring 1 hr at 25 °C, labeled vesicles were diluted tenfold in SR buffer and centrifuged 45 min at 30,000*g* (4 °C) to remove unreacted MSL. The resulting pellet was resuspended in SR buffer and purified as above. Protein concentrations were quantified using a BCA assay.

3.3.3 Reconstitution of SERCA and PLB

Functional reconstitution of SERCA and PLB was carried out as described previously, using 4:1 DOPC/DOPE (mol/mol) to yield unilamellar vesicles that are optimal for reproducing physiological SERCA-PLB regulatory function [140, 141]. These vesicles have an average diameter of 100 nm [141] and thus rotate too slowly to affect our saturation transfer EPR spectra [142, 143]. Final buffer composition of EPR samples was 50 mM MOPS, 50 mM KCl, 5 mM $MgCl_2$, 0.5 mM EGTA, 210 μM $CaCl_2$, pH 7.0, resulting in pCa 6.5 to give optimal regulation of SERCA by PLB [122]. Identical buffer conditions were used in functional assays, except that $CaCl_2$ was varied in order to vary pCa ($-\log_{10}[Ca^{2+}]$). An enzyme-coupled ATPase assay was used to measure the Ca-dependence of SERCA activity as described previously [80, 140]. As in previous publications from our laboratory, EPR experiments were performed at 4 °C to maintain protein stability during lengthy STEPR experiments, while functional measurements were performed at 25 °C to enhance SERCA activity and permit comparison to published work. PLB inhibitory potency is only weakly dependent on

temperature [144]. For phosphorylation, the PLB/lipid/detergent mixture (containing 20 μM PLB, before SERCA addition) was incubated 2 hr at 25 °C with 200 IU/mL bovine protein kinase A catalytic subunit (Sigma, St. Louis MO) and 1 mM MgATP. Complete PLB phosphorylation (> 92%) was confirmed by quantitative Western blotting [145] using 10–20% tris-tricine gels (Bio-Rad, Hercules CA).

3.3.4 EPR spectroscopy and data analysis

Before EPR experiments, samples were centrifuged 1 hr at 200,000*g* (4 °C) and the pellets resuspended in minimal buffer. 40 μL samples were loaded into 22-gauge Teflon tubing (Amazon Supply, Miami Lakes FL) threaded through a glass capillary (Wiretrol, Drummond Scientific Company, Broomall PA) flame-sealed at one end. The Teflon tubing extended 1 cm from the end of the capillary and was plugged with Critoseal (Krackeler Scientific, Albany NY). Spectra were acquired at X-band (9.5 GHz) with a Bruker EleXsys E500 spectrometer equipped with the ER 4122 SHQ cavity. Temperature was maintained at 4 ± 0.2 °C with a quartz dewar insert and a nitrogen gas flow temperature controller. Spectra were acquired after sample deoxygenation under nitrogen gas (~1 hr) to eliminate the dependence of spectra on oxygen accessibility [111]. Microwave field amplitude H_1 (G) was calibrated with a solution of 0.9 mM PADS, 50 mM K_2CO_3 [111].

Spectral acquisition parameters were set according to Squier et al. [111]. Conventional (V_1, first harmonic, in-phase) EPR spectra were acquired with H_1 = 0.14 G microwave field amplitude, 100 kHz modulation frequency, 2 G modulation amplitude,

and 120 G sweep width. V_1 spectra used for normalization were acquired as above except that H_1 was set to 0.032 G. STEPR (V_2', second harmonic, out-of-phase) spectra were acquired with 50 kHz modulation frequency, 5 G modulation amplitude, and 120 G sweep width. After null phase determination by minimizing the signal at non-saturating microwave intensity (H_1 = 0.032 G), H_1 was increased to 0.25 G and the V_2' spectrum recorded. All EPR spectra were baseline-corrected and then normalized, either to $\iint V_1$ (conventional EPR) or to $\iint V_1 / H_1$ for H_1 = 0.032 G (STEPR). V_1 EPR spectra near the slow-motion limit were analyzed by evaluating lineshape features Δ_L' (the outer half-width of the low-field line, which increases with spin-spin interaction and rotational motion) and $2T_{\parallel}'$ (the splitting between outer extrema, which decreases with rotational motion but not with spin-spin interaction) [109, 146].

For V_2' spectra, effective rotational correlation times were calculated from an integrated intensity parameter (I_{ST}), using a correlation plot created from MSL-hemoglobin samples in glycerol [111]. I_{ST} reports an effective rotational correlation time that is minimally sensitive to modulation phase errors and thus provides greater precision than provided by lineshape parameters [111]. Data plots were produced with Origin 8.1. Error bars are SEM (n = 3-5). When no error bar is visible, this indicates that SEM is smaller than the plotted symbol.

3.4 Results

3.4.1 Functional Assays

To confirm that 36-TOAC-PLB retained regulatory function, we reconstituted it with SERCA into 4:1 (mol/mol) DOPC/DOPE (1,2-dioleoyl-*sn*-glycero-3-phosphocholine, 1,2-dioleoyl-sn-glycero-3-phosphoethanolamine) vesicles at 700 lipids/SERCA (mol/mol) and measured Ca-dependent ATPase activity using a coupled-enzyme assay [140]. Results were fit by the Hill equation (Eq. 25):

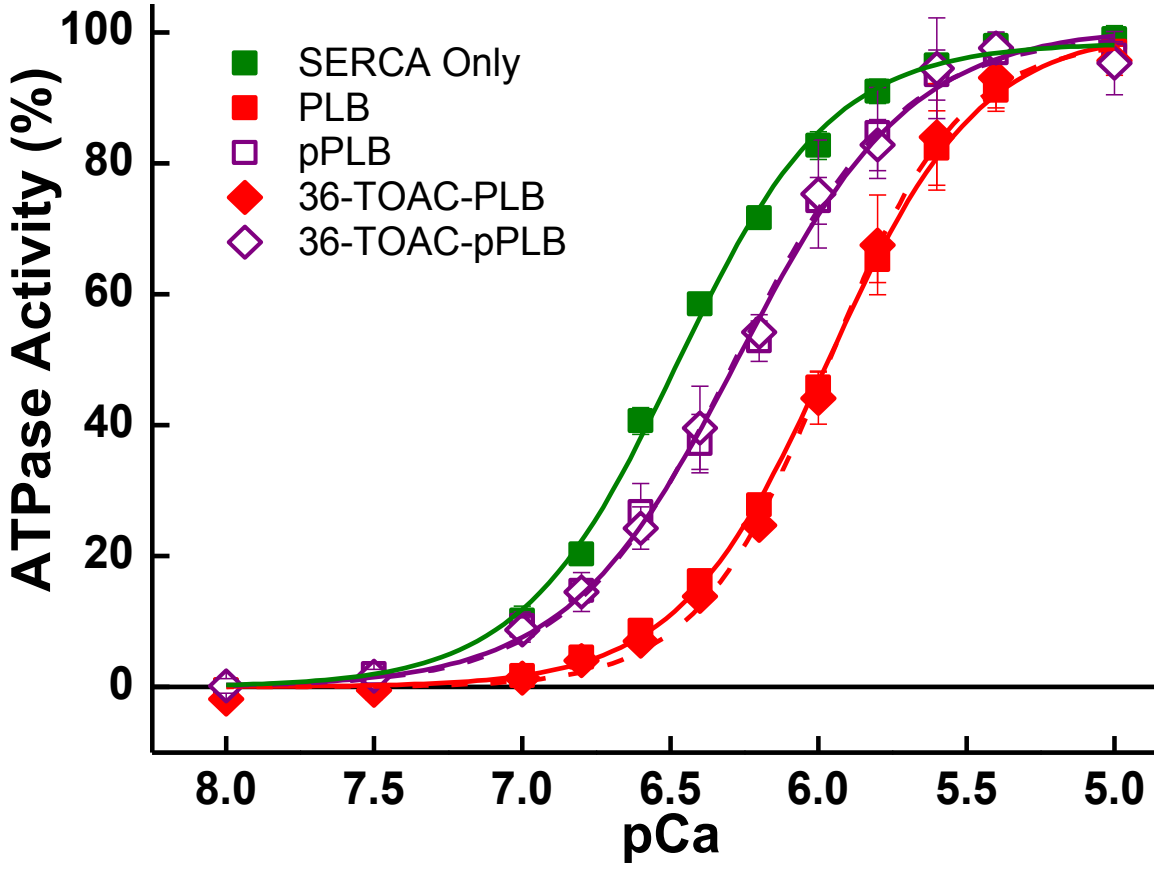

Fig. 27. Ca-dependence of ATPase activity. Samples were reconstituted at 700 lipids/SERCA and 10 PLB/SERCA (mol/mol). ATP turnover was measured at 25 °C, fit by Eq. 25, and normalized to V_{max}. SERCA-only controls (circles) were compared to samples containing PLB (closed squares), 36-TOAC-PLB (closed diamonds), and their pSer16 counterparts (open squares and diamonds). pK_{Ca} values obtained from the fits were used to quantify SERCA inhibition, and are summarized in Table S1.

$$V = \frac{V_{max}}{1 + 10^{-n \cdot (pKCa - pCa)}} \quad \text{Eq. 25}$$

where V is the ATPase rate, V_{max} is the ATPase rate at saturating [Ca^{2+}], n is the Hill coefficient, and pK_{Ca} is the pCa where activity is half-maximal. PLB inhibitory potency, defined as the decrease in pK_{Ca}, was indistinguishable between our spin-labeled construct and unlabeled PLB controls (Fig. 27). At 10 PLB/SERCA, where inhibition is maximal, pK_{Ca} shifted from 6.48 ± 0.01 to 6.00 ± 0.01 (inhibitory potency = 0.48 ± 0.02). When PLB was completely phosphorylated (> 92%), inhibition was partially reversed, increasing pK_{Ca} to 6.30 ± 0.01 (inhibitory potency = 0.18 ± 0.02) and restoring SERCA Ca sensitivity to the same extent as phosphorylating unlabeled PLB (Fig. 27). At 0.5 PLB/SERCA, matching the conditions of some experiments below, the inhibitory potency of 36-TOAC-PLB was 0.28 ± 0.03 (unphosphorylated) and 0.12 ± 0.04 (phosphorylated). These results, including the partial reversal of inhibition by phosphorylation, are similar to those reported previously for other PLB derivatives [23, 25] and demonstrate that 36-TOAC-PLB regulates SERCA normally. We also used functional assays to determine whether reacting SERCA with MSL affected its interaction with PLB. While MSL decreased V_{max} by ~30% as reported previously [130], pK_{Ca} regulation by PLB was unaltered, indicating that the label does not perturb regulatory interactions between the two proteins.

3.4.2 Monomeric mutant AFA-PLB does not aggregate

Our goal was to find conditions in which self-association is minimized for both PLB and SERCA. We used conventional and saturation transfer EPR to examine spin-

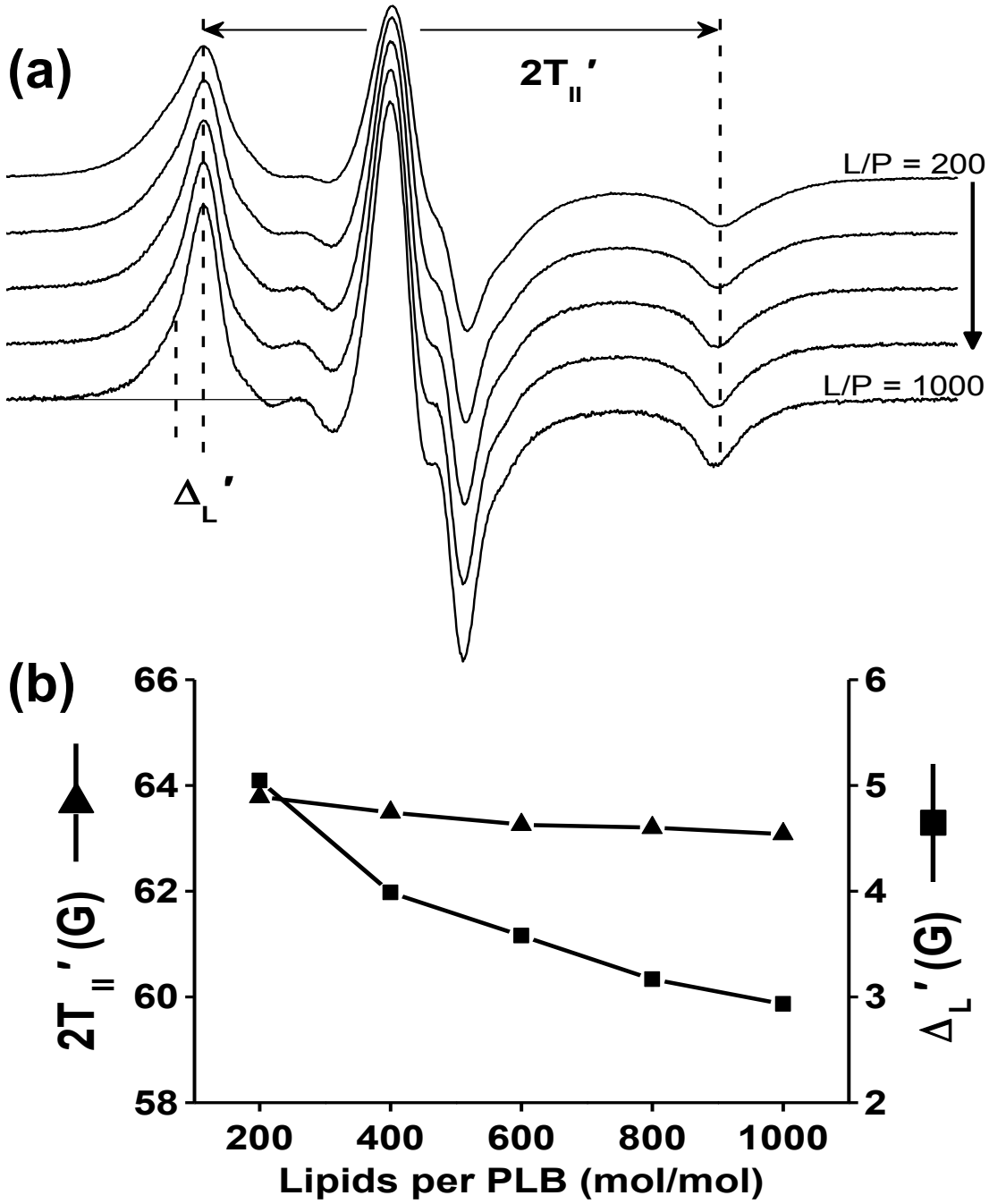

Fig. 28. Dependence of conventional EPR spectra of 36-TOAC-PLB on lipid/protein ratio. **(a)** Spectra of 36-TOAC-PLB reconstituted at 200–1000 L/P **(b)** Outer splitting ($2T_{||}'$, squares) and low-field outer linewidth (Δ_L', triangles) as a function of L/P. The vertical scales were set so that a change in rotational motion would yield changes in Δ_L' and $2T_{||}'$ of similar magnitude (but opposite sign) [109, 146]. STEPR spectra are given in Fig. S34.

labeled PLB or SERCA reconstituted at several L/P. Conventional EPR of 36-TOAC-PLB detected only a marginal decrease in outer splitting ($2T_{\parallel}'$, Fig. 28) with increasing L/P, indicating little or no change in nanosecond rotational dynamics. However, lipid dilution did lead to a substantial decrease in the linewidth (Δ_L') (Fig. 28b), which could arise from decreased nanosecond rotational mobility [109, 146], but this is inconsistent with the lack of increased splitting (Fig. 28b). Thus the linewidth decrease is due to decreased dipolar broadening from spin-spin interactions, but the observed broadening is precisely that expected for a random two-dimensional arrangement of monomers in the membrane [147], and would be much greater if PLB oligomers were present, as demonstrated by Fig. S32 and Fig. S33. STEPR spectra support this interpretation (Fig. S36). Thus this PLB construct remains predominantly monomeric at all L/P tested here.

3.4.3 SERCA does not aggregate above 600 L/P

We conducted similar lipid-dilution experiments with MSL-SERCA. Conventional EPR spectra (Fig. S35) have no significant dependence on L/P, confirming the previous finding that this spin label binds rigidly to SERCA and undergoes no nanosecond rotational dynamics [128]. Thus any changes in STEPR spectra (Fig. 29a) are due to changes in microsecond rotational motion of SERCA about an axis perpendicular to the membrane [128]. These STEPR spectra show that the effective rotational correlation time τ_R decreases substantially from L/P = 200 to 600, to a limiting value of ~12 μs for L/P > 600. This τ_R is consistent with the rotational diffusion of monomeric or dimeric SERCA [129] based on the Saffman-Delbrück equation [133], which predicts

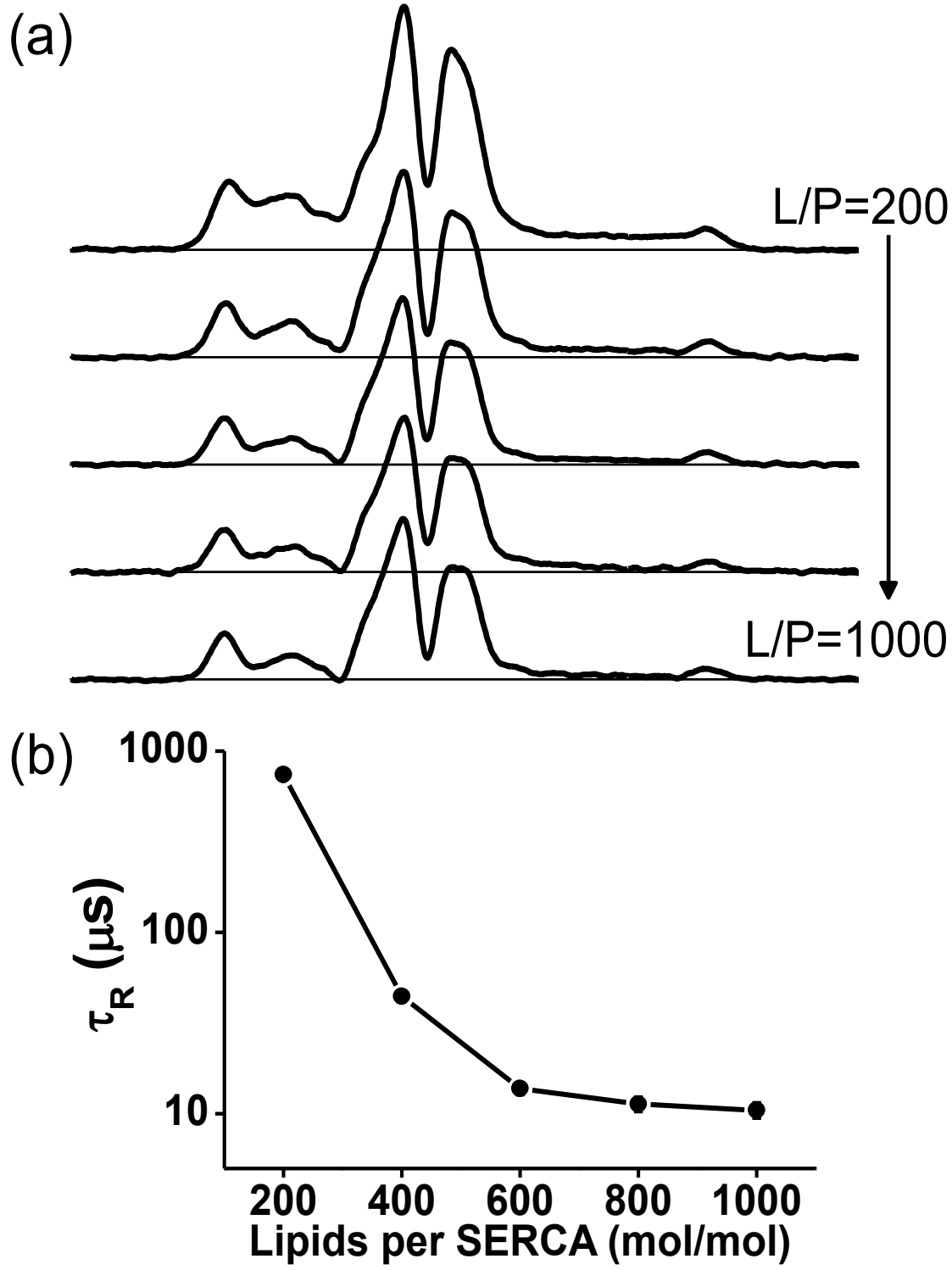

Fig. 29. STEPR of MSL-SERCA as a function of lipid/protein molar ratio (L/P). (a) Representative STEPR (V_2') spectra of reconstituted MSL-SERCA. (b) Effective rotational correlation times (τ_R). Conventional EPR (V_1) spectra are given in Fig. S35.

that τ_R is proportional to protein transmembrane volume and lipid viscosity. Assuming a membrane height of 4 nm [148] and membrane viscosity of 2 – 5 P [149], the Saffman-Delbrück model yields correlation times of 2 – 4 μs and 8 – 19 μs for SERCA monomers and dimers, respectively. We conclude that SERCA undergoes concentration-dependent self-association, but that this dependence is negligible for L/P > 600, suggesting the presence of stable SERCA monomers or small oligomers. Therefore, further experiments were performed at 700 lipids per SERCA to eliminate the formation of homo-oligomers, allowing us to focus on the SERCA-PLB interaction.

3.4.4 Effects of phosphorylation and SERCA binding on rotational dynamics of spin-labeled PLB

We co-reconstituted 36-TOAC-PLB with SERCA to investigate PLB rotational dynamics within the regulatory complex, using 700 lipids/SERCA and 2 SERCA/PLB to minimize both homo-oligomers and unbound PLB. Conventional EPR spectra of co-reconstituted samples (PLB + SERCA, pPLB + SERCA) and their PLB-only controls (PLB, pPLB) are all near the rigid limit and are virtually identical (Fig. 30a,c), indicating no change in nanosecond dynamics or self-association of PLB upon phosphorylation and/or SERCA binding. The V_1 EPR spectra in Fig. 30a contain subtle 'shoulders' on the low- and high-field peaks. These could arise from spin-spin interactions (Fig. 28, Fig. S32) or the presence of slow restricted-amplitude rotation [150]. However, the V_1 spectra are not affected by phosphorylation and/or SERCA addition, so the effects on V_2' spectra (Fig. 30b) must arise from changes in microsecond rotational dynamics.

In contrast to the invariant conventional (V_1) spectra (Fig. 30a,c), STEPR (V_2') revealed significant changes in microsecond dynamics (Fig. 30b,d). SERCA decreased PLB mobility substantially, with τ_R increasing from 1.9 ± 0.4 μs (PLB) to 5.6 ± 0.2 μs (PLB + SERCA), consistent with the large increase in SERCA binding. Ser16 phosphorylation had no significant effect on PLB dynamics in the absence of SERCA (Fig. 30b,d), but increased τ_R slightly in the presence of SERCA, from 5.6 ± 0.2 μs to 6.5 ± 0.1 μs (Fig. 30d). This larger τ_R is probably not due to increased binding to SERCA (since that would increase inhibition) or to increased PLB aggregation (since that is

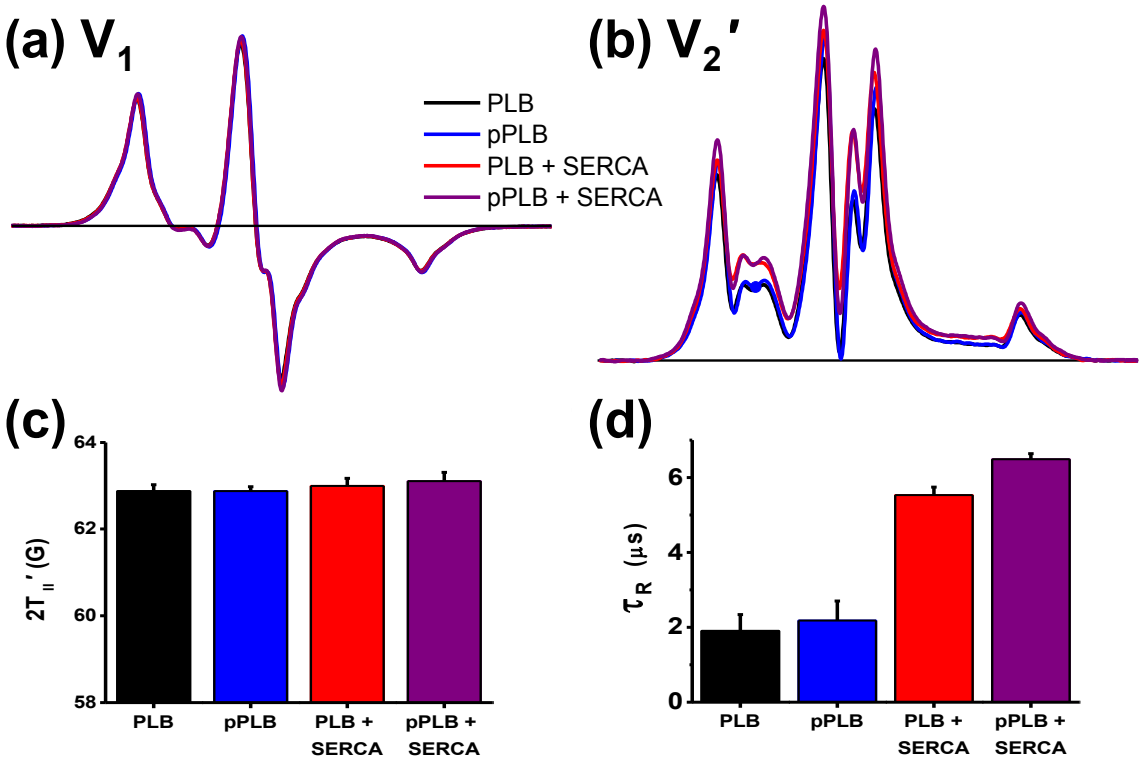

Fig. 30. Effects of Ser16 phosphorylation and SERCA on EPR of 36-TOAC-PLB. **(a)** Conventional (V_1) EPR spectra and **(b)** STEPR (V_2') spectra of 36-TOAC-PLB as affected by phosphorylation (pPLB) and/or SERCA (2 SERCA/PLB). **(c)** Outer splitting $2T_{||}'$ measured from conventional EPR spectra in (a). **(d)** Effective rotational correlation times from STEPR spectra in (b). Typical normalized spectra are shown in (a) and (b). Bar graphs in (c) and (d) show mean values and SEM for n = 3-5 trials.

inconsistent with the V_1 spectra in Fig. 30a), so it must be due to some structural change of the SERCA-PLB complex that alters either the tilt of the PLB TM domain or the frictional interaction of the SERCA-PLB complex with lipid [112, 151, 152]. In any case, it is clear that PLB does not dissociate from SERCA following phosphorylation, since this would cause a substantial *decrease* in the rotational correlation time, making the blue (pPLB) and purple (pPLB + SERCA) spectra identical (Fig. 30c,d). Indeed, a slight *increase* in τ_R was observed due to phosphorylation (Fig. 30d), and the blue and purple spectra are quite different (Fig. 30c), so Fig. 30 clearly contradicts the Dissociation Model and strongly supports the Subunit Model (Fig. 26).

3.4.5 Rotational dynamics of spin-labeled SERCA reconstituted with PLB

To determine whether the results of Fig. 30 were affected by changes in SERCA aggregation, we performed identical experiments except using MSL-SERCA and unlabeled PLB. Both V_1 (Fig. S36) and V_2' (Fig. 31) detect no change in SERCA rotational dynamics due to PLB or pPLB. The addition of 0.5 PLB per SERCA should increase the transmembrane volume (and thus the rotational correlation time) by only ~5% [133], within the experimental error of our measurements (~10%, Fig. 30d). This indicates that the aggregation state of SERCA is not significantly perturbed by PLB binding or phosphorylation under these dilute conditions (700 lipids/SERCA and 2 SERCA/PLB), despite substantial functional effects. These findings indicate that regulatory effects of PLB do not arise solely from modulating SERCA aggregation,

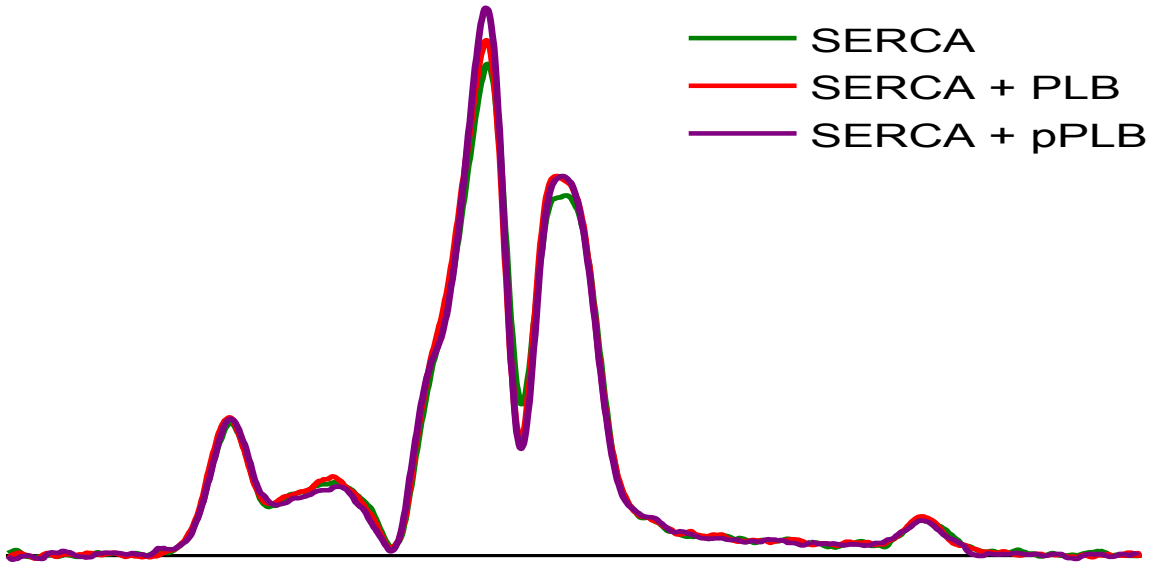

Fig. 31. STEPR (V_2') spectra of MSL-SERCA. Experimental conditions are as in Fig. 30, using MSL-SERCA and unlabeled PLB. Rotational correlation times did not vary significantly among these samples and were consistent with the data in Fig. 29 at 700 lipids/SERCA (13 ± 4 μs). Conventional EPR spectra also showed no significant changes (Fig. S36).

although such phosphorylation-dependent aggregation does contribute to functional regulation in cardiac SR [134].

Rotational correlation times determined from STEPR spectra are effective, and depend on several parameters that are not easily controlled or evaluated, such as probe orientation relative to the diffusion axis [153] and spin label environment [111]. In addition, it is likely that the TM domain of PLB has residual small-amplitude rotational flexibility relative to SERCA. These factors probably contribute to the significant differences between the V_1 spectra of the SERCA-PLB complex with labeled PLB (Fig. 30a) or labeled SERCA (Fig. S36), and to the shorter τ_R values determined from V_2' spectra of the complex with labeled PLB (Fig. 30b), compared to labeled SERCA (Fig. 31). Therefore, our key conclusions come from comparing the V_2' spectra of a particular spin-labeled protein (36-TOAC-PLB or MSL-SERCA), as perturbed by factors (protein-

protein interactions, protein concentration, and phosphorylation) that do not affect the V_1 spectra.

3.5 Discussion

We have used EPR to investigate the tendencies of SERCA and the monomeric AFA-PLB to form homo- and hetero-oligomers in reconstituted membranes. By systematically varying the lipid/protein molar ratio (L/P), we found that SERCA self-association occurs at low L/P but is eliminated for L/P > 600 (Fig. 29), even in the presence of 0.5 PLB/SERCA (Fig. 31). We also showed that TOAC-labeled PLB does not self-associate under the conditions of this study (Fig. 28). Thus the data in Fig. 30 reflect directly the rotational dynamics of PLB alone or in complex with SERCA. Since phosphorylation and SERCA binding caused no significant effects on PLB nanosecond dynamics as detected by conventional EPR (Fig. 30, left), the changes in STEPR (Fig. 30, right) are due to microsecond rigid-body dynamics of PLB. Thus SERCA does immobilize PLB by binding it, but phosphorylation does not dissociate PLB from SERCA, supporting the Subunit Model (Fig. 26, bottom right).

3.5.1 AFA-PLB is monomeric in lipid bilayers at high L/P, even after phosphorylation

While the null-Cys PLB mutant AAA-PLB, similar to AFA-PLB, was found previously to be monomeric by SDS-PAGE [137, 154], solid-state NMR studies suggested that AAA-PLB is substantially aggregated in reconstituted membranes at the

extremely low L/P value of 20 [155]. 36-TOAC-AFA-PLB shows substantial broadening of the V_1 spectrum at 20 L/P, consistent with aggregation (Fig. S32), along with dramatic effects on the V_2' spectrum (Fig. S33), showing that PLB aggregation is detectable if present. In contrast, our EPR experiments performed between 200 and 1000 L/P did not reveal significant PLB aggregation (Fig. 28). This is the most direct demonstration to date that AFA-PLB behaves as a monomer in reconstituted bilayers, whether phosphorylated or not. In previous studies, it was shown that the pentameric propensity of wild-type PLB increases with phosphorylation [30], and that SERCA preferentially binds to the PLB monomer [156]. Thus it remains likely that the decrease in PLB monomer concentration due to phosphorylation plays a significant role in relieving SERCA inhibition [30, 157]. However, the present results show that some relief of inhibition by phosphorylation occurs even under conditions where PLB oligomers do not form.

3.5.2 SERCA self-association occurs only at low L/P and is not induced by PLB at high L/P

The oligomeric state of SERCA for optimal function has been postulated to range from monomeric to tetrameric [125, 129, 158-160], while larger aggregates have been shown to decrease SERCA activity, whether induced by crosslinking [161], cationic peptides [162, 163], cationic local anesthetics [164], mismatch in lipid bilayer thickness [165], small-molecule SERCA inhibitors [124, 166], or PLB [134, 167]. Most importantly, inhibition relief in cardiac SR by either Ca^{2+} or phosphorylation correlates

with decreased SERCA aggregation [134]. The present study does not contradict these findings; SERCA aggregation probably plays a significant physiological role in both skeletal and cardiac SR. However, our results show that at low protein concentrations in the membrane (at high L/P), significant changes in SERCA inhibition by PLB occur without significant changes in SERCA aggregation (Fig. 31).

3.5.3 Binding of TOAC-spin-labeled PLB to SERCA is clearly detected by STEPR

STEPR shows that reconstitution with SERCA decreases the microsecond mobility of 36-TOAC-AFA-PLB substantially, consistent with binding (Fig. 30b&d), while conventional EPR detects no change in nanosecond motion or PLB aggregation. This complex formation is consistent with FRET from SERCA to PLB in a similar reconstituted system [27].

3.5.4 Phosphorylation causes a structural change in the SERCA-PLB complex, not dissociation

Phosphorylation of SERCA-bound PLB at Ser16 does not increase its rotational mobility, and thus does not dissociate it from SERCA under conditions of our study (Fig. 30). In fact, an increase in the effective rotational correlation time is observed, indicating a structural change in the SERCA-PLB complex that decreases mobility or changes the tilt of the PLB TM domain. This result supports the Subunit Model (Fig. 26, bottom right), though future studies are needed to characterize the structural change. Since the

concentrations of SERCA and PLB, as well as the PLB/SERCA ratio, are much higher in cardiac SR than in the samples considered here, it is unlikely that phosphorylation of PLB causes significant dissociation under physiological conditions. While previous studies have found that PLB is in dynamic equilibrium between free and SERCA-bound states [35, 80], our data indicates that PLB phosphorylation does not perturb this binding equilibrium significantly.

The present study used the SERCA1a isoform from skeletal SR. There is no known difference between the functional or physical interaction of PLB with SERCA1a and SERCA2a [17, 157, 168], but future studies with the SERCA2a isoform will be needed to rule this out. Previous studies using spin or fluorescent probes of phosphorylated PLB interacting with SERCA are consistent with the conclusions of the present study [25, 59, 60]. However, this is the first study of the SERCA-PLB interaction using a probe rigidly coupled to the transmembrane domain of PLB, thus reporting reliably the rotational mobility of PLB and showing that Ser16 phosphorylation does not dissociate the inhibitory transmembrane domain [137] of PLB from SERCA.

3.6 Conclusions

We have used STEPR to detect the microsecond rotational mobilities of SERCA and AFA-PLB in reconstituted membranes, providing direct insight into their oligomeric interactions, as perturbed by phosphorylation. At L/P $\geq$ 600 and PLB/SERCA = 0.5, SERCA does not change its state of self association due to PLB or pPLB, both of which are strongly immobilized by SERCA binding. Under these conditions, relief of SERCA

inhibition must be due to a structural change within the SERCA-PLB complex, not to dissociation of the complex.

3.7 Acknowledgments

This work was supported in part by NIH grants GM27906 and AR057220 to DDT. ZMJ was supported by NIH Training Grants AR007612 and GM008700, JEM was supported by NIH Training Grant AR007612, and KDT was supported by a Predoctoral Fellowship from the American Heart Association (0615710Z). EPR experiments were performed at the Biophysical Spectroscopy Center. Computational resources were provided by the Minnesota Supercomputing Institute. We thank Edmund Howard, Ryan Mello, and Yuri Nesmelov for EPR assistance and helpful discussions, Elizabeth Lockamy for advice and training on functional assays, and Octavian Cornea for assistance in preparing the manuscript.

3.8 Supplemental Information

Sample	pK_{Ca}
SERCA Only	6.48 ± 0.02
PLB	5.96 ± 0.01
pPLB	6.26 ± 0.02
36-TOAC-PLB	5.97 ± 0.01
36-TOAC-pPLB	6.27 ± 0.02

Table S1. pK_{Ca} values from functional experiments shown in Fig. 27.

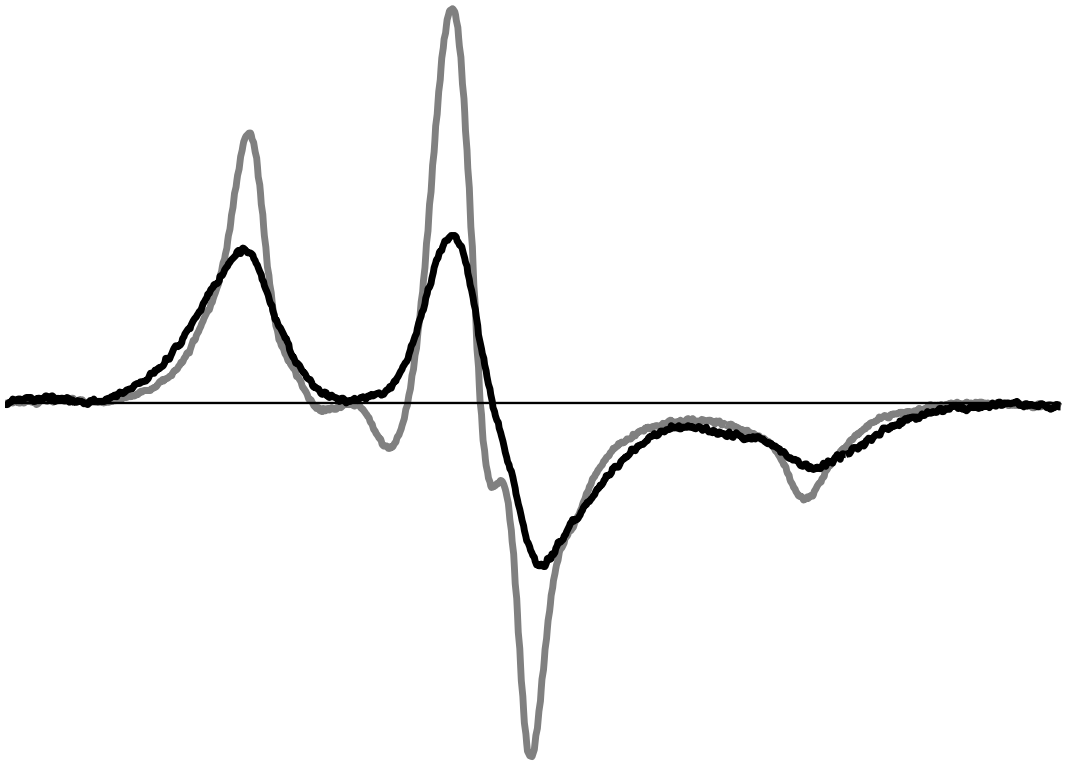

Fig. S32. Conventional EPR spectra of 36-TOAC PLB at 1000 L/P (gray, same conditions as in Fig. 28) and 20 L/P (black), showing greatly enhanced spin-spin interactions due to aggregation at 20 L/P.

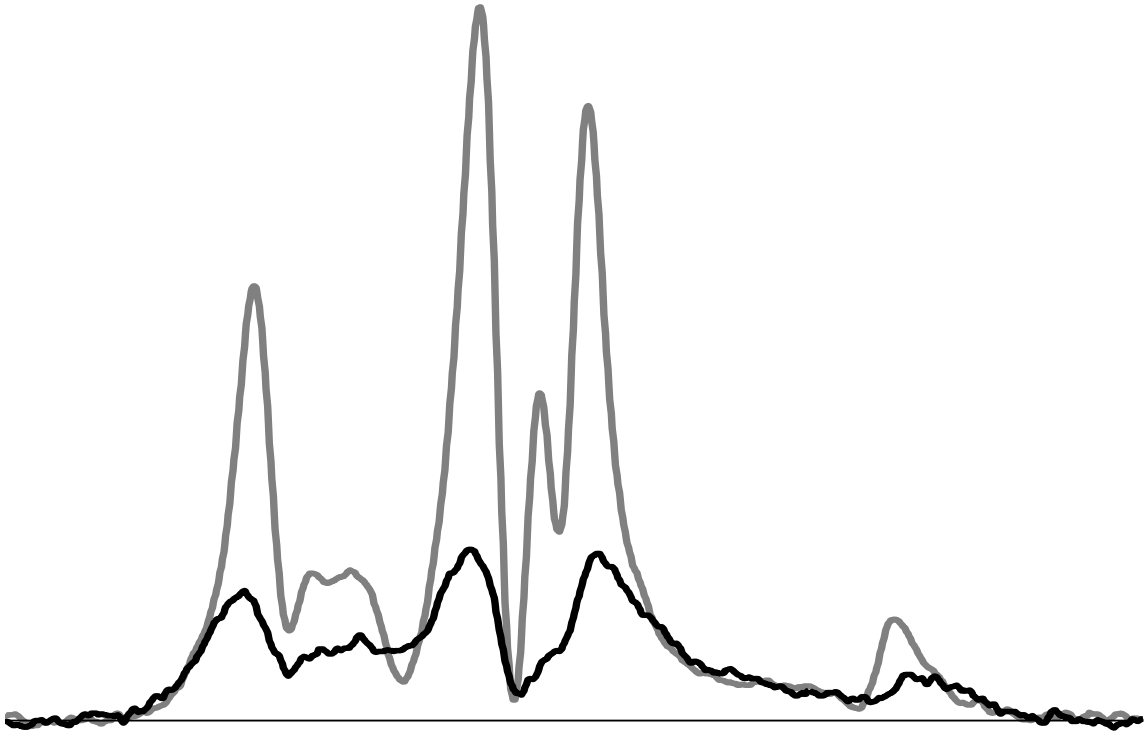

Fig. S33. STEPR spectra of 36-TOAC PLB at 1000 L/P (gray, same conditions as in Fig. 28) and 20 L/P (black). The black spectrum is strongly attenuated by spin-spin interactions [130], which are evident in the conventional EPR spectra of Fig. S32. Thus STEPR is quite sensitive to self-aggregation of this protein, which does not occur above 600 L/P.

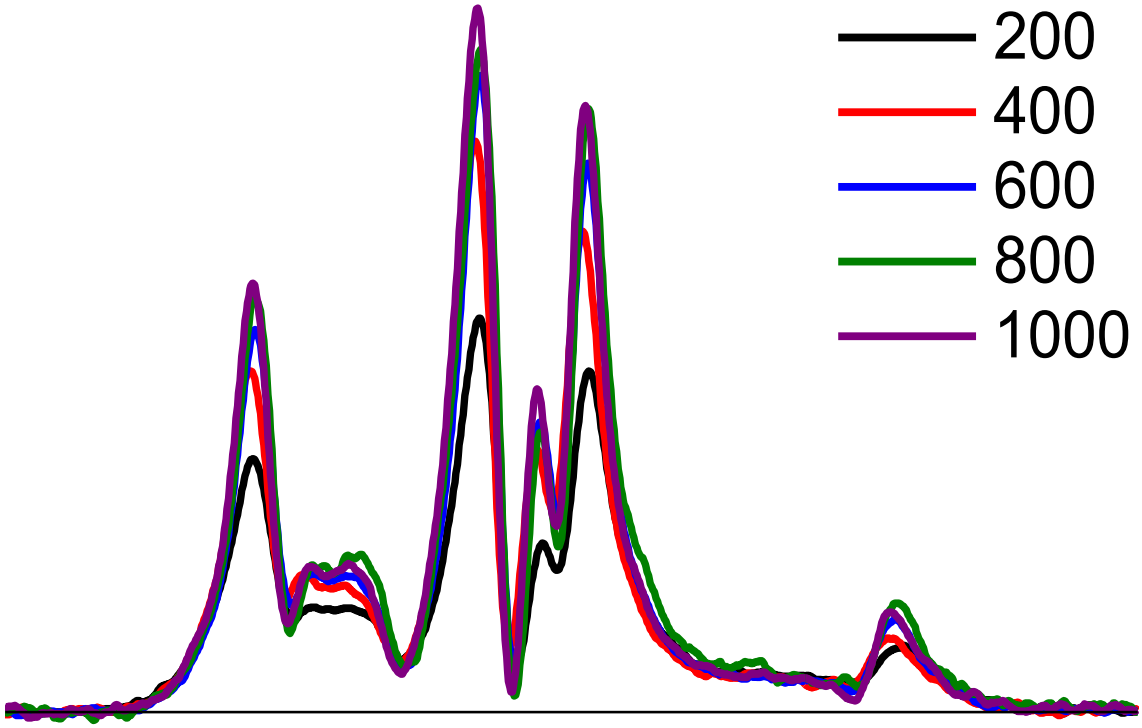

Fig. S34. STEPR spectra of 36-TOAC-PLB as a function of L/P (see figure legend), corresponding to the same samples as in Fig. 28. The increase in spectral intensity with increasing L/P (leveling off at high L/P) is consistent with decreasing spin-spin interactions [130], as documented in Fig. 28. STEPR lineshapes are essentially invariant above 600 L/P, supporting the conclusion that AFA-PLB is monomeric.

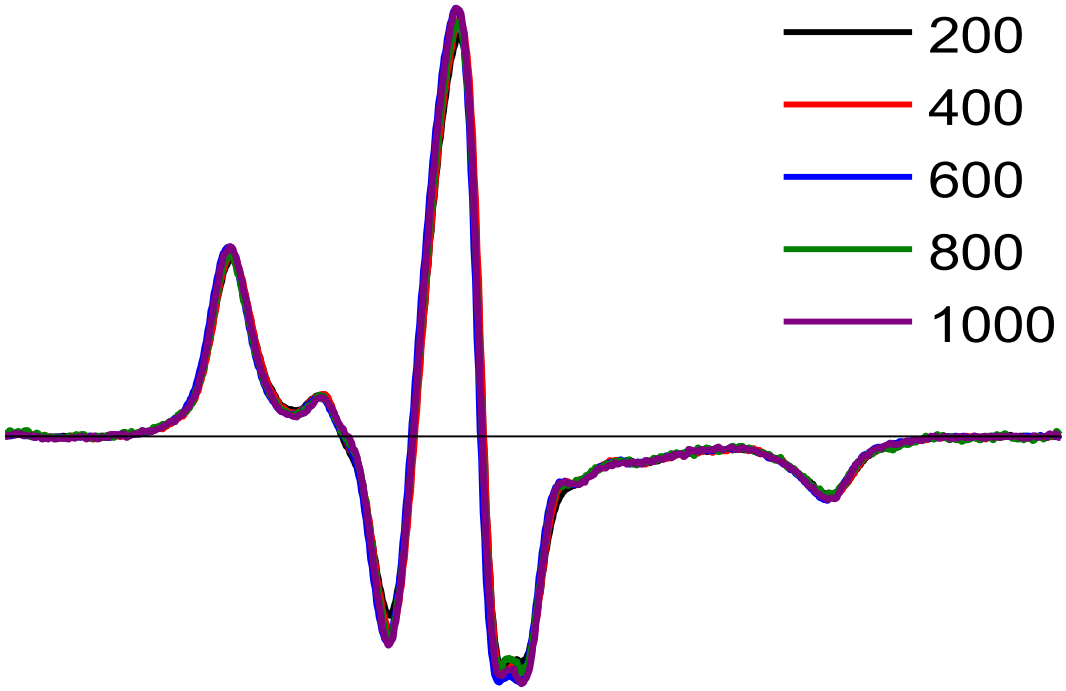

Fig. S35. Conventional EPR spectra of MSL-SERCA as a function of L/P, corresponding to the data shown in Fig. 29. The invariant spectra show that there are no significant changes in nanosecond rotational motion or spin-spin interactions due to variation of L/P, so all changes in STEPR spectra (Fig. 29) are due to μs rotational diffusion of SERCA. Average $2T_{\parallel}' = 68.2$ G.

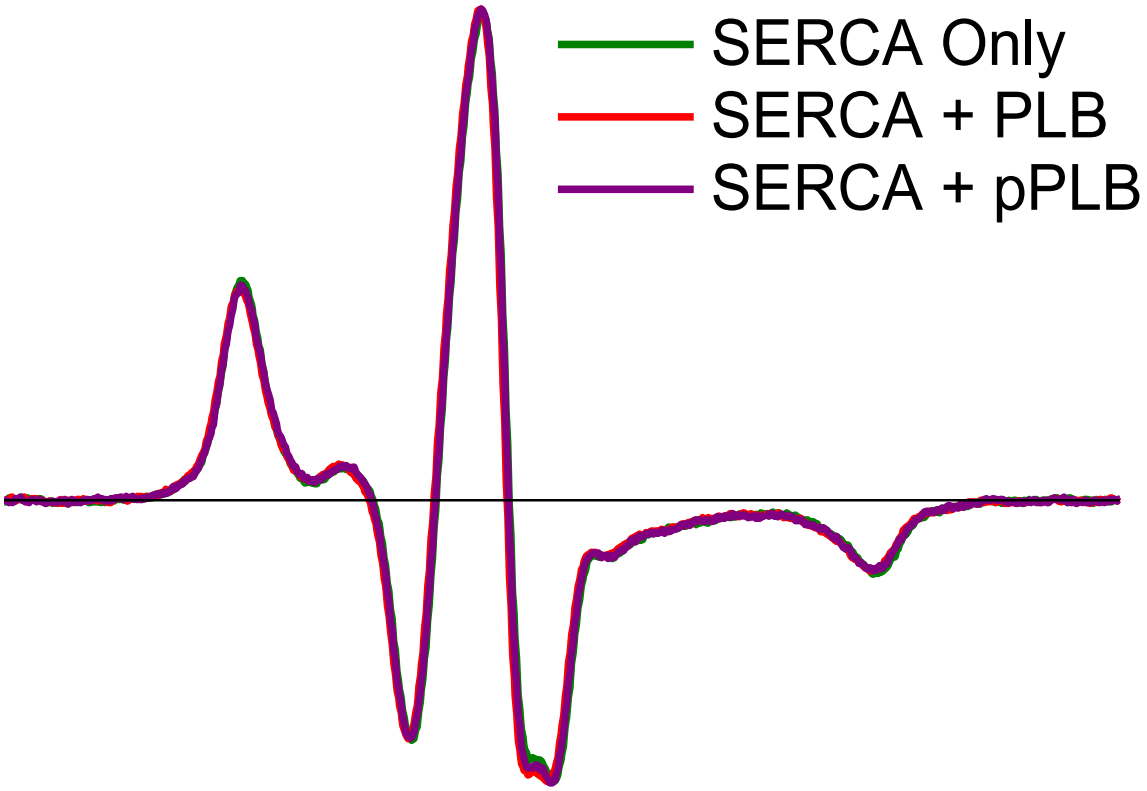

Fig. S36. Conventional EPR of MSL-SERCA reconstituted with unlabeled PLB, corresponding to the data shown in Fig. 31. The invariant spectra show that there are no significant changes in nanosecond rotational motion or spin-spin interactions due to PLB binding or phosphorylation, so STEPR spectra (Fig. 31) report microsecond rotational diffusion of SERCA.

Chapter 4: Optimization of Bicelle Lipid Composition and Temperature for EPR Spectroscopy of Aligned Membranes

Jesse E. McCaffrey, Zachary M. James, and David D. Thomas*

Department of Biochemistry, Molecular Biology, and Biophysics, University of Minnesota, Minneapolis, MN 55455

Submitted to: Journal of Magnetic Resonance

4.1 Summary

We have optimized the magnetic alignment of phospholipid bilayered micelles (bicelles) for EPR spectroscopy, by varying lipid composition and temperature. Bicelles have been extensively used in NMR spectroscopy for several decades, in order to obtain aligned samples in a near-native membrane environment and take advantage of the intrinsic sensitivity of magnetic resonance to molecular orientation. Recently, bicelles have also seen increasing use in EPR, which offers superior sensitivity and orientation resolution. However, the low magnetic field strength (less than 1 T) of most conventional EPR spectrometers results in homogeneously oriented bicelles only at a temperature well above physiological. To optimize bicelle composition for magnetic alignment at reduced temperature, we prepared bicelles containing varying ratios of saturated (DMPC) and unsaturated (POPC) phospholipids, using EPR spectra of a spin-labeled fatty acid to assess alignment as a function of lipid composition and temperature. Spectral analysis

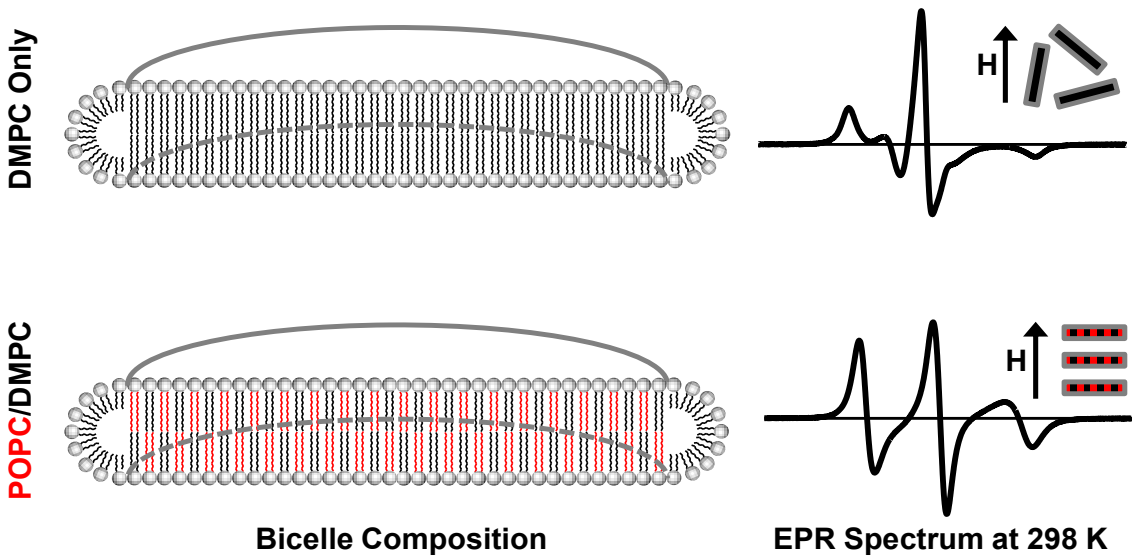

Fig. 37. Graphical Summary. Conventional DMPC-only bicelles (top, black) are poorly aligned at 298 K. Bicelles with a 1:1 molar mixture of POPC and DMPC (bottom, black and red) align homogeneously at 298 K.

showed that bicelles containing an equimolar mixture of DMPC and POPC homogeneously align at 298 K, 20 K lower than conventional DMPC-only bicelles. It is now possible to perform EPR studies of membrane protein structure and dynamics in bicelles at physiological temperatures and below.

4.2 Introduction

For several decades, bicelles have been used in magnetic resonance studies of membrane protein structure and dynamics [169]. A bicelle contains a flat patch of lipid bilayer comprised of long-chain lipids such as 1,2-dimyristoyl-sn-glycero-3-phosphocholine (14:0 PC or DMPC), surrounded by a rim of short-chain lipids such as 1,2-dihexanoyl-sn-glycero-3-phosphocholine (6:0 PC or DHexPC) protecting the hydrophobic core of the bilayer. Due to their negative magnetic susceptibility, bicelles placed in a sufficiently strong magnetic field will align with the membrane symmetry axis (membrane normal) perpendicular to the applied magnetic field [170]. This magnetic susceptibility can be altered by addition of paramagnetic lanthanides, which bind to lipid headgroups within bicelles, allowing for both parallel and perpendicular alignment [171]. In a well-prepared sample containing many bicelles, the alignment homogeneity is excellent, providing a more physiological alternative to other anisotropic membrane systems such as partially dehydrated lipid bilayers supported on glass plates [172] or lipid-containing crystals [173]. Since transmembrane proteins can be uniformly oriented in an aligned bicelle sample, techniques with sensitivity to orientation, such as nuclear magnetic resonance (NMR) and electron paramagnetic resonance (EPR), can be used to

measure probe orientation with high accuracy relative to the applied magnetic field [174-176], thus providing crucial information about protein structure and dynamics relative to the membrane.

Magnetically aligned bicelles have been most widely used in NMR, but bicelles applications in EPR using nitroxide spin labels have grown in recent years [177]. Due to the large magnetic moment of the electron spin, EPR offers much greater sensitivity than NMR, making possible much briefer experiments on much smaller samples, at more physiological lipid/protein ratios [61]. However, the substantially lower magnetic field strength (typically ~ 0.35 T of an X-band EPR spectrometer vs 16 T for 700 MHz NMR spectrometer) requires that bicelle composition must be modified to produce adequate alignment homogeneity. Protein orientation homogeneity in aligned bicelles is improved through addition of cholesterol, which acts to stabilize bicelle rigidity, as well as paramagnetic lanthanides [178, 179].

Homogeneous bicelle alignment is significantly influenced by lipid phase transitions, which are especially important in the case of the comparatively weak EPR magnetic field. At lower temperatures (~270 K), bicelles exist in an isotropic phase that is not readily aligned magnetically [180]. At higher temperatures (~290 K), bicelles transition into a nematic crystal phase, where they may be partially aligned, but are characterized by flexible lipid interactions that result in overall disorder [180]. At still higher temperatures (ca 320 K), bicelles transition into a smectic crystal phase, with rigid lipid interactions [181]. Bicelles in this smectic crystal phase can be identified by a substantial increase in sample viscosity and opacity, compared with the nematic and

isotropic phases [182]. The typical procedure for magnetic alignment of bicelles for EPR involves increasing temperature to drive the bicelle mixture from the isotropic phase to the smectic phase in the presence of a strong magnetic field (~ 1 T, the maximum field available on X-band EPR spectrometers). It has been shown that this alignment remains stable for hours after decreasing the field to 0.35 T for X-band EPR measurements [181]. The need for high temperatures to achieve the smectic phase presents a problem for studies of many proteins, as increased dynamics and thermal degradation complicate orientation measurements [183]. A possible solution is suggested by NMR studies in which the unsaturated phospholipid 1-palmitoyl-2-oleoyl-sn-glycero-3-phosphocholine (16:0-18:1 PC or POPC) has been shown to improve bicelle alignment at lower temperatures [172, 184].

4.3 Methods

In the present study, we optimize bicelle lipid composition with DMPC and POPC, in order to determine the minimum temperature for homogeneous alignment in X-band EPR experiments. Bicelles were prepared based on methods previously described [104]. Briefly, 5-DOXYL-stearic acid (5-DSA, Sigma Aldrich, St. Louis, MO) was combined with lipids (DMPC, POPC, DHexPC, Avanti Polar Lipids, Alabaster, AL), and cholesterol (Sigma Aldrich), all dissolved in chloroform. This produced bicelles with 700 long-chain lipids per 5-DSA [61], 13% cholesterol (mol cholesterol / mol long-chain lipid) [104, 178], and q (molar ratio of long- to short-chain lipids) = 4 [172]. Organic solvent was evaporated under N_2 gas and then completely removed by storage in a

vacuum desiccator overnight. 100 mM HEPES buffer (pH 7.0) was added up to 25% (lipid mass / buffer volume), then the sample was vortexed for 2 min and placed on ice for 5 min. After repeating this process twice, samples were sonicated in an ice bath for 30 min [104]. Prepared lanthanide stock ($TmCl_3$*$6H_20$ (Sigma Aldrich, St. Louis, MO) in 100 mM HEPES) was added to the sample up to 20% (mol lanthanide / mol long-chain lipid), then vortexed for 2 min [104]. Samples were then flash-frozen in liquid N_2 three times to further homogenize, yielding a clear, viscous fluid. 16 μL of the sample was pipetted into a 0.6/0.84 mm ID/OD glass capillary (Vitrocom, Mountain Lakes, NJ), in order to span the active portion of the EPR resonator. The capillary was then plugged with Critoseal (Krackeler Scientific, Albany, NY). Randomly oriented samples (vesicles) were prepared identically to bicelles, with the omission of the short-chain lipid DHexPC.

EPR experiments were performed on a Bruker EleXsys E500 spectrometer equipped with an ER 4122 SHQ spherical resonator. Sample temperature was maintained at ± 0.2 K using a quartz dewar attached to a nitrogen gas temperature controller. Samples were first placed in the resonator and equilibrated at 273 K for 5 min. To align bicelles, the field strength was raised to 1.1 T [181], then the temperature was raised 2 K per minute up to the final (alignment) temperature, at which point the sample was incubated for 20 min at 1.1 T field strength. The EPR spectrum was then acquired at X-band field strength (~3400 G) at the desired alignment temperature. For randomly oriented vesicle samples, spectra were acquired immediately after the initial 5 minute equilibration at the desired temperature. Spectra were acquired with the following

parameters: 2 mW microwave power, 1 G peak-to-peak modulation amplitude, 120 G sweep width, and 20.48 ms time constant and conversion time.

EPR spectra were background-corrected and normalized to the double integral [185]. Least-squares minimization fitting was performed in MultiComponent, an EPR simulation program that is optimized for fitting spectra to models involving multiple populations (Altenbach et al) [186]. Data was fit based on a model of microscopic order, macroscopic disorder (MOMD). Starting values for the DOXYL *g*-factor and hyperfine tensors were obtained from a previous study [187], and further refined with the spectrum of a 5-DSA vesicle sample acquired at 200 K (see Supplemental Information for fitting details). The model for vesicle samples assumed a single, randomly oriented component with isotropic rotational diffusion and Lorentzian linewidth tensors, as well as an orienting potential determined by c_{20}. Oriented bicelle spectra were fit to a two-component model: randomly oriented and aligned. The randomly oriented component was assumed to be the same as that of the corresponding vesicle sample. For the aligned component, all parameters were fixed to those of the random component, with the exceptions that NORT (the number of orientations calculated) was reduced from 20 to 1, and the orienting potential coefficients c_{20}, c_{22}, and c_{40} were allowed to vary. Rigorous fitting revealed that constraining the dynamics (τ_R) and magnetic parameters (*g*, A) for the aligned component to those from the randomly oriented component requires additional orienting coefficients, presumably to account for subtle orientation disorder in the aligned component. Alignment homogeneity was characterized by the mole fraction of the aligned component relative to the randomly oriented component ("fraction

aligned" below). Aligned bicelle spectra were also fit to a single aligned component, allowing disorder in the orienting potential, but these fits gave much higher χ^2 values than the two-component model described above. Standard error of the mean (SEM) for fit parameters was determined by least-squares minimization fitting in NLSL (Freed et al) [113, 188]. All spectra are centered at 3356 G with a baseline of 120 G, and are all to scale.

4.4 Results

We began by verifying the bicelle alignment methodology of Ghimire and co-workers [104], preparing conventional DMPC bicelles containing 5-DSA, and using thulium to align bicelles parallel to the magnetic field up to 318 K and 298 K. Fig. 38 shows the EPR spectra of 5-DSA in randomly oriented vesicles (top) and parallel aligned

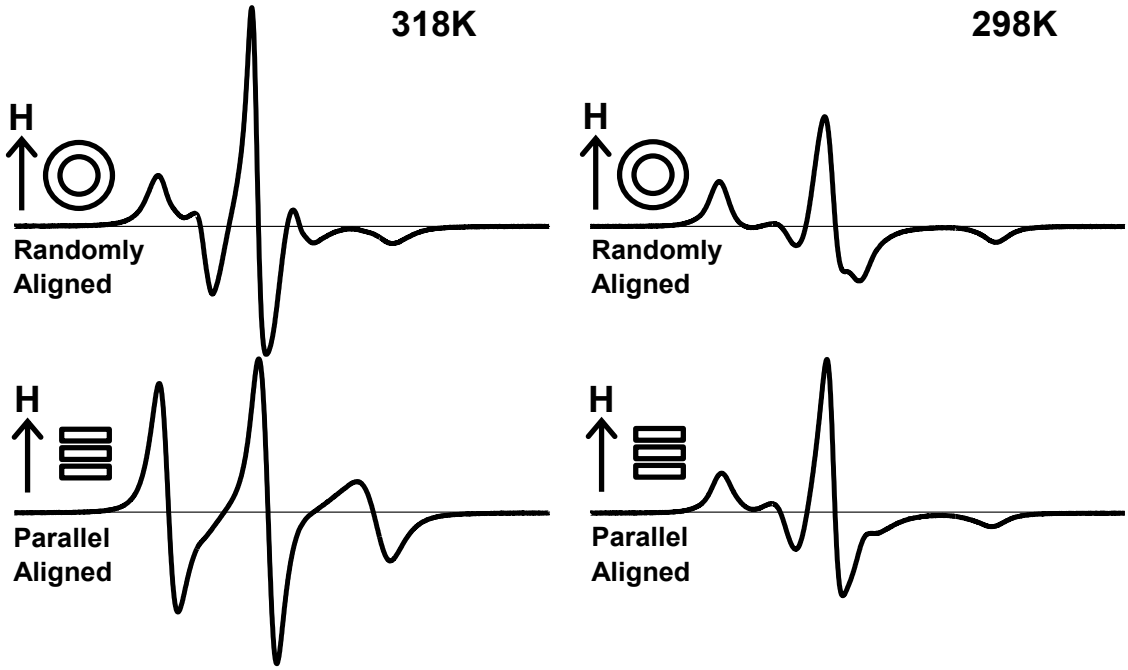

Fig. 38. EPR spectra of 5-DSA in conventional DMPC vesicles (top) and bicelles with membrane normal oriented parallel to the instrument magnetic field (bottom) aligned at 318 K (left) and 298 K (right).

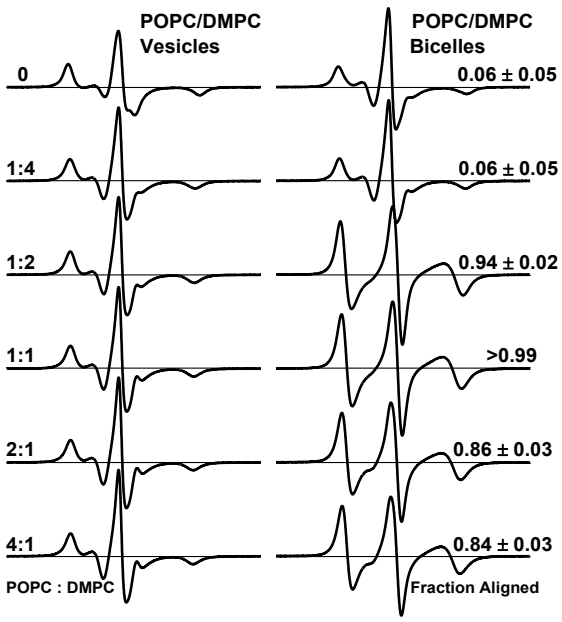

Fig. 39. EPR spectra of 5-DSA in POPC/DMPC vesicles (left) and bicelles (right) as a function of POPC:DMPC molar ratio (left text). All spectra were acquired at 298 K. The relative amount of 5-DSA in uniformly oriented bicelles is indicated as fraction aligned (right text).

bicelles (bottom). There is a substantial change in lineshape upon alignment of bicelles at 318 K, reflecting a uniform orientation distribution of the 5-DSA spin label. These spectra are consistent with previous studies of 5-DSA in conventional DMPC bicelles [189]. When this experiment was repeated using an alignment temperature of 298 K (Fig. 38, right), there was no significant spectral change between the vesicle and bicelle samples, suggesting that conventional DMPC bicelles cannot be uniformly aligned at 298 K.

Next, we optimized the POPC:DMPC molar ratio for bicelles by performing a titration experiment with different POPC:DMPC ratios. During this experiment, we aligned bicelle samples up to 298 K, consistent with previous NMR experiments using bicelles of similar composition [172, 184, 190]. Fig. 39 shows the EPR spectra of 5-DSA in vesicles and aligned bicelles at 298 K as a function of POPC:DMPC molar ratio. Both the control (0 POPC:DMPC) and 1:4 POPC:DMPC bicelle samples were poorly aligned.

These samples possess similar vesicle and aligned bicelle spectra, as well as low alignment fractions. Upon increasing the POPC:DMPC molar ratio to 1:2, there was a substantial change in the aligned bicelle EPR lineshape, indicative of improved alignment homogeneity. The aligned component now accounts for a majority of the spectrum (fraction aligned = 0.94), although there is some residual randomly oriented component. At 1:1 POPC:DMPC, the aligned bicelle EPR sample was homogeneously aligned, with a fraction aligned greater than 0.99. This spectrum is well-fit with only the aligned component. For higher POPC:DMPC molar ratios, the fraction aligned is slightly degraded, possibly due to a perturbation in bilayer structure from high POPC concentration. The data in Fig. 39 therefore suggests that a 1:1 molar ratio of POPC:DMPC is the optimum value for aligned bicelle EPR. This is consistent with NMR experiments that have used 1:1 POPC:DMPC and observe homogeneous alignment at ambient temperature [184].

Next, we characterized the alignment homogeneity of conventional DMPC bicelles as a function of alignment temperature. Fig. 40 shows the EPR spectra of 5-DSA in vesicles and aligned conventional DMPC bicelles, using alignment temperatures between 278 K and 318 K. Aside from small changes in splitting and linewidth due to temperature, the aligned bicelle spectra from 278 K to 298 K are nearly identical. The bicelle samples corresponding to these three spectra were poorly aligned, with alignment fractions below 0.1. At 308 K, the aligned bicelle spectrum changes slightly, particularly in the region immediately flanking the central resonance, and the fraction aligned increases to 0.29. In contrast, the 318 K spectrum possesses a strikingly different

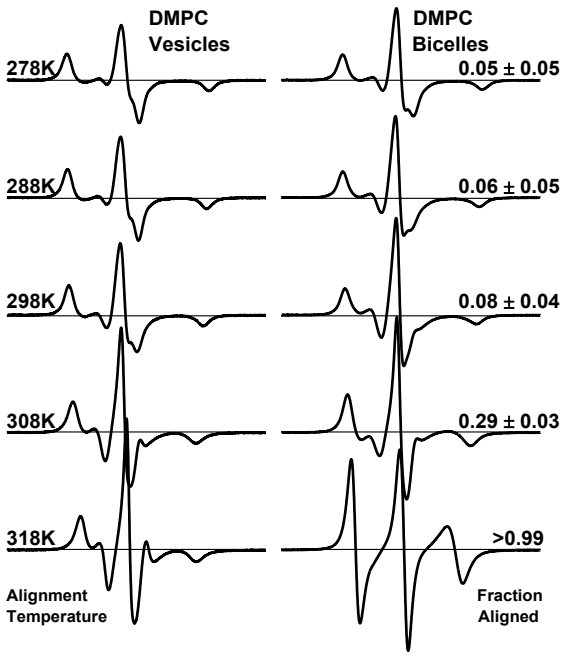

Fig. 40. EPR spectra for 5-DSA in DMPC-only vesicles (left) and bicelles (right) as a function of alignment temperature (left text). The relative amount of 5-DSA in uniformly oriented bicelles is indicated as fraction aligned (right text).

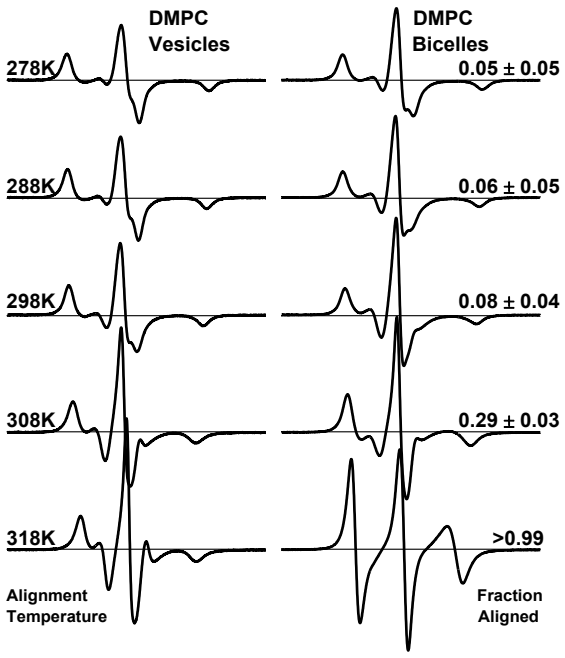

Fig. 41. EPR spectra for 5-DSA in 1:1 POPC:DMPC vesicles (left) and bicelles (right) as a function of alignment temperature (left text). The relative amount of 5-DSA in uniformly oriented bicelles is indicated as fraction aligned (right text).

lineshape, and is well-fit by only the aligned component. Therefore, a temperature of 318 K is required for homogeneous alignment of conventional DMPC bicelles. This result is consistent with previous EPR experiments using this conventional bicelle method that observe complete alignment at 318 K [178, 179, 181].

Fig. 41 shows the EPR spectra of 5-DSA in vesicles and aligned bicelles with 1:1 POPC:DMPC, using alignment temperatures between 278 K and 318 K. Although the 278 K spectra indicate poor alignment, substantial alignment is observed beginning at 288 K (fraction aligned = 0.80). At 298 K, the fraction aligned is greater that 0.99, indicative of homogeneous alignment. At 308 K and 318 K, the fraction aligned decreases slightly. This suggests that high temperature destabilizes POPC/DMPC bicelle alignment, possibly either through thermal motion or transition to another isotropic

bicelle phase. Importantly, the alignment homogeneity of these POPC/DMPC bicelles at 298 K is comparable to that of conventional DMPC-only bicelles at 318 K, as both spectra are well-fit by a single oriented spectral component (fraction aligned ~ 1).

4.5 Conclusions

In summary, through optimization of lipid composition and alignment temperature, we found that bicelles containing a 1:1 mixture of POPC and DMPC homogeneously align at 298 K, which is 20 K less than the alignment temperature required for conventional DMPC-only bicelles. This decrease in alignment temperature is likely due to POPC reducing bicelle phase transition temperatures (T_M), since T_M for pure POPC is 26 K lower than that for pure DMPC. The vesicle EPR spectra for both DMPC-only and POPC/DMPC samples report similar dynamics and magnetic parameters (see Supplemental Information), suggesting that the lipid environments are also similar. The POPC/DMPC bicelles described in this work should be excellent reconstitution systems for orientation studies of proteins with structural dynamics that are sensitive to temperature, such as the regulatory proteins sarcolipin and phospholamban, as well as the SR Ca-ATPase SERCA.

4.6 Acknowledgements

This work was supported in part by NIH grants GM27906 and AR057220 to DDT. JEM was supported by NIH Training Grant AR007612, and ZMJ was supported by NIH Training Grants AR007612 and GM008700. EPR experiments were performed at

the Biophysical Spectroscopy Center. Computational resources were provided by the Minnesota Supercomputing Institute. We thank Edmund Howard and Yuri Nesmelov for EPR simulation assistance and helpful discussions, and Octavian Cornea for assistance in preparing the manuscript.

4.7 Supplemental Information

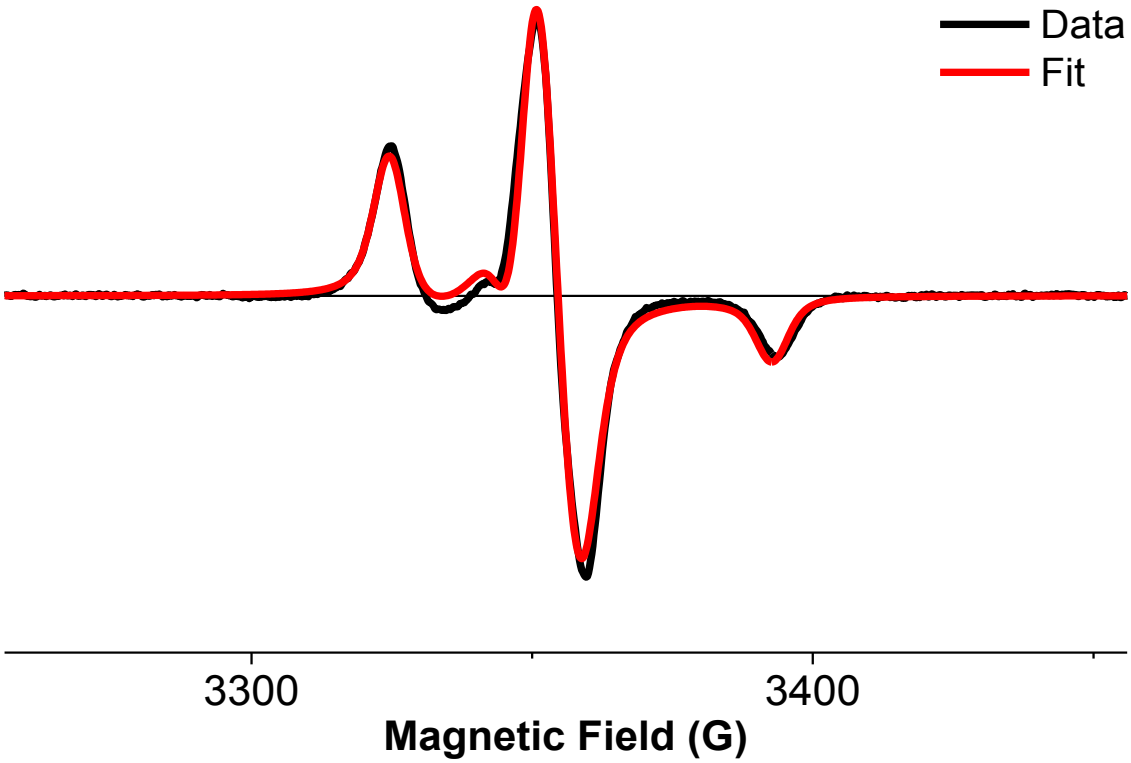

Fig. S42. EPR spectrum and best fit for 5-DSA in randomly oriented conventional DMPC bicelles frozen at 200K. Acquired EPR spectrum is shown in black, and best fit is shown in red.

Lipid Structure	POPC:DMPC (mol/mol)	Temp (K)	g_x	g_y	g_z	$A_{\parallel}$ (G)	$A_{\perp}$ (G)
Vesicle	0	200	2.0083	2.0059	2.0030	34.07	5.54

Table S2. Fitting parameters for 5-DSA bicelle sample from Fig. 38.

Lipid Structure	POPC:DMPC (mol/mol)	Temp (K)	g_x	g_y	g_z	$A_{\parallel}$ (G)	$A_{\perp}$ (G)	τ_R (ns)	C_{20} (kT)	C_{22} (kT)	C_{40} (kT)
Vesicle	0	298	2.0083	2.0059	2.0030	31.71	6.22	7.72	3.57	0	0
Bicelle	0	298	2.0083	2.0059	2.0030	31.71	6.22	7.72	7.20	-8.78	-0.24
Vesicle	1:4	298	2.0083	2.0059	2.0030	31.71	6.26	9.23	3.57	0	0
Bicelle	1:4	298	2.0083	2.0059	2.0030	31.71	6.26	9.23	5.77	-5.76	0.98
Vesicle	1:2	298	2.0083	2.0059	2.0030	31.76	6.24	8.95	3.43	0	0
Bicelle	1:2	298	2.0083	2.0059	2.0030	31.76	6.24	8.95	1.72	-0.86	-0.35
Vesicle	1:1	298	2.0083	2.0059	2.0030	31.58	6.26	10.46	3.77	0	0
Bicelle	1:1	298	2.0083	2.0059	2.0030	31.58	6.26	10.46	1.65	-0.37	-0.58
Vesicle	2:1	298	2.0083	2.0059	2.0030	31.40	6.33	12.43	4.22	0	0
Bicelle	2:1	298	2.0083	2.0059	2.0030	31.40	6.33	12.43	1.60	0.18	-0.74
Vesicle	4:1	298	2.0083	2.0059	2.0030	31.54	6.24	12.24	4.17	0	0
Bicelle	4:1	298	2.0083	2.0059	2.0030	31.54	6.24	12.24	1.67	0.23	-0.91

Table S3. Fitting parameters for 5-DSA in POPC/DMPC vesicles and bicelles as a function of POPC:DMPC molar ratio (see Fig. 39).

Lipid Structure	POPC:DMPC (mol/mol)	Temp (K)	g_x	g_y	g_z	$A_{\parallel}$ (G)	$A_{\perp}$ (G)	τ_R (ns)	C_{20} (kT)	C_{22} (kT)	C_{40} (kT)
Vesicle	0	278	2.0083	2.0059	2.0030	32.89	5.89	371.47	18.69	0	0
Bicelle	0	278	2.0083	2.0059	2.0030	32.89	5.89	371.47	9.41	-1.23	8.63
Vesicle	0	288	2.0083	2.0059	2.0030	32.48	5.70	188.29	16.12	0	0
Bicelle	0	288	2.0083	2.0059	2.0030	32.48	5.70	188.29	9.92	5.16	-2.86
Vesicle	0	298	2.0083	2.0059	2.0030	31.61	6.05	57.04	12.12	0	0
Bicelle	0	298	2.0083	2.0059	2.0030	31.61	6.05	57.04	4.22	-4.53	-0.24
Vesicle	0	308	2.0083	2.0059	2.0030	31.02	6.71	11.39	4.05	0	0
Bicelle	0	308	2.0083	2.0059	2.0030	31.02	6.71	11.39	3.61	4.21	-0.84
Vesicle	0	318	2.0083	2.0059	2.0030	30.72	7.05	7.62	2.94	0	0
Bicelle	0	318	2.0083	2.0059	2.0030	30.72	7.05	7.62	1.80	-0.54	-0.91

Table S4. Fitting parameters for 5-DSA in DMPC-only vesicles and bicelles as a function of alignment temperature (see Fig. 40).

Lipid Structure	POPC:DMPC (mol/mol)	Temp (K)	g_x	g_y	g_z	$A_{\parallel}$ (G)	$A_{\perp}$ (G)	τ_R (ns)	C_{20} (kT)	C_{22} (kT)	C_{40} (kT)
Vesicle	1:1	278	2.0083	2.0059	2.0030	32.25	5.76	92.71	14.75	0	0
Bicelle	1:1	278	2.0083	2.0059	2.0030	32.25	5.76	92.71	9.86	3.79	-4.14
Vesicle	1:1	288	2.0083	2.0059	2.0030	31.66	6.28	25.26	8.43	0	0
Bicelle	1:1	288	2.0083	2.0059	2.0030	31.66	6.28	25.26	5.87	5.60	-1.10
Vesicle	1:1	298	2.0083	2.0059	2.0030	31.54	6.35	11.44	3.95	0	0
Bicelle	1:1	298	2.0083	2.0059	2.0030	31.54	6.35	11.44	1.62	-0.17	-0.65
Vesicle	1:1	308	2.0083	2.0059	2.0030	31.58	6.54	7.28	2.81	0	0
Bicelle	1:1	308	2.0083	2.0059	2.0030	31.58	6.54	7.28	1.61	-0.21	-0.86
Vesicle	1:1	318	2.0083	2.0059	2.0030	31.40	6.76	5.79	2.25	0	0
Bicelle	1:1	318	2.0083	2.0059	2.0030	31.40	6.76	5.79	1.63	-0.39	-0.94

Table S5. Fitting parameters for 5-DSA in 1:1 POPC:DMPC vesicles and bicelles as a function of alignment temperature (see Fig. 41).

Fig. S43. EPR spectra and best fit for 5-DSA in POPC/DMPC vesicles (left) and bicelles (right) as a function of POPC:DMPC molar ratio aligned and acquired at 298K (see Fig. 39 of the manuscript). Acquired EPR spectra are shown in black, and best fits are shown in red.

Fig. S44. EPR spectra and best fit for 5-DSA in DMPC-only vesicles (left) and bicelles (right) as a function of alignment temperature (see Fig. 40 of the manuscript). Acquired EPR spectra are shown in black, and best fits are shown in red.

Fig. S45. EPR spectra and best fit for 5-DSA in 1:1 POPC:DMPC vesicles (left) and bicelles (right) as a function of alignment temperature (see Fig. 41 of the manuscript). Acquired EPR spectra are shown in black, and best fits are shown in red.

Chapter 5: A Bifunctional Spin Label Reports the Structural Topology of Phospholamban in Magnetically-Aligned Bicelles

Zachary M. James, Jesse E. McCaffrey, Bengt Svensson, Ben P. Binder, and David D. Thomas

Department of Biochemistry, Molecular Biology, and Biophysics, University of Minnesota, Minneapolis, MN 55455

To be submitted to: Journal of the American Chemical Society

5.1 Summary

We have applied a bifunctional spin label and EPR spectroscopy to the study of membrane protein structural topology in magnetically-aligned bicelles, using monomeric phospholamban (PLB) as a model system. Bicelles are a powerful tool for studying membrane proteins by NMR and EPR spectroscopies, where magnetic alignment yields topological constraints by resolving the anisotropic spectral properties of nuclei and spin labels. However, EPR bicelle studies are often hindered by the rotational mobility of conventional Cys-linked spin labels, which obscures their orientation relative to the host protein. The rigid TOAC label provides high orientation sensitivity but must be introduced via solid-phase peptide synthesis, precluding its use in large proteins. Here we show that a bifunctional methanethiosulfonate spin label, attached to i and i + 4 Cys residues along PLB's transmembrane helix, offers orientation resolution similar to TOAC, while being applicable to large proteins for which synthesis is impractical.

5.2 Introduction

Magnetically-aligned bicelles are a powerful tool for studying the structural topology of integral membrane proteins by magnetic resonance spectroscopies. Reconstitution into aligned bicelles can resolve the anisotropic spectral properties of nuclei for NMR or nitroxide spin labels for EPR, yielding valuable information regarding protein orientation with respect to the bilayer. Bicelles (bilayered micelles) are mixtures of long- and short-chain phospholipids that combine to form patches of long-chain lipid bilayers encircled by short-chain lipids. Bicelles possess negative magnetic susceptibility

($\Delta\chi$), and in the presence of high magnetic fields ($\mathbf{B_0} \geq 6$ T) will align spontaneously with their membrane normal (n) perpendicular to the field ($n \perp \mathbf{B_0}$). Alignment may be enhanced by the addition of lanthanides that associate with bicelle surface and further decrease $\Delta\chi$ (Dy^{3+}), or impart a positive $\Delta\chi$ (Tm^{3+}) that 'flips' the bicelles such that they align with n parallel to the field ($n \parallel \mathbf{B_0}$).

In solid-state NMR spectroscopy, particularly the $^{1}H/^{15}N$ PISEMA and SAMMY experiments, membrane protein alignment in bicelles (or mechanically-oriented bilayers) resolves the $^{15}N - ^{1}H$ dipolar coupling and ^{15}N chemical shift anisotropies to permit the

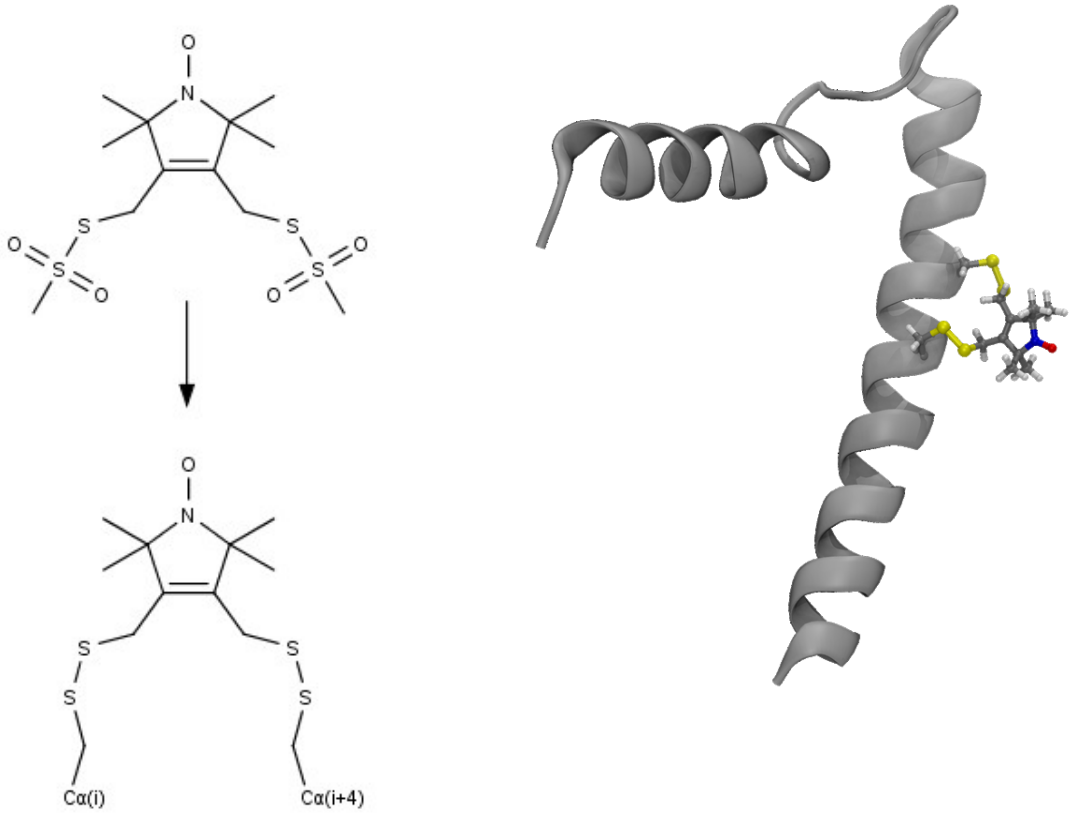

Fig. 46. Left: structural formula of BSL. Right: energy-minimized structure of BSL attached at positions 32 and 36 on the structure of monomeric PLB. BSL dihedral angles were determined from a study by Fleissner and co-workers [93].

determination of transmembrane helical tilt and azimuthal rotation [191]. Similarly, sample alignment in conventional EPR can resolve the *g*-factor and hyperfine coupling anisotropies of nitroxides introduced via site-directed spin labeling [192], provided these parameters do not undergo significant motional averaging. However, conventional Cys-linked spin labels often possess residual ps – ns rotational mobility that limits their utility in oriented EPR measurements. To overcome this obstacle, the Lorigan Lab has pioneered the use of TOAC in bicelle EPR, which suppresses backbone-independent probe motion by incorporating the nitroxide group and α-carbon into the same six-membered ring [193]. While the rigidity of TOAC affords high orientation resolution, it must be introduced during solid-phase peptide synthesis, precluding its use in large proteins. Techniques to introduce TOAC via amber codon suppression have thus far proved unsuccessful [194], so bicelle EPR measurements to date have focused exclusively on small (< 60 residues) proteins amenable to peptide synthesis [104, 176].

The bifunctional spin label HO-1944 (Fig. 46, hereafter called BSL) is a derivative of the popular methanethiosulfonate spin label (MTSL), and reacts with CxxC or CxxxC motifs along α-helices, or CxC motifs along β-sheets. Bifunctional attachment significantly restricts probe mobility and orientation with respect to the peptide backbone, permitting a variety of EPR measurements that are impractical with monofunctionally-attached labels. Studies using BSL have probed the μs – ms rotational dynamics of actin-bound myosin S1 [195, 196] and tropomyosin [90], as well as the orientation of myosin S1 in mechanically-oriented muscle fibers [197]. Recently, BSL was shown to enhance the resolution of double electron-electron resonance (DEER) distance measurements for

both aqueous [93] and membrane [198, 199] proteins, presumably by constraining the static disorder of the label. In the present study, we demonstrate that BSL can be used in conjunction with magnetically-aligned bicelles to probe the structural topology of membrane proteins, with orientation resolution comparable to TOAC. For our model system we chose phospholamban (PLB), a single-pass membrane protein that regulates the cardiac sarcoplasmic reticulum Ca^{2+}-ATPase (SERCA) [200]. Wild-type PLB equilibrates between monomeric and homopentameric states, so the purely monomeric mutant C36A/C41F/C46A (AFA) was employed to simplify the system and eliminate potential spin-spin interactions [201]. The structural topology of AFA-PLB in mechanically-oriented bilayers has been thoroughly characterized by hybrid solution/solid-state NMR techniques, allowing for the interpretation of our results in the context of a high-resolution structure [201].

5.3 Methods

Double-Cys (F32C/A36C) and single-Cys (F32C) PLB constructs were prepared by QuikChange mutagenesis of a plasmid encoding the Cys-free monomeric mutant C36A/C41F/C46A (AFA) PLB as a cleavable fusion to maltose binding protein (MBP) [202]. Expression was carried out in BL21(DE3) cells (Lucigen) grown in Terrific Broth at 37 °C and induced with 0.5 mM IPTG once OD_{600} reached 2.5 – 3.0. Following induction, cells were incubated 20 hr at room-temperature before collection by centrifugation, after which expressed MBP-PLB was purified by amylose resin

chromatography, cleaved with recombinant TEV protease [203], and purified by HPLC [204, 205].

Purified, lyophilized PLB was solubilized at 100 μM in 50 mM Tris-HCl, 5% (w/v) SDS, pH 7.5 and immediately combined with 5-fold molar excess BSL (Toronto Research Chemicals) from a 25 mM stock in N,N-dimethylformamide, followed by 16 hr incubation at room-temperature with protection from light. The next day, spin-labeled protein was re-purified by HPLC and lyophilized as above, then solubilized at ~1 mg/mL in trifluoroethanol and stored at -20 °C. Labeling efficiency (> 95%) was determined by dissolving a portion of each lyophilized powder in 5% (w/v) SDS and comparing the double-integrals of their EPR spectra to that of a 100 μM TEMPOL standard, followed by determination of protein concentration using a BCA (Thermo Fisher Scientific, Rockford IL). Labeling specificity was determined using electrospray ionization mass spectrometry (ESI-MS). Briefly, lyophilized powders were solubilized in 50:50 H_2O/acetonitrile (v/v) containing 0.1% (v/v) mass-spectrometry-grade formic acid (Sigma). Samples were characterized by direct infusion onto an Agilent MSD SL Ion Trap operating in positive ion mode.

Spin-labeled PLB was reconstituted at 1400 long-chain lipids per PLB into 2:2:1 (mol/mol) DMPC/POPC/DHexPC bicelles containing 13% (mol/mol) cholesterol and 20% (mol/mol) $TmCl_3$ or $DyCl_3$ [184, 193]. To prepare bicelles, lipid and cholesterol stocks in chloroform (Avanti Lipids) were combined with PLB, dried under N_2 gas, and stored overnight in a vacuum desiccator. The resulting films were resuspended at 25% (w/v) in 100 mM HEPES, pH 7.0 by thorough vortexing and ice-water-bath sonication,

after which the samples were combined with lanthanides also dissolved in 100 mM HEPES. To create lipid vesicles, samples were prepared as described above while omitting DHexPC.

EPR experiments were performed on a Bruker EleXsys E500 spectrometer equipped with an ER 4122 SHQ resonator containing a quartz dewar insert attached to a nitrogen gas temperature controller. 16 µL samples were loaded into 0.6 mm inner diameter glass capillaries (Vitrocom) and plugged with Critoseal (Krackeler Scientific, Albany, NY). For alignment, bicelle samples were first incubated in the resonator for 5 min at 273 K in the absence of a magnetic field. Next, the field strength was raised to 1.1 T and the temperature gradually increased to 298 K at a rate of 2 K per minute. Finally, the samples were incubated for 20 min at 298 K and 1.1 T before the field strength was decreased for EPR measurements. For vesicle samples, spectra were acquired directly at 298 K or 200 K. Spectra at 298 K were acquired using 1 G peak-to-peak amplitude modulation, 5 mW microwave power, and a 120 G sweep width, while spectra at 200 K were acquired with 0.1 mW microwave power and a 200 G sweep width.

EPR spectra were background-corrected and normalized in WACY, an in-house program developed by Edmund Howard [185]. WACY was also used to fit the rigid-limit spectra acquired at 200 K. All other spectra were fit using NLSL [113] and the LabView program MultiComponent developed by Christian Altenbach. Randomly-oriented spectra were fit assuming the microscopic-order macroscopic-disorder (MOMD) model. Initial values for the hyperfine and *g* tensors were taken from the fits to the frozen (200 K) EPR spectrum of the lipid vesicle sample. Aligned bicelle spectra were fit globally, again using

an isotropic rotational diffusion tensor and the first coefficient of the orienting potential (c_{20}). To optimize the fit, values for the axially symmetric hyperfine tensor were allowed to vary. During global fitting, the director tilt angles were fixed at 0° (parallel) and 90° (perpendicular) while the diffusion tilt angles β_D and γ_D were allowed to vary.

5.4 Results

Prior to our EPR measurements, we performed electrospray ionization (ESI) mass spectrometry on both BSL-F32C/A36C-PLB (hereafter called 32/36-BSL-PLB) and BSL-F32C-PLB (hereafter called 32-BSL-PLB) to characterize the nature of labeling. Our results indicate that the 32/36-PLB construct containing a single, bifunctionally-attached label is the predominant species (Fig. S50a). This is further supported by the absence of dipolar broadening in our EPR spectra, which would be observed if two labels were each monofunctionally attached to 32/36-BSL-PLB. In comparison, ESI-MS of 32-BSL-PLB revealed the predominant species to be monofunctionally-attached BSL with an intact, second methanethiosulfonate group (Fig. S50b). Our results are in good agreement with those reported previously [93], where monofunctional and bifunctional attachment yield similar degrees of BSL immobilization. Notably, the sharp spectral features of the 32/36-BSL-PLB spectrum indicate that bifunctional attachment predominates in the F32C/A36C sample.

To determine the rotational dynamics of BSL-F32C/A36C-PLB in the absence of alignment, but still mimicking the bicelle environment, we acquired its spectrum at 298 K following reconstitution into DMPC/POPC vesicles containing 13% (mol/mol)

cholesterol and 20% (mol/mol) $TmCl_3$. Fig. 47a shows the vesicle spectrum at 298 K, revealing a lineshape typical for strongly immobilized, membrane-embedded nitroxides ($2A_{\parallel}' = 62.2$ G) [106]. In comparison, the EPR spectrum of our labeled single-Cys construct in lipid vesicles reports a similar outer splitting ($2A_{\parallel}' = 61.7$ G, Fig. S51) but a significantly broader linewidth, indicating that the unreacted methanethiosulfonate group restricts BSL rotational mobility. This effect has been observed for other mutants, and matches the effects of 4-substituted MTSL derivatives [206].

A spectrum of the BSL-32/36-PLB acquired at 200 K (Fig. 47b) reports an outer splitting of 66.0 G, indicating that residual ns mobility is present, arising either from BSL internal dynamics or the motion of PLB itself. To quantify rotational dynamics, we first fit the 200 K spectrum assuming a rigid-limit model, in order to determine values for the *g*-factor and hyperfine tensors (Table 6). These served as initial values when analyzing the 298 K spectrum, which was fit assuming the MOMD model [113]. A satisfactory fit was obtained using an isotropic rotational correlation time (τ_R) and the first coefficient of the ordering potential (c_{20}), corresponding to slow, modestly restricted rotational dynamics ($\tau_R \sim 76$ ns, $S = 0.36$). Similarly, variation of the diffusion tilt angles β_D and γ_D not did significantly improve the fit, likely because the rotational motion is too near the rigid limit to detect averaging of the *g*-factor and hyperfine tensor components. The observed correlation time is comparable to the rate of PLB uniaxial diffusion ($\tau_R = 105$ ns at 277 K) measured using the TOAC spin label [106], suggesting that BSL is reporting the uniaxial diffusion of PLB within the membrane.

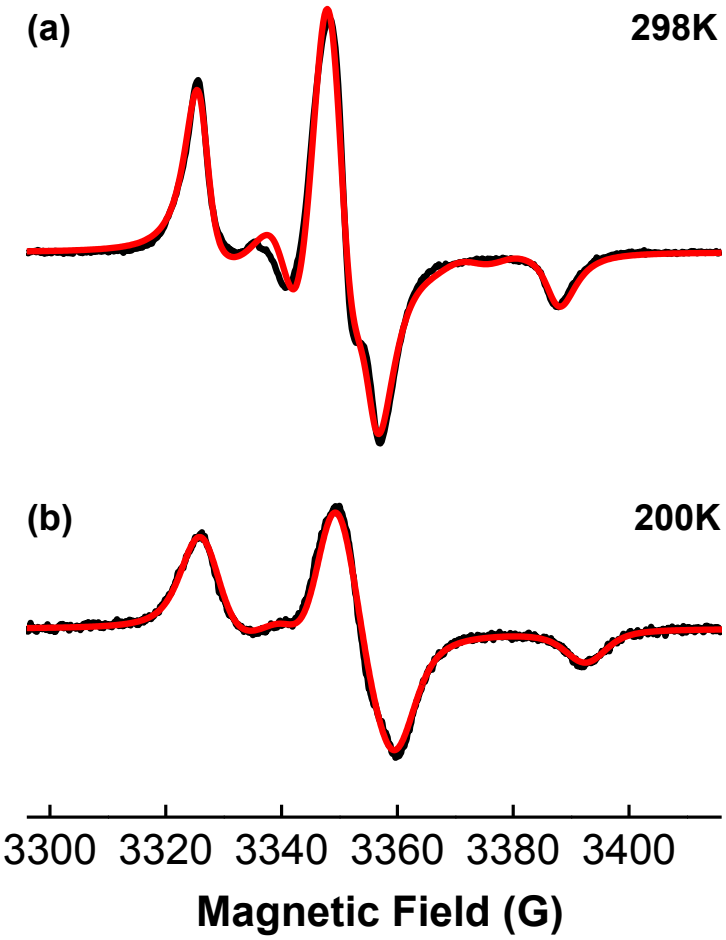

Fig. 47. EPR spectra (black) of 32/36-BSL-PLB in randomly-oriented lipid vesicles, and best fits (red). (a) 298 K, fit generated by NLSL. (b) 200 K, fit generated by WACY. Parameter values from fits are included in Table 6.

To prepare aligned samples, we reconstituted 32/36-BSL-PLB into 2:2:1 (mol/mol) POPC/DMPC/DHexPC bicelles containing 13% (mol/mol) cholesterol and 20% (mol/mol) $TmCl_3$ or $DyCl_3$. This lipid composition (omitting lanthanides) was demonstrated previously to undergo magnetic alignment between 291 - 298 K at NMR field strengths [184], and with the addition of lanthanides we observed complete alignment of POPC/DMPC/DHexPC bicelles containing 5-DOXYL-stearic acid as a reporter (Fig. S53). Parallel- and perpendicular-aligned bicelle spectra are given in Fig. 48, and show dramatic differences in outer splitting indicative of alignment. Based on the

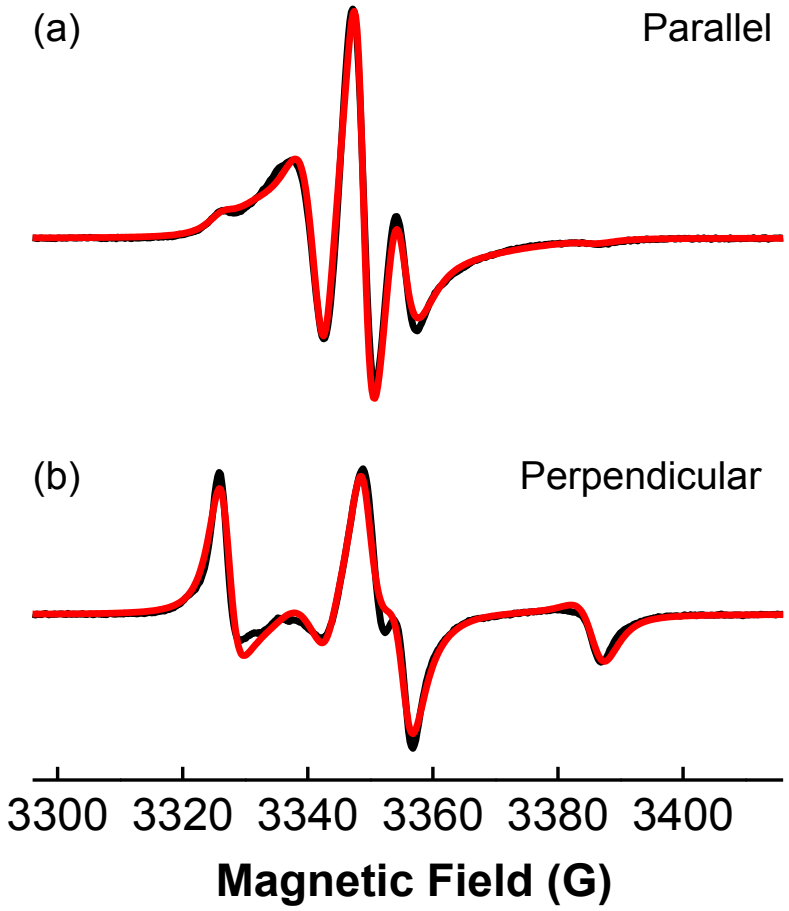

Fig. 48. EPR spectra of 32/36-BSL-PLB in bicelles aligned parallel (a) and perpendicular (b) with respect to the instrument magnetic field. Black: data. Red: best-fit results of global analysis (Table 6).

crystal structure of BSL-T4 lysozyme [93], BSL is predicted to attach along PLB's transmembrane helix with its principal axis (z_M) tilted ~70° relative to the helix long axis (*h*, see Fig. 46). For 32/36-BSL-PLB in parallel ($n \parallel \mathbf{B_0}$) bicelles, where *h* is roughly collinear with the membrane normal (*n*), the EPR spectrum should be dominated by x_M-y_M contributions and possess a narrow outer splitting. In contrast, perpendicular ($n \perp \mathbf{B_0}$) bicelles should yield a spectrum with substantially wider splitting due to contributions from z_M. As expected, narrow splitting of the parallel spectrum (Fig. 48a, $A_{\parallel}' = 10.0$ G) and wide splitting of the perpendicular spectrum (Fig. 48b, $A_{\perp}' = 30.6$ G) indicate that z_M is nearly orthogonal to the membrane normal.

To determine the diffusion tilt angles (β_D, γ_D) relating the nitroxide principal axis (z_M) to the director axis (z_D), we performed global fitting of the parallel and perpendicular bicelle spectra using NLSL, with results given in Table 6. Initial values for the *g*-factor and hyperfine tensors were again taken from the frozen vesicle spectrum, though minor variation of both tensors was necessary to optimize the fit. The director tilt (Ψ) was fixed at 0° and 90° for the parallel and perpendicular spectra, respectively. As with the vesicle spectrum, bicelle spectra were well-described by an isotropic rotational diffusion tensor and the first coefficient of the ordering potential, corresponding to slow, moderately restricted rotational dynamics ($\tau_R \sim 61$ ns, S = 0.56). For the diffusion tilt angles, we found that varying β_D (90.0°) significantly improved the fit. Variation of γ_D (36.8°) also improved the fit quality, however it was only well-defined by global fitting. When $\beta_D \sim 90°$, variation of γ_D only interconverts x_M and y_M, which are not well-resolved at X-band, and so the error associated with γ_D is significant.

As a control, we also acquired spectra from 32-BSL-PLB reconstituted in parallel- and perpendicular-aligned bicelles, shown in Fig. S52. The parallel-aligned spectrum clearly contains multiple components, while the outer splitting appears to decrease, suggesting that 32-BSL-PLB preferentially adopts conformations with its principal axis perpendicular to membrane normal. In contrast, the perpendicular-aligned spectrum does

Spectrum	Temp (K)	g_x	g_y	g_z	$A_\parallel$ (G)	$A_\perp$ (G)	τ_R (ns)	C_{20} (kT)	S	β_D (°)	γ_D (°)
Vesicle	200	2.00866	2.00641	2.00228	33.89	5.92	-	-	-	-	-
Vesicle	298	2.00859	2.00655	2.00225	32.21	5.63	76.2	1.6	0.36	-	-
Bicelle (Global)	298	2.00842	2.00677	2.00242	31.69	5.61	60.5	2.7	0.56	90.0	36.8

Table 6. Parameters from rigid-limit (200 K) and MOMD (298 K) fits to 32/36-BSL-PLB spectra.

not differ significantly from the randomly-oriented vesicle spectrum, as rotational diffusion of 32-BSL-PLB in the bicelle further disorders the probe orientation. Therefore, 32-BSL-PLB demonstrates that monofunctional attachment of BSL does not restrict probe dynamics sufficiently to measure orientation with high precision.

To extract the helical tilt of PLB's transmembrane helix from our EPR measurements, we modeled BSL onto the high-resolution NMR structure of AFA-PLB (PDB 2KB7) [22], using dihedral angles were taken from the crystal structure of BSL-T4-lysozyme [93]. To confirm the stability of this conformation, we performed a 160 ns

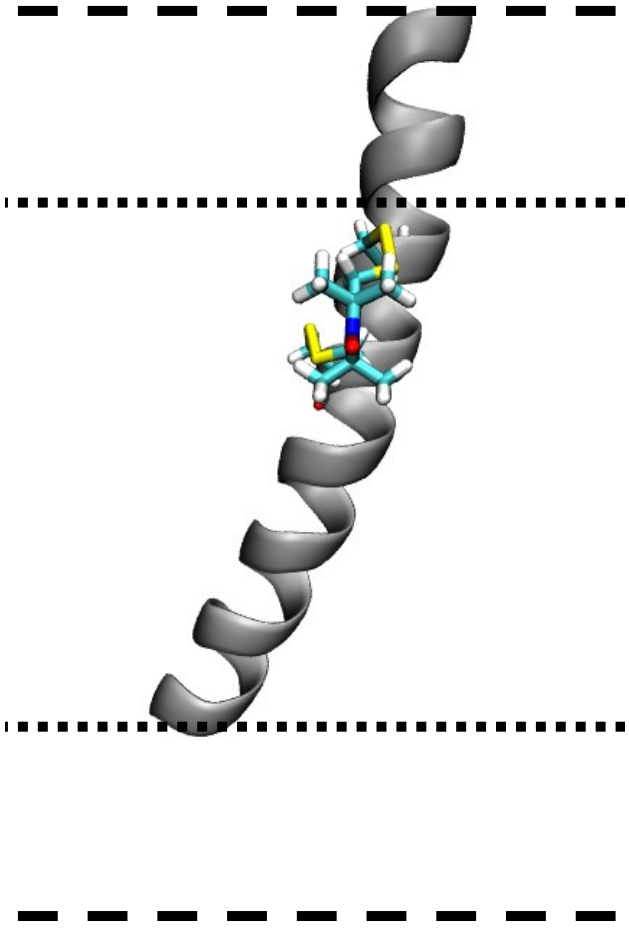

Fig. 49. Molecular dynamics simulation of BSL attached at positions 32 and 36 of the TM helix (residues 23-52) of PLB, aligned to PDB 2KB7 structure [207].

molecular dynamics simulation of the 32/36-BSL-PLB transmembrane helix (omitting cytoplasmic residues 1-24) in implicit solvent. We found the position and orientation of BSL to be largely invariant relative to the helix long axis (*h*), with our simulation reporting an average angle of 67° (FWHM ~ 10°) between *h* and the nitroxide principal axis (z_M). This yields a TM helix tilt of 21.4°, in good agreement with the helix tilt of 21° determined by NMR [22]. There are likely additional modes of motion besides uniaxial diffusion, such as rapid wobble of the helix [208] and dynamics of the spin label relative to PLB that may perturb this measurement. When the simulated 32/36-BSL-PLB TM helix was aligned to the full 2KB7 structure in lipid bilayer, we measured an average angle of 89° (FWHM ~ 5°) between the membrane normal and the nitroxide principal axis (z_M). This is in excellent agreement with β_D (90.0°) from our simulated EPR data.

5.5 Conclusions

We have shown that a bifunctional methanethiosulfonate spin label (BSL) is capable of reporting the structural topology of monomeric PLB reconstituted into magnetically-aligned bicelles. Using POPC/DMPC mixed bicelles, we were able to prepare oriented samples at physiological temperature (298 K), acquiring spectra from both parallel and perpendicular samples. Fitting the randomly oriented samples (vesicles), as well as the parallel and perpendicular bicelle spectra simultaneously resulted in sufficient fitting convergence. We determined that while both monofunctionally (32-BSL-PLB) and bifunctionally (32/36-BSL-PLB) attached BSL were immobilized on PLB's TM helix (Fig. 47), bifunctional attachment is necessary for sufficient orientation

resolution (Fig. S52). We also determined that at the incorporated position (32,36), BSL makes a 90^{o} angle with the membrane normal. This result was well-corroborated with a molecular dynamics simulation.

In principle, EPR spectroscopy is exquisitely sensitive to the orientation of spin labels with respect to the applied magnetic field, although this resolution is usually obscured by the rotational mobility of conventional labels. The majority of bicelle EPR studies to date have relied on TOAC, which is limited to small proteins. The bifunctional spin label used here may be applied to larger proteins, requiring only two cysteine mutations on a protein segment with well-ordered secondary structure, such as a helix.

5.6 Acknowledgements

This work was supported in part by NIH grants GM27906 and AR057220 to DDT. ZMJ was supported by NIH Training Grants AR007612 and GM008700, and JEM was supported by NIH Training Grant AR007612. EPR experiments were performed at the Biophysical Spectroscopy Center. Computational resources were provided by the Minnesota Supercomputing Institute. We thank Edmund Howard for EPR simulation assistance and helpful discussions, and Octavian Cornea for assistance in preparing the manuscript.

5.7 Supplemental Information

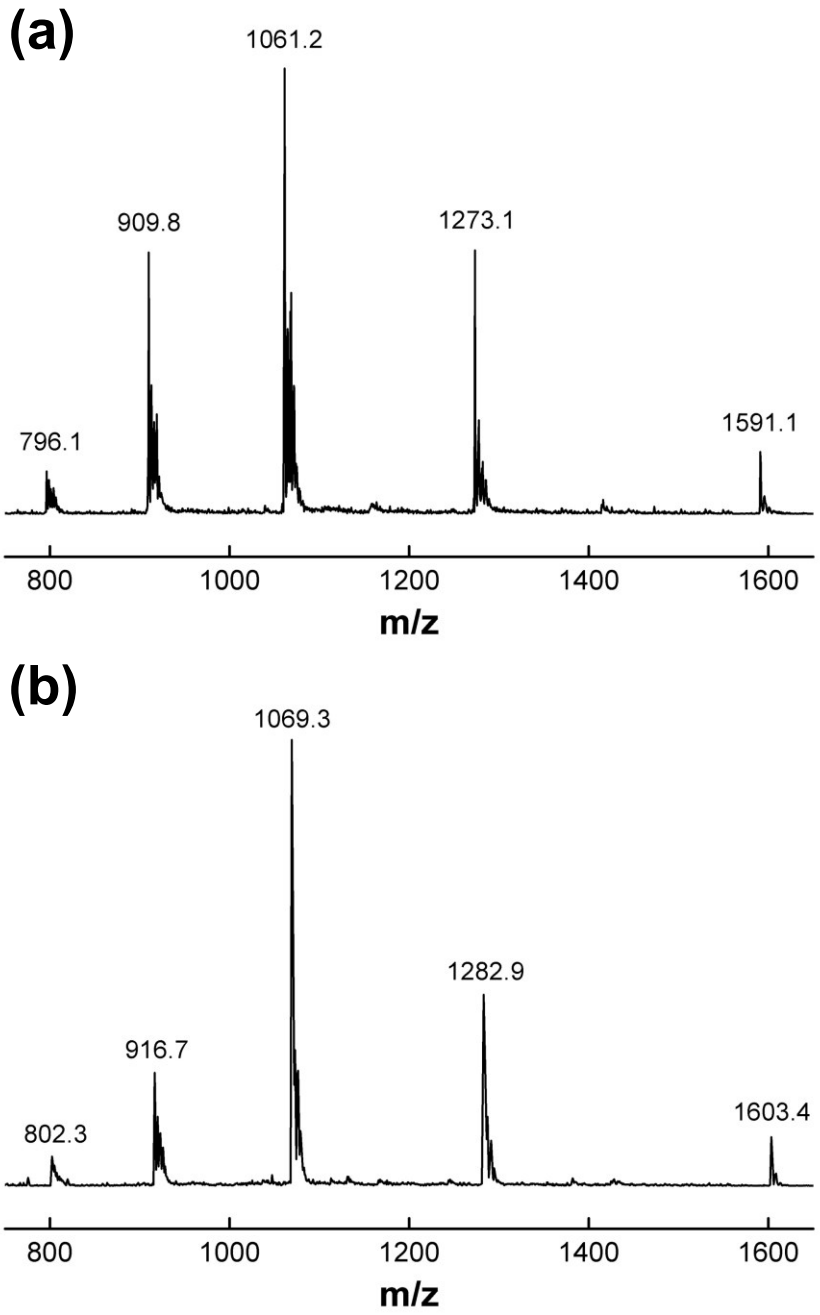

Fig. S50. Electrospray ionization (ESI) mass spectrometry of 32/36-BSL-PLB (a) and 32-BSL-PLB (b).

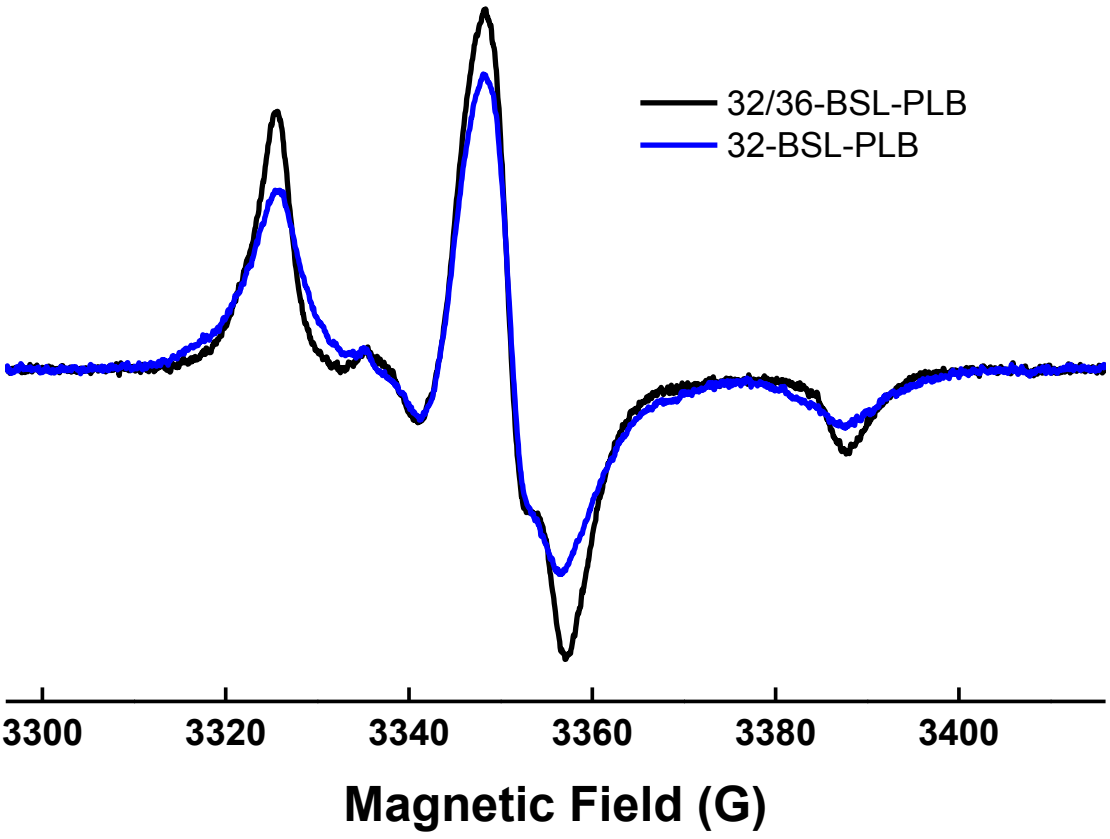

Fig. S51. Conventional EPR spectra of 32/36-BSL-PLB (black) and 32-BSL-PLB (blue) in randomly-oriented vesicles at 298 K.

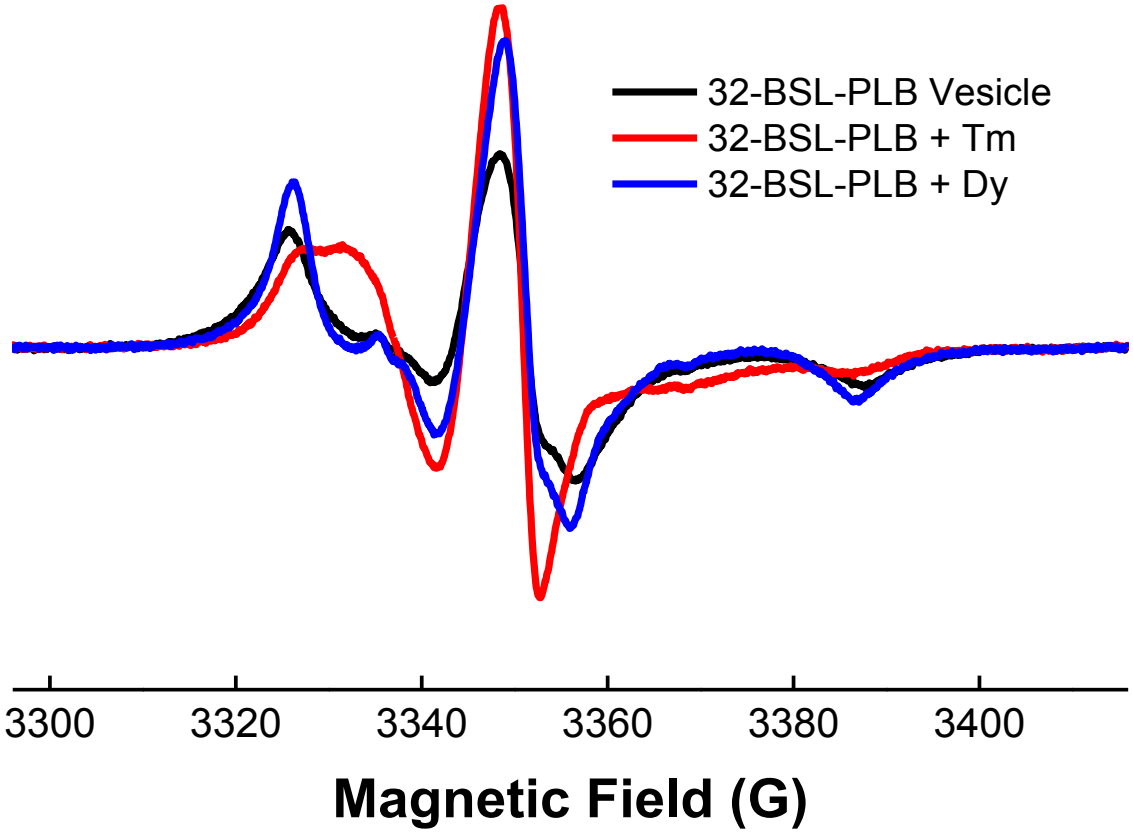

Fig. S52. Conventional EPR spectra of 32-BSL-PLB in randomly oriented vesicles (black), parallel oriented bicelles (red), and perpendicular oriented bicelles (blue) at 298 K.

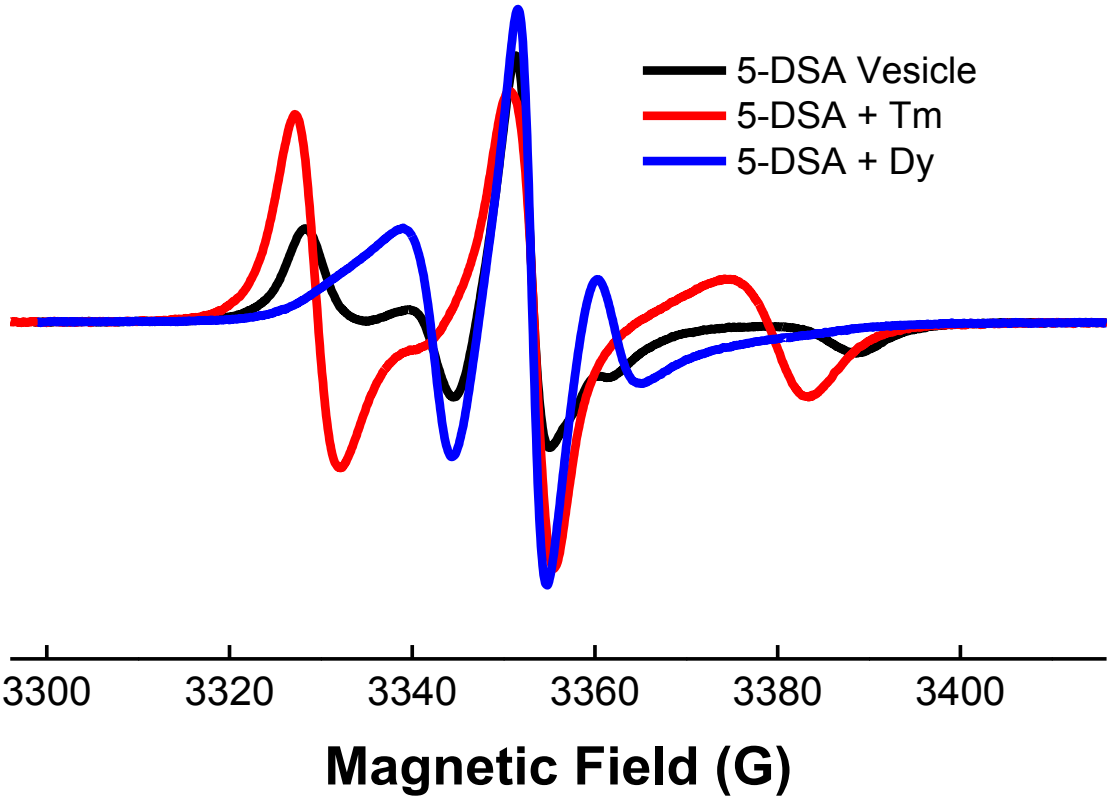

Fig. S53. Conventional EPR spectra of 5-DOXYL-stearic acid in randomly oriented vesicles (black), parallel oriented bicelles (red), and perpendicular oriented bicelles (blue) at 298 K.

Chapter 6: Probing Phospholamban Orientation in the Presence of SERCA – Ongoing Research

6.1 Introduction

My current research aims to measure PLB orientation within the SERCA-PLB complex, to further elucidate the inhibitory and non-inhibitory conformations of PLB. To date, no group has performed EPR measurements on large transmembrane protein complexes like SERCA-PLB in oriented bicelles. The addition of SERCA to oriented bicelle samples requires detergent reconstitution, where detergent is added to permeabilize lipid bilayers and facilitate incorporation of large membrane proteins [209]. However, there are several challenges to combining detergent reconstitutions with bicelles.

The short-chain lipid used to prepare bicelles, DHexPC, is quite similar to the detergents β-octyl glucoside (β-OG) and octaethylene glycol monododecyl ether ($C_{12}E_8$), meaning that any residual detergent will change the bicelle q. This necessitates adding DHexPC after reconstitution and detergent removal, since it would also be removed along with the detergent. Also, the cross-sectional area of SERCA is about 16 times larger than that of PLB or a typical lipid (~13 nm^2 vs ~0.8 nm^2), so these large membrane proteins further perturb the effective bicelle q.

Prior to studies on PLB orientation in bicelles containing SERCA, we spent a considerable amount of time performing control experiments with the 5-DOXYL-stearic acid spin label, attempting to characterize the critical aspects of forming and aligning

bicelles, with emphasis on the detergent reconstitution needed to prepare SERCA bicelles. Chapter 5 highlights optimization of temperature and POPC:DMPC molar ratio in bicelles, but several other characteristics were explored. The total concentration of lipid with respect to buffer volume is essential for bicelle alignment. Bicelle samples where the total lipid concentration is <25% w/v (weight lipid per volume solution) do not align well, likely because diluting the bicelles prevents them from forming large lamellar sheets at elevated temperature. Exceeding this lipid concentration leads to viscous samples that are difficult to pipette and contain lipid aggregation. These observations are corroborated by previous NMR studies [210]. Bicelle q is also an important parameter for successful alignment. In bicelle samples containing either 5-DOXYL-stearic acid or TOAC-AFA, $3 < q < 6$ produces sufficient alignment homogeneity, with $q \sim 4$ being optimal. Bicelles with $q < 3$ become isotropic and will not align, while bicelles with $q > 6$ produce a very viscous solution and align poorly. This is approximately the range used in NMR experiments [172]. Interestingly, bicelles prepared by the reconstitution method (see Section 6.2) show improved alignment at lower q, requiring $q \sim 3$ even for modest alignment. Presumably, residual detergent and/or the effect of SERCA on the flat bilayer area necessitate a different bicelle q. Cholesterol is also essential for bicelle alignment. The 13% (mol cholesterol / mol LC lipid) used by the Lorigan lab works well [178], with less or more cholesterol degrading alignment homogeneity. Finally, the decrease in magnetic field strength after bicelle alignment for spectrum acquisition does not seem to affect bicelle alignment for well-ordered samples. In one experiment, the magnetic field was turned completely off for 30 minutes before acquisition, and demonstrated similar

lineshape to those that were acquired immediately after alignment. Temperature is the critical parameter for maintaining bicelle alignment, as observed previously [211].

Another technique that has aided experiments is the use of Q-band EPR spectroscopy. Fitting the preliminary X-band data proved largely unsuccessful, so we sought to constrain the fitting routine further with additional data acquired at Q-band. Global fitting of the X-band and Q-band data has improved fit convergence, producing results that are self-consistent, and also consistent with previous models of SERCA-PLB regulation.

6.2 Methods

36-TOAC-AFA-PLB (36-TOAC-PLB), phosphorylated 36-TOAC-AFA-PLB (36-TOAC-pPLB) and reactive red SERCA were prepared and purified as described previously [61]. PLB was combined with lipids (equimolar DMPC and POPC), and cholesterol, all dissolved in chloroform. This produced vesicles with 1400 lipids per PLB, 13% cholesterol (mol cholesterol / mol long-chain lipid). Organic solvent was evaporated under N_2 gas and then completely removed by storage in a vacuum desiccator overnight. Samples were then brought up to 3 mL total volume, 10 mM lipid, 55 mM β-OG, and 100 mM HEPES (pH 7.0) using appropriate stocks. Purified SERCA was added at a 2:1 molar ratio with PLB, then stirred for five minutes. β-OG was adsorbed using Bio-Beads SM2 (30 mg Bio-Beads per mg β-OG), added in three equal batches over three hours, and stirred on an inverter. Samples were then diluted up to 75 mL (to reduce the effect of any residual detergent), and centrifuged at 100,000 relative centrifugal force (RCF, or

times gravity) at 4 °C for one hour. After removal of supernatant, DHexPC in 100 mM HEPES (pH 7.0) was added to the protein/lipid pellet to produce a q ratio of 3, and lanthanide stock ($TmCl_3*6H_2O$ in 100 mM HEPES) was added to the sample up to 20% (mol lanthanide / mol long-chain lipid). The sample was vortexed for 2 min and placed on ice for 5 min a total of three times, then briefly sonicated. 16 μL of the sample was pipetted into a 0.6/0.84 mm ID/OD glass capillary, then plugged with Critoseal.

X-band / Q-band EPR experiments were performed on a Bruker EleXsys E500 / E580 spectrometer equipped with an ER 4122 SHQ / ER 5106 QT resonator. Samples were first placed in the resonator and equilibrated at 273 K for 5 min. To align bicelles, the field strength was raised to 1.1 T / 1.2 T, then the temperature was raised 2 K per minute up to 298 K, at which point the sample was incubated for 20 min at 1.1 T / 1.2 T field strength. The EPR spectrum was then acquired at X-band / Q-band field strength (~3400 G / ~12000 G) at 298 K. For randomly oriented vesicle samples, spectra were acquired immediately after the initial 5 minute equilibration at 298 K. EPR spectra were acquired with the parameters specified in Table 7:

Frequency Band	Temp (K)	Center Field (G)	Sweep Width (G)	Modulation Amplitude (G)	Microwave Power (mW)	Time Constant (ms)	Conversion Time (ms)
X (9.5 GHz)	298	3356	120	1	2	20.48	20.48
Q (35 GHz)	298	12130	200	1	1	20.48	20.48

Table 7. EPR acquisition parameters for X-band and Q-band bicelle samples.

6.3 Results

Initial experiments with 36-TOAC-AFA began at X-band in the absence of SERCA. Fig. 54 (left) shows the EPR spectra of 36-TOAC-PLB and 36-TOAC-pPLB in

randomly oriented vesicles and bicelles. The substantial change in lineshape between the vesicle (black) and bicelle (red) spectra for samples without SERCA (left) is indicative of homogeneous alignment, which was also evident in spectral fitting. Phosphorylation had little effect on both these vesicle and bicelle sample spectra, indicating that the TM helix of PLB is relatively unaffected by phosphorylation in the absence of SERCA.

Fig. 54 (right) shows the EPR spectra of 36-TOAC-PLB and 36-TOAC-pPLB samples in the presence of 2:1 SERCA:PLB. Comparing the spectra for vesicle and bicelle samples containing SERCA, the difference in lineshape is less than that observed for the PLB-only samples, suggesting lower alignment homogeneity. Indeed, the spectra do not fit well to a single oriented component or to a two-component model containing both a singly oriented and randomly oriented components. This suggests that PLB's TM

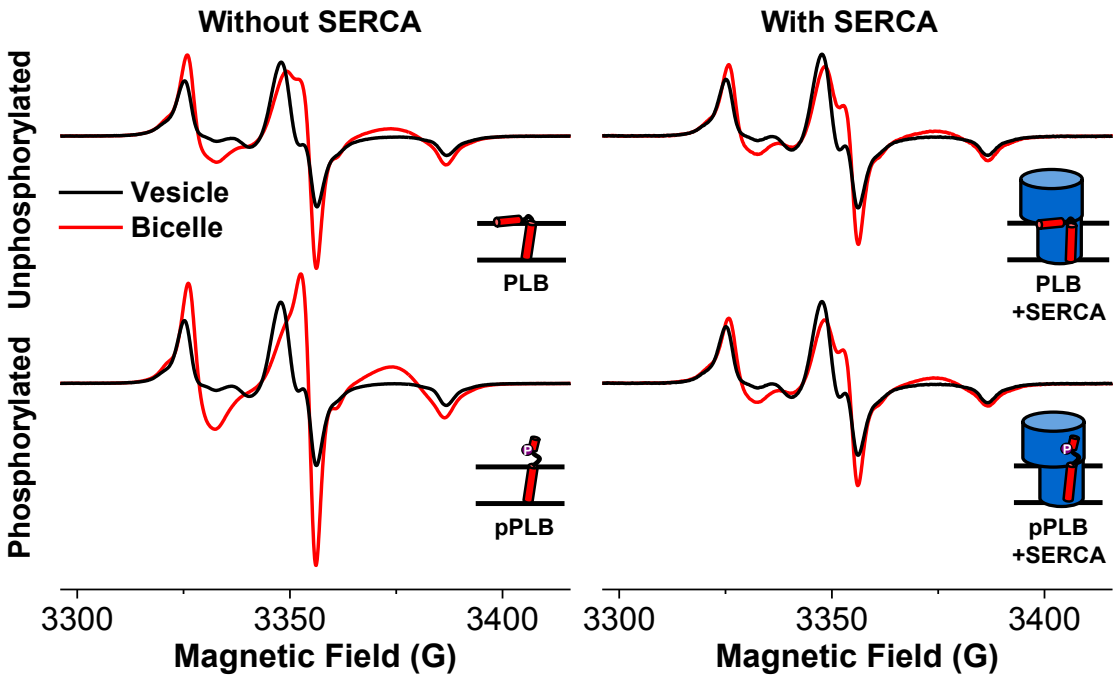

Fig. 54. X-band EPR spectra of 36-TOAC-PLB (top) and 36-TOAC-pPLB (bottom) in randomly oriented vesicles (black) and bicelles aligned parallel with respect to the instrument magnetic field (red), in the absence (left) and presence (right) of 2:1 SERCA:PLB.

helix adopts several conformations in the presence of SERCA, or the EPR spectra are not sufficiently resolved to converge the fitting routine.

This result prompted the use of Q-band EPR spectroscopy on 36-TOAC-PLB samples, as the potential increased sensitivity to orientation and opportunity for global analysis with previous X-band data could resolve the ambiguity observed in the SERCA-containing samples at X-band. Fig. 55 (left) shows the Q-band EPR spectra of 36-TOAC-PLB and 36-TOAC-pPLB in randomly oriented vesicles and bicelles, corresponding to the X-band EPR spectra shown in Fig. 54. Similar to Fig. 54, the Q-band EPR spectra in Fig. 55 demonstrate substantial alignment in bicelle samples, with PLB phosphorylation having little effect on both the vesicle and bicelle sample spectra. In the presence of

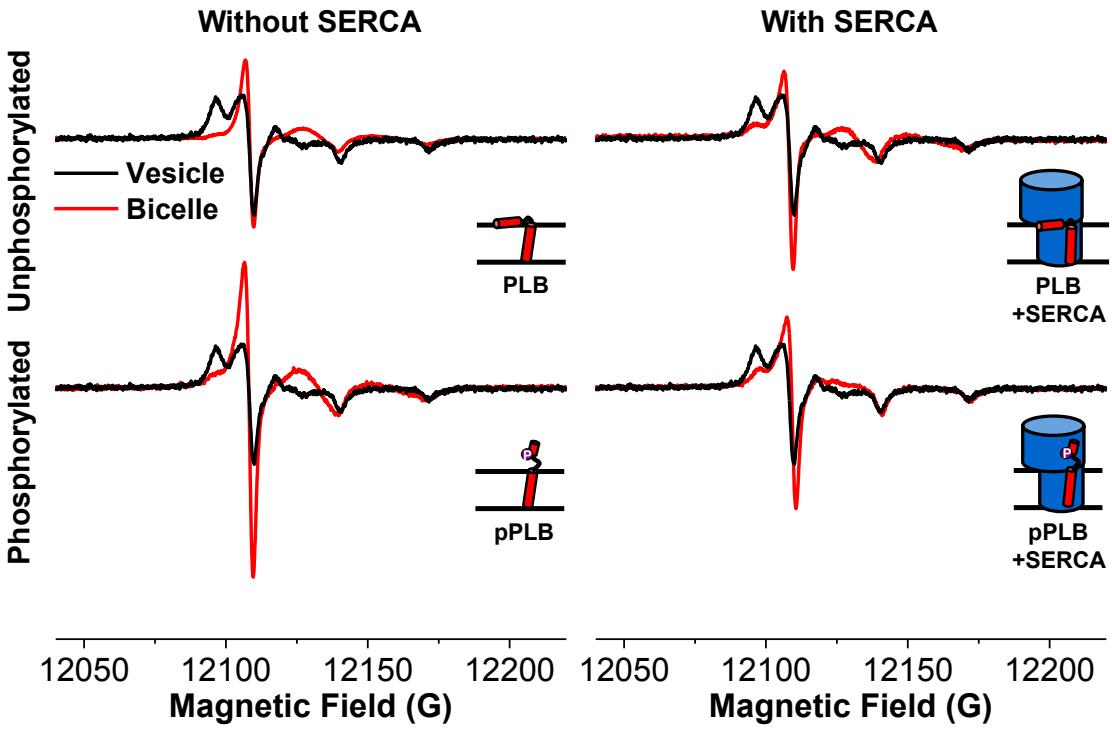

Fig. 55. Q-band EPR spectra of 36-TOAC-PLB and 36-TOAC-pPLB with and without 2:1 SERCA:PLB in randomly oriented vesicles and bicelles aligned parallel with respect to the instrument magnetic field.

SERCA (Fig. 55, right), there are subtle changes in the spectral lineshape upfield of the central resonance upon phosphorylation that were not observed in the X-band data.

Global fitting of the X-band and Q-band data determined a PLB TM helix tilt angle of 35.6° (Fig. 56). This angle differs from the angle determined by NMR (21°) [207], which could be due to the use of a different membrane system or an alternate

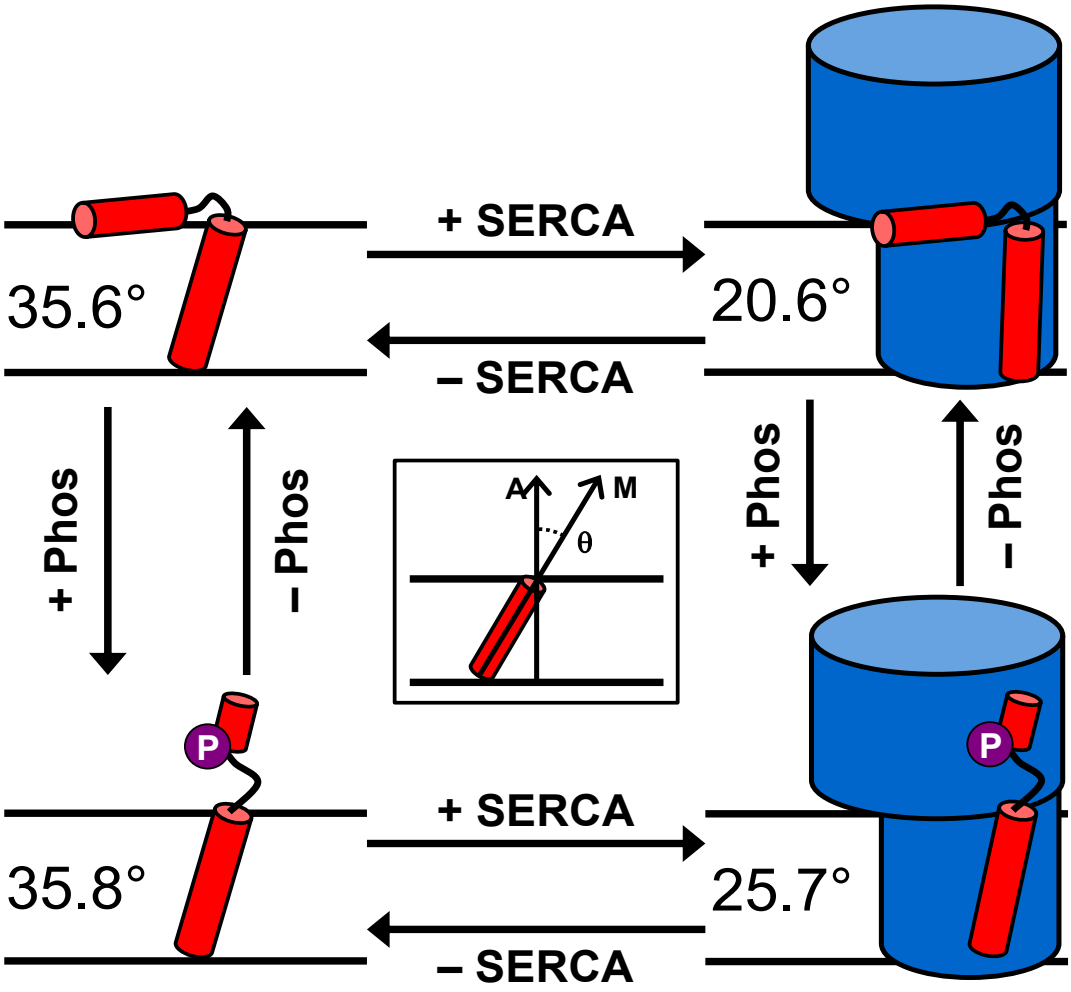

Fig. 56. Diffusion tilt angles for PLB TM helix determined by preliminary fitting of oriented bicelle EPR on 36-TOAC-PLB. The diffusion tilt angle (θ) is defined as the angle between the membrane normal (A) and the PLB TM helix axis (M) (see center inset). PLB phosphorylation in the absence of SERCA (left) causes little change in θ. SERCA binding causes a significant decrease in θ, while phosphorylation of SERCA-bound PLB partially reverses this decrease in θ.

conformation of TOAC upon PLB. Phosphorylation yields β_D = 35.8°, suggesting no significant change in PLB TM helix tilt due to phosphorylation In contrast, SERCA binding significantly decreases the PLB TM helix tilt angle to 20.6°, while phosphorylation of SERCA-bound PLB partially reverses this decrease, such that β_D = 25.7°.

6.4 Conclusions

While still in progress, this research has produced several valuable conclusions regarding SERCA bicelle methodology and PLB orientation in the presence of SERCA. Well-orienting bicelles possess a high lipid to solvent ratio, a q that has been optimized for the system under study, and a modest amount of cholesterol. Additionally, the use of multifrequency EPR improves fit convergence significantly over both X-band and Q-band EPR individually. Using the 36-TOAC-PLB construct, no significant change in TM helix tilt is observed for PLB alone after phosphorylation. Binding to SERCA decreases the tilt angle, causing the TM helix to be more parallel with the membrane normal. Phosphorylation of SERCA-bound PLB partially reverses this tilt change.

Several additional experiments need to be conducted for this project before a full analysis can be completed. The activity of SERCA, including inhibition by PLB and phosphorylation-induced reversal of PLB inhibition, should be verified with calcium-dependent ATPase functional assays. Calcium should also be regulated in future samples with ethylene glycol tetraacetic acid (EGTA), a calcium chelating molecule. Additional

trials should be conducted, including with the 32/36-BSL-PLB mutant introduced in Chapter 5, since it demonstrated a well-defined orientation distribution.

The increase in PLB TM helix tilt upon phosphorylation in the presence of SERCA could correspond to a fraction of PLB that has dissociated from SERCA, as previous studies have detected decreased binding affinity upon phosphorylation [57, 212]. This could be evaluated by performing saturation transfer EPR on identical bicelle samples, and verify previous results supporting the subunit model still hold in the current bicelle system [61].

A limitation to the orientation data obtained in the presence of SERCA is that it cannot resolve the direction of PLB's helical tilt relative to SERCA. This tilt may face towards, away, or along the binding interface of SERCA. Cross-linking studies have found several residues at the beginning and ends of PLB domain II that are important for SERCA binding, suggesting that the tilt may occur along the binding interface [52, 53]. Accessibility EPR studies in progress in our laboratory may be able to resolve this by detecting changes in PLB residue accessibility upon phosphorylation.

Chapter 7: Final Conclusions and Future Directions

My thesis work has advanced both knowledge of the SERCA-PLB structure-function relationship, and spectroscopic methods to continue these studies in greater detail. Below, I outline the primary methods and results from each chapter, and follow with motivation and outline for future experiments.

In Chapter 3, I measured the rotational dynamics of PLB as affected by phosphorylation and binding to SERCA. By incorporating spin labels into PLB and SERCA and reconstituting these proteins into lipid vesicles, I measured their rotational mobility by conventional and saturation transfer EPR. I determined that phosphorylation of SERCA-bound PLB does not dissociate the SERCA-PLB complex, supporting the subunit model of regulation. I also characterized concentration-dependent protein oligomerization, identifying conditions where monomeric PLB, SERCA, and SERCA-PLB complexes can be studied.

In Chapter 4, I optimized lipid bicelle composition, reconstituting the 5-DOXYL-stearic acid lipid spin label into bicelles with different ratios of DMPC and POPC, and aligning these bicelles up to different temperatures. Through these experiments, I determined that an equimolar mixture of DMPC and POPC reduced the necessary alignment temperature by 20 K, compared to conventional DMPC-only bicelles. This makes possible orientation measurements on membrane proteins at physiological conditions, which is essential for preserving native structure and dynamics.

In Chapter 5, I utilized the bicelle methodology from Chapter 4 to probe PLB orientation in its membrane environment. Through cysteine mutagenesis, I attached a bifunctional spin label (BSL) at positions 32 and 36 on PLB's TM helix, and reconstituted it into POPC/DMPC bicelles. Through a combination of oriented bicelle EPR and molecular dynamics simulations, I found that the principal axis of BSL at positions 32/36 on PLB forms a 90° angle with the bilayer normal, and a 76° angle with the PLB TM helix axis. From these, I determined a PLB TM helix tilt angle of 21°, consistent with previous NMR measurements. I also demonstrated through a single cysteine PLB mutant, that monofunctionally attached BSL is not sufficiently restricted for orientation measurements. This suggests that singly attached spin labels like MSL and MTSL are not suitable for oriented bicelle EPR, and that rigid probes such as TOAC and BSL are required.

In Chapter 6, I reconstituted 36-TOAC-PLB and SERCA into bicelles to determine changes in PLB TM helix tilt angle due to phosphorylation and SERCA binding. Control experiments motivated several modifications to the bicelle protocol developed in Chapter 4, including detergent reconstitution and reduced bicelle q. Preliminary results find no significant change in helix tilt angle after phosphorylation for PLB alone, with a 15° decrease in helix tilt upon binding to SERCA, and a partial reversal of this decrease upon phosphorylation (5.7°). Along with the results from Chapter 3, this suggests that relief of SERCA inhibition by PLB phosphorylation occurs by subtle structural changes within the SERCA-PLB transmembrane binding region.

Additional EPR measurements with TOAC and functional assays should be performed to confirm these results.

A wide variety of additional experiments remain to expand upon the results presented in this thesis work. The SERCA-PLB dynamics measurements performed in Chapter 3 were done at low calcium concentration (pCa = 6.5) to maximize PLB inhibition. In vivo, calcium concentration can be several hundred times above this [8]. Several studies suggest that PLB has decreased binding affinity, or cannot bind at all, to SERCA with calcium bound to it [21, 57, 58]. These results could be verified using the same combination of conventional and saturation transfer EPR as used in Chapter 3.

Additionally, while dilute protein concentrations were used in those experiments to ensure monomeric conditions and simplify analysis, the system is much more crowded in vivo (<100 lipids per SERCA vs 700 lipids per SERCA) [213]. Protein oligomerization is known to play an important role in calcium regulation; this could be investigated using saturation transfer EPR. The possible emergence of multiple oligomeric states and spin-spin interactions makes this a difficult measurement, so care would be needed to gradually introduce higher oligomeric states, starting with dimers.

TOAC and BSL are both rigidly coupled spin labels that can be used to study protein dynamics and orientation. However, they differ in their conformation on the peptide backbone. On the PLB TM helix, TOAC's principal axis makes a 14° angle with the helix axis, while BSL's principal axis makes a 76° angle with the helix axis. This suggests that TOAC and BSL can be used together to improve orientation measurement accuracy. Indeed, comparison of oriented bicelle EPR spectra with 36-TOAC-PLB and

32/36-BSL-PLB show this complementary property. This relationship could be further characterized and put into practice for enhanced measurements.

References

1. Bers, D.M., *Cardiac excitation-contraction coupling.* Nature, 2002. **415**(6868): p. 198-205.
2. Huxley, H. and J. Hanson, *Changes in the cross-striations of muscle during contraction and stretch and their structural interpretation.* Nature, 1954. **173**(4412): p. 973-6.
3. Huxley, A.F. and R. Niedergerke, *Structural changes in muscle during contraction; interference microscopy of living muscle fibres.* Nature, 1954. **173**(4412): p. 971-3.
4. Spudich, J.A., *The myosin swinging cross-bridge model.* Nature reviews. Molecular cell biology, 2001. **2**(5): p. 387-92.
5. Solaro, R.J. and H.M. Rarick, *Troponin and tropomyosin: proteins that switch on and tune in the activity of cardiac myofilaments.* Circulation research, 1998. **83**(5): p. 471-80.
6. Filatov, V.L., et al., *Troponin: structure, properties, and mechanism of functioning.* Biochemistry. Biokhimiia, 1999. **64**(9): p. 969-85.
7. Clapham, D.E., *Calcium signaling.* Cell, 1995. **80**(2): p. 259-68.
8. Pieske, B., et al., *Ca2+ handling and sarcoplasmic reticulum Ca2+ content in isolated failing and nonfailing human myocardium.* Circulation research, 1999. **85**(1): p. 38-46.
9. Kirchberger, M.A., et al., *Cyclic adenosine 3',5'-monophosphate-dependent protein kinase stimulation of calcium uptake by canine cardiac microsomes.* Journal of molecular and cellular cardiology, 1972. **4**(6): p. 673-80.
10. MacLennan, D.H. and E.G. Kranias, *Phospholamban: a crucial regulator of cardiac contractility.* Nat Rev Mol Cell Biol, 2003. **4**(7): p. 566-77.
11. Toyoshima, C. and H. Nomura, *Structural changes in the calcium pump accompanying the dissociation of calcium.* Nature, 2002. **418**(6898): p. 605-11.
12. Moller, J.V., et al., *The sarcoplasmic Ca2+-ATPase: design of a perfect chemi-osmotic pump.* Q Rev Biophys, 2010. **43**(4): p. 501-66.
13. Brandl, C.J., et al., *Two Ca2+ ATPase genes: homologies and mechanistic implications of deduced amino acid sequences.* Cell, 1986. **44**(4): p. 597-607.
14. Lytton, J. and D.H. MacLennan, *Molecular cloning of cDNAs from human kidney coding for two alternatively spliced products of the cardiac Ca2+-ATPase gene.* The Journal of biological chemistry, 1988. **263**(29): p. 15024-31.
15. Anger, M., et al., *The sarco(endo)plasmic reticulum Ca(2+)-ATPase mRNA isoform, SERCA 3, is expressed in endothelial and epithelial cells in various organs.* FEBS letters, 1993. **334**(1): p. 45-8.
16. Periasamy, M. and A. Kalyanasundaram, *SERCA pump isoforms: their role in calcium transport and disease.* Muscle & nerve, 2007. **35**(4): p. 430-42.
17. Toyofuku, T., et al., *Identification of regions in the Ca(2+)-ATPase of sarcoplasmic reticulum that affect functional association with phospholamban.* J Biol Chem, 1993. **268**(4): p. 2809-15.

18. Zhang, Z., et al., *Detailed characterization of the cooperative mechanism of Ca(2+) binding and catalytic activation in the Ca(2+) transport (SERCA) ATPase.* Biochemistry, 2000. **39**(30): p. 8758-67.
19. Toyoshima, C., et al., *Trinitrophenyl derivatives bind differently from parent adenine nucleotides to Ca2+-ATPase in the absence of Ca2+.* Proceedings of the National Academy of Sciences, 2011. **108**(5): p. 1833-8.
20. Toyoshima, C., et al., *Crystal structure of the calcium pump of sarcoplasmic reticulum at 2.6 A resolution.* Nature, 2000. **405**(6787): p. 647-55.
21. Akin, B.L., et al., *The structural basis for phospholamban inhibition of the calcium pump in sarcoplasmic reticulum.* The Journal of biological chemistry, 2013. **288**(42): p. 30181-91.
22. Traaseth, N.J., et al., *Structure and topology of monomeric phospholamban in lipid membranes determined by a hybrid solution and solid-state NMR approach.* Proceedings of the National Academy of Sciences, 2009. **106**(25): p. 10165-70.
23. Karim, C.B., et al., *Phospholamban structural dynamics in lipid bilayers probed by a spin label rigidly coupled to the peptide backbone.* Proc Natl Acad Sci U S A, 2004. **101**(40): p. 14437-42.
24. Mascioni, A., et al., *Solid-state NMR and rigid body molecular dynamics to determine domain orientations of monomeric phospholamban.* J Am Chem Soc, 2002. **124**(32): p. 9392-3.
25. Karim, C.B., et al., *Phosphorylation-dependent Conformational Switch in Spin-labeled Phospholamban Bound to SERCA.* J Mol Biol, 2006. **358**(4): p. 1032-40.
26. Ha, K.N., et al., *Controlling the Inhibition of the Sarcoplasmic Ca2+-ATPase by Tuning Phospholamban Structural Dynamics.* J Biol Chem, 2007. **282**(51): p. 37205-14.
27. Li, J., et al., *Structural and Functional Dynamics of an Integral Membrane Protein Complex Modulated by Lipid Headgroup Charge.* J Mol Biol, 2012.
28. Fujii, J., et al., *Complete complementary DNA-derived amino acid sequence of canine cardiac phospholamban.* The Journal of clinical investigation, 1987. **79**(1): p. 301-4.
29. Wegener, A.D. and L.R. Jones, *Phosphorylation-induced mobility shift in phospholamban in sodium dodecyl sulfate-polyacrylamide gels. Evidence for a protein structure consisting of multiple identical phosphorylatable subunits.* The Journal of biological chemistry, 1984. **259**(3): p. 1834-41.
30. Cornea, R.L., et al., *Mutation and phosphorylation change the oligomeric structure of phospholamban in lipid bilayers.* Biochemistry, 1997. **36**(10): p. 2960-7.
31. Kimura, Y., et al., *Phospholamban inhibitory function is activated by depolymerization.* The Journal of biological chemistry, 1997. **272**(24): p. 15061-4.
32. Traaseth, N.J., et al., *Spectroscopic validation of the pentameric structure of phospholamban.* Proceedings of the National Academy of Sciences, 2007. **104**(37): p. 14676-81.
33. Becucci, L., et al., *On the function of pentameric phospholamban: ion channel or storage form?* Biophysical journal, 2009. **96**(10): p. L60-2.

34. Simmerman, H.K., et al., *A leucine zipper stabilizes the pentameric membrane domain of phospholamban and forms a coiled-coil pore structure.* The Journal of biological chemistry, 1996. **271**(10): p. 5941-6.
35. Robia, S.L., et al., *Forster transfer recovery reveals that phospholamban exchanges slowly from pentamers but rapidly from the SERCA regulatory complex.* Circ Res, 2007. **101**(11): p. 1123-9.
36. Mascioni, A., B.L. Eggimann, and G. Veglia, *Determination of helical membrane protein topology using residual dipolar couplings and exhaustive search algorithm: application to phospholamban.* Chemistry and physics of lipids, 2004. **132**(1): p. 133-44.
37. Tada, M., et al., *Effects of phospholamban phosphorylation catalyzed by adenosine 3':5'-monophosphate- and calmodulin-dependent protein kinases on calcium transport ATPase of cardiac sarcoplasmic reticulum.* Journal of molecular and cellular cardiology, 1983. **15**(5): p. 335-46.
38. Tada, M. and M. Kadoma, *Regulation of the Ca2+ pump ATPase by cAMP-dependent phosphorylation of phospholamban.* Bioessays, 1989. **10**(5): p. 157-63.
39. Jones, L.R., et al., *Purification and characterization of phospholamban from canine cardiac sarcoplasmic reticulum.* The Journal of biological chemistry, 1985. **260**(12): p. 7721-30.
40. Wegener, A.D., et al., *Phospholamban phosphorylation in intact ventricles. Phosphorylation of serine 16 and threonine 17 in response to beta-adrenergic stimulation.* The Journal of biological chemistry, 1989. **264**(19): p. 11468-74.
41. Ablorh, N.A., Dong, X., James, Z. M., Langer, H. R., Thomas, D. D., and Karim, C. B., *Distinct functional effects of phospholamban phosphorylation states.* J Biol Chem, 2014. Submitted.
42. Mundina-Weilenmann, C., et al., *Immunodetection of phosphorylation sites gives new insights into the mechanisms underlying phospholamban phosphorylation in the intact heart.* The Journal of biological chemistry, 1996. **271**(52): p. 33561-7.
43. Li, M., et al., *A fluorescence energy transfer method for analyzing protein oligomeric structure: application to phospholamban.* Biophysical journal, 1999. **76**(5): p. 2587-99.
44. Hou, Z., E.M. Kelly, and S.L. Robia, *Phosphomimetic mutations increase phospholamban oligomerization and alter the structure of its regulatory complex.* The Journal of biological chemistry, 2008. **283**(43): p. 28996-9003.
45. Metcalfe, E.E., N.J. Traaseth, and G. Veglia, *Serine 16 phosphorylation induces an order-to-disorder transition in monomeric phospholamban.* Biochemistry, 2005. **44**(11): p. 4386-96.
46. Traaseth, N.J., D.D. Thomas, and G. Veglia, *Effects of Ser16 phosphorylation on the allosteric transitions of phospholamban/Ca(2+)-ATPase complex.* Journal of molecular biology, 2006. **358**(4): p. 1041-50.
47. Traaseth, N.J. and G. Veglia, *Probing excited states and activation energy for the integral membrane protein phospholamban by NMR CPMG relaxation dispersion experiments.* Biochimica et biophysica acta, 2010. **1798**(2): p. 77-81.

48. Gustavsson, M., N.J. Traaseth, and G. Veglia, *Probing ground and excited states of phospholamban in model and native lipid membranes by magic angle spinning NMR spectroscopy.* Biochimica et biophysica acta, 2012. **1818**(2): p. 146-53.
49. De Simone, A., et al., *Structures of the excited states of phospholamban and shifts in their populations upon phosphorylation.* Biochemistry, 2013. **52**(38): p. 6684-94.
50. Kirchberber, M.A., M. Tada, and A.M. Katz, *Phospholamban: a regulatory protein of the cardiac sarcoplasmic reticulum.* Recent advances in studies on cardiac structure and metabolism, 1975. **5**: p. 103-15.
51. Toyoshima, C., et al., *Modeling of the inhibitory interaction of phospholamban with the Ca2+ ATPase.* Proc Natl Acad Sci U S A, 2003. **100**(2): p. 467-72.
52. Chen, Z., et al., *Spatial and dynamic interactions between phospholamban and the canine cardiac Ca2+ pump revealed with use of heterobifunctional cross-linking agents.* The Journal of biological chemistry, 2003. **278**(48): p. 48348-56.
53. Chen, Z., et al., *Cross-linking of C-terminal residues of phospholamban to the Ca2+ pump of cardiac sarcoplasmic reticulum to probe spatial and functional interactions within the transmembrane domain.* The Journal of biological chemistry, 2006. **281**(20): p. 14163-72.
54. Ambudkar, I.S. and A.E. Shamoo, *Role of phospholamban in regulating cardiac sarcoplasmic reticulum calcium pump.* Membrane biochemistry, 1984. **5**(2): p. 119-30.
55. Edes, I. and E.G. Kranias, *Regulation of cardiac sarcoplasmic reticulum function by phospholamban.* Membrane biochemistry, 1987. **7**(3): p. 175-92.
56. Cantilina, T., et al., *Comparative studies of cardiac and skeletal sarcoplasmic reticulum ATPases. Effect of a phospholamban antibody on enzyme activation by Ca2+.* J Biol Chem, 1993. **268**(23): p. 17018-25.
57. Chen, Z., B.L. Akin, and L.R. Jones, *Mechanism of reversal of phospholamban inhibition of the cardiac Ca2+-ATPase by protein kinase A and by anti-phospholamban monoclonal antibody 2D12.* J Biol Chem, 2007. **282**(29): p. 20968-76.
58. James, P., et al., *Nature and site of phospholamban regulation of the Ca2+ pump of sarcoplasmic reticulum.* Nature, 1989. **342**(6245): p. 90-2.
59. Negash, S., et al., *Phospholamban remains associated with the Ca2+- and Mg2+-dependent ATPase following phosphorylation by cAMP-dependent protein kinase.* Biochem J, 2000. **351**(Pt 1): p. 195-205.
60. Gruber, S.J., et al., *Phospholamban mutants compete with wild type for SERCA binding in living cells.* Biochem Biophys Res Commun, 2012.
61. James, Z.M., et al., *Protein-protein interactions in calcium transport regulation probed by saturation transfer electron paramagnetic resonance.* Biophys J, 2012. **103**(6): p. 1370-8.
62. Schmidt, U., et al., *Human heart failure: cAMP stimulation of SR Ca(2+)-ATPase activity and phosphorylation level of phospholamban.* The American journal of physiology, 1999. **277**(2 Pt 2): p. H474-80.

63. Lindner, M., E. Erdmann, and D.J. Beuckelmann, *Calcium content of the sarcoplasmic reticulum in isolated ventricular myocytes from patients with terminal heart failure.* Journal of molecular and cellular cardiology, 1998. **30**(4): p. 743-9.
64. Kargacin, M.E. and G.J. Kargacin, *The sarcoplasmic reticulum calcium pump is functionally altered in dystrophic muscle.* Biochimica et biophysica acta, 1996. **1290**(1): p. 4-8.
65. Divet, A. and C. Huchet-Cadiou, *Sarcoplasmic reticulum function in slow- and fast-twitch skeletal muscles from mdx mice.* Pflugers Archiv : European journal of physiology, 2002. **444**(5): p. 634-43.
66. Park, S.W., et al., *Sarco(endo)plasmic reticulum Ca2+-ATPase 2b is a major regulator of endoplasmic reticulum stress and glucose homeostasis in obesity.* Proceedings of the National Academy of Sciences, 2010. **107**(45): p. 19320-5.
67. Belke, D.D. and W.H. Dillmann, *Altered cardiac calcium handling in diabetes.* Current hypertension reports, 2004. **6**(6): p. 424-9.
68. Del Monte, F., et al., *Abrogation of ventricular arrhythmias in a model of ischemia and reperfusion by targeting myocardial calcium cycling.* Proceedings of the National Academy of Sciences, 2004. **101**(15): p. 5622-7.
69. Goonasekera, S.A., et al., *Mitigation of muscular dystrophy in mice by SERCA overexpression in skeletal muscle.* The Journal of clinical investigation, 2011. **121**(3): p. 1044-52.
70. Trost, S.U., et al., *Overexpression of the sarcoplasmic reticulum Ca(2+)-ATPase improves myocardial contractility in diabetic cardiomyopathy.* Diabetes, 2002. **51**(4): p. 1166-71.
71. Zsebo, K., et al., *Long-term effects of AAV1/SERCA2a gene transfer in patients with severe heart failure: analysis of recurrent cardiovascular events and mortality.* Circulation research, 2014. **114**(1): p. 101-8.
72. Greenberg, B., et al., *Design of a phase 2b trial of intracoronary administration of AAV1/SERCA2a in patients with advanced heart failure: the CUPID 2 trial (calcium up-regulation by percutaneous administration of gene therapy in cardiac disease phase 2b).* JACC. Heart failure, 2014. **2**(1): p. 84-92.
73. Jessup, M., et al., *Calcium Upregulation by Percutaneous Administration of Gene Therapy in Cardiac Disease (CUPID): a phase 2 trial of intracoronary gene therapy of sarcoplasmic reticulum Ca2+-ATPase in patients with advanced heart failure.* Circulation, 2011. **124**(3): p. 304-13.
74. Jaski, B.E., et al., *Calcium upregulation by percutaneous administration of gene therapy in cardiac disease (CUPID Trial), a first-in-human phase 1/2 clinical trial.* Journal of cardiac failure, 2009. **15**(3): p. 171-81.
75. Pfeifer, A. and I.M. Verma, *Gene therapy: promises and problems.* Annual review of genomics and human genetics, 2001. **2**: p. 177-211.
76. Muller, O.J., H.A. Katus, and R. Bekeredjian, *Targeting the heart with gene therapy-optimized gene delivery methods.* Cardiovascular research, 2007. **73**(3): p. 453-62.

77. Luo, W., et al., *Targeted ablation of the phospholamban gene is associated with markedly enhanced myocardial contractility and loss of beta-agonist stimulation.* Circulation research, 1994. **75**(3): p. 401-9.
78. Zhang, T., et al., *Phospholamban ablation rescues sarcoplasmic reticulum Ca(2+) handling but exacerbates cardiac dysfunction in CaMKIIdelta(C) transgenic mice.* Circulation research, 2010. **106**(2): p. 354-62.
79. Janczewski, A.M., et al., *Phospholamban gene ablation improves calcium transients but not cardiac function in a heart failure model.* Cardiovascular research, 2004. **62**(3): p. 468-80.
80. Lockamy, E.L., et al., *Functional and physical competition between phospholamban and its mutants provides insight into the molecular mechanism of gene therapy for heart failure.* Biochem Biophys Res Commun, 2011. **408**(3): p. 388-92.
81. Schmitt, J.P., et al., *Dilated cardiomyopathy and heart failure caused by a mutation in phospholamban.* Science, 2003. **299**(5611): p. 1410-3.
82. Ha, K.N., et al., *Lethal Arg9Cys phospholamban mutation hinders Ca2+-ATPase regulation and phosphorylation by protein kinase A.* Proceedings of the National Academy of Sciences, 2011. **108**(7): p. 2735-40.
83. Minamisawa, S., et al., *Mutation of the phospholamban promoter associated with hypertrophic cardiomyopathy.* Biochemical and biophysical research communications, 2003. **304**(1): p. 1-4.
84. Cornea, R.L., S.J. Gruber, E.L. Lockamy, J.M. Muretta, D. Jin, J. Chen, R. Dahl, T. Bartfai, K.M. Zsebo, G.D. Gillespie, and D.D. Thomas, *High-throughput FRET assay yields allosteric SERCA activators.* J Biomol Screen, 2013. **18**(1): p. 97-107.
85. Gruber, S.J., et al., *Discovery of enzyme modulators via high-throughput time-resolved FRET in living cells.* Journal of biomolecular screening, 2014. **19**(2): p. 215-22.
86. Likhtenshtein, G.I., *Spin labeling methods in molecular biology*1976: Wiley.
87. Altenbach, C., et al., *Structural studies on transmembrane proteins. 2. Spin labeling of bacteriorhodopsin mutants at unique cysteines.* Biochemistry, 1989. **28**(19): p. 7806-12.
88. Altenbach, C., et al., *Transmembrane protein structure: spin labeling of bacteriorhodopsin mutants.* Science, 1990. **248**(4959): p. 1088-92.
89. Kusnetzow, A.K., C. Altenbach, and W.L. Hubbell, *Conformational states and dynamics of rhodopsin in micelles and bilayers.* Biochemistry, 2006. **45**(17): p. 5538-50.
90. Arata, T., et al., *Orientation and motion of myosin light chain and troponin in reconstituted muscle fibers as detected by ESR with a new bifunctional spin label.* Advances in experimental medicine and biology, 2003. **538**: p. 279-83; discussion 284.
91. Beth, A.H., et al., *Dynamics and interactions of the anion channel in intact human erythrocytes: an electron paramagnetic resonance spectroscopic study*

employing a new membrane-impermeant bifunctional spin-label. Biochemistry, 1986. **25**(13): p. 3824-32.
92. Thompson, A.R., et al., *Structural dynamics of the actomyosin complex probed by a bifunctional spin label that cross-links SH1 and SH2.* Biophysical journal, 2008. **95**(11): p. 5238-46.
93. Fleissner, M.R., et al., *Structure and dynamics of a conformationally constrained nitroxide side chain and applications in EPR spectroscopy.* Proceedings of the National Academy of Sciences, 2011. **108**(39): p. 16241-6.
94. Moen, R.J., D.D. Thomas, and J.C. Klein, *Conformationally trapping the actin-binding cleft of myosin with a bifunctional spin label.* The Journal of biological chemistry, 2013. **288**(5): p. 3016-24.
95. Mello, R.N. and D.D. Thomas, *Three distinct actin-attached structural states of myosin in muscle fibers.* Biophysical journal, 2012. **102**(5): p. 1088-96.
96. Marchetto, R., S. Schreier, and C.R. Nakaie, *A Novel Spin-Labeled Amino-Acid Derivative for Use in Peptide-Synthesis - (9-Fluorenylmethyloxycarbonyl)-2,2,6,6-Tetramethylpiperidine-N-Oxyl-4-Amino-4-Carboxylic Acid.* Journal of the American Chemical Society, 1993. **115**(23): p. 11042-11043.
97. Toniolo, C., et al., *Synthesis and conformational studies of peptides containing TOAC, a spin-labelled C alpha, alpha-disubstituted glycine.* Journal of peptide science : an official publication of the European Peptide Society, 1995. **1**(1): p. 45-57.
98. Karim, C.B., Z. Zhang, and D.D. Thomas, *Synthesis of TOAC spin-labeled proteins and reconstitution in lipid membranes.* Nat Protoc, 2007. **2**(1): p. 42-9.
99. Zeeman, P., *On the Influence of Magnetism on the Nature of the Light Emitted by a Substance.* ApJ, 1897. **5**.
100. Griffiths, D.J., *Introduction to quantum mechanics*. 2005: Pearson Prentice Hall.
101. Fajer, P.G., *Electron Spin Resonance Spectroscopy Labeling in Peptide and Protein Analysis*, in *Encyclopedia of Analytical Chemistry: Applications, Theory, and Instrumentation*, R.A. Meyers, Editor 2000, Wiley.
102. Copeland, J.A., *Theoretical Study of a Gunn Diode in a Resonant Circuit.* IEEE Trans. Electron Devices, 1967. **14**(2): p. 55-58.
103. Lakowicz, J.R., *Principles of Fluorescence Spectroscopy.* 2007: Springer.
104. Ghimire, H., et al., *Probing the helical tilt and dynamic properties of membrane-bound phospholamban in magnetically aligned bicelles using electron paramagnetic resonance spectroscopy.* Biochim Biophys Acta, 2012. **1818**(3): p. 645-50.
105. Zavoisky, E., *Paramagnetic relaxation of liquid solutions for perpendicular fields.* J. Phys. USSR, 1945. **9**: p. 211.
106. Nesmelov, Y.E., et al., *Rotational dynamics of phospholamban determined by multifrequency electron paramagnetic resonance.* Biophysical journal, 2007. **93**(8): p. 2805-12.
107. Inbaraj, J.J., N.A. Nusair, and G.A. Lorigan, *Investigating magnetically aligned phospholipid bilayers with EPR spectroscopy at Q-band (35 GHz): optimization*

and comparison with X-band (9 GHz). Journal of magnetic resonance, 2004. **171**(1): p. 71-9.
108. Smirnova, T.I., et al., *W-Band (95 GHz) EPR Spectroscopy of Nitroxide Radicals with Complex Proton Hyperfine Structure: Fast Motion.* The Journal of Physical Chemistry, 1995. **99**(22): p. 9008-9016.
109. Goldman, S.A., Bruno, G.V., and Freed, J.H., *Estimating Slow-Motional Rotational Correlation Times for Nitroxides by Electron Spin Resonance.* J Phys Chem, 1972. **76**(13): p. 1858-1860.
110. Berliner, L.J., *Spin labeling : theory and applications*. Molecular biology1976, New York: Academic Press.
111. Squier, T.C. and D.D. Thomas, *Methodology for increased precision in saturation transfer electron paramagnetic resonance studies of rotational dynamics.* Biophys J, 1986. **49**(4): p. 921-35.
112. Beth, A.H. and E.J. Hustedt, *Saturation Transfer EPR: Rotational Dynamics of Membrane Proteins*. Biomedical EPR-Part B: Methodology, Instrumentation, and Dynamics, ed. S.S. Eaton, G.R. Eaton, and L.J. Berliner. 2005, New York: Springer. 369-408.
113. Budil, D.E., et al., *Nonlinear-least-squares analysis of slow-motion EPR spectra in one and two dimensions using a modified Levenberg-Marquardt algorithm.* Journal of Magnetic Resonance Series A, 1996. **120**(2): p. 155-189.
114. Khairy, K., D. Budil, and P. Fajer, *Nonlinear-least-squares analysis of slow motional regime EPR spectra.* Journal of magnetic resonance, 2006. **183**(1): p. 152-9.
115. Bigelow, D.J. and G. Inesi, *Frequency-domain fluorescence spectroscopy resolves the location of maleimide-directed spectroscopic probes within the tertiary structure of the Ca-ATPase of sarcoplasmic reticulum.* Biochemistry, 1991. **30**(8): p. 2113-25.
116. Zamoon, J., et al., *NMR solution structure and topological orientation of monomeric phospholamban in dodecylphosphocholine micelles.* Biophys J, 2003. **85**(4): p. 2589-98.
117. Simmerman, H.K. and L.R. Jones, *Phospholamban: protein structure, mechanism of action, and role in cardiac function.* Physiol Rev, 1998. **78**(4): p. 921-47.
118. MacLennan, D.H., Y. Kimura, and T. Toyofuku, *Sites of regulatory interaction between calcium ATPases and phospholamban.* Ann N Y Acad Sci, 1998. **853**: p. 31-42.
119. Hasenfuss, G. and B. Pieske, *Calcium cycling in congestive heart failure.* J Mol Cell Cardiol, 2002. **34**(8): p. 951-69.
120. Lipskaia, L., et al., *Sarcoplasmic reticulum Ca(2+) ATPase as a therapeutic target for heart failure.* Expert Opin Biol Ther, 2010. **10**(1): p. 29-41.
121. Kaye, D.M., et al., *Percutaneous cardiac recirculation-mediated gene transfer of an inhibitory phospholamban peptide reverses advanced heart failure in large animals.* J Am Coll Cardiol, 2007. **50**(3): p. 253-60.

122. Mueller, B., et al., *Direct detection of phospholamban and sarcoplasmic reticulum Ca-ATPase interaction in membranes using fluorescence resonance energy transfer.* Biochemistry, 2004. **43**(27): p. 8754-65.
123. MacLennan, D.H., T. Toyofuku, and Y. Kimura, *Sites of regulatory interaction between calcium ATPases and phospholamban.* Basic Res Cardiol, 1997. **92 Suppl 1**: p. 11-5.
124. Mersol, J.V., et al., *Self-association accompanies inhibition of Ca-ATPase by thapsigargin.* Biophys J, 1995. **68**(1): p. 208-15.
125. Mahaney, J.E., et al., *Intermolecular interactions in the mechanism of skeletal muscle sarcoplasmic reticulum Ca(2+)-ATPase (SERCA1): evidence for a triprotomer.* Biochemistry, 2008. **47**(51): p. 13711-25.
126. Hidalgo, C., D.D. Thomas, and N. Ikemoto, *Effect of the lipid environment on protein motion and enzymatic activity of sarcoplasmic reticulum calcium ATPase.* J Biol Chem, 1978. **253**(19): p. 6879-87.
127. Squier, T.C. and D.D. Thomas, *Relationship between protein rotational dynamics and phosphoenzyme decomposition in the sarcoplasmic reticulum Ca-ATPase.* J Biol Chem, 1988. **263**(19): p. 9171-7.
128. Thomas, D.D., and C. Hidalgo, *Rotational motion of the sarcoplasmic reticulum Ca2+-ATPase.* Proc Natl Acad Sci U S A, 1978. **75**: p. 5488-5492.
129. Birmachu, W. and D.D. Thomas, *Rotational dynamics of the Ca-ATPase in sarcoplasmic reticulum studied by time-resolved phosphorescence anisotropy.* Biochemistry, 1990. **29**(16): p. 3904-14.
130. Horvath, L.I., et al., *Saturation transfer electron spin resonance of Ca2(+)-ATPase covalently spin-labeled with beta-substituted vinyl ketone- and maleimide-nitroxide derivatives. Effects of segmental motion and labeling levels.* Biophys J, 1990. **58**(1): p. 231-41.
131. Thomas, D.D., et al., *Rotational dynamics of protein and boundary lipid in sarcoplasmic reticulum membrane.* Biophys J, 1982. **37**(1): p. 217-25.
132. Napier, R.M., J.M. East, and A.G. Lee, *State of aggregation of the (Ca2+ + Mg2+)-ATPase studied using saturation-transfer electron spin resonance.* Biochim Biophys Acta, 1987. **903**(2): p. 365-73.
133. Saffman, P.G. and M. Delbruck, *Brownian motion in biological membranes.* Proc Natl Acad Sci U S A, 1975. **72**(8): p. 3111-3.
134. Voss, J., L.R. Jones, and D.D. Thomas, *The physical mechanism of calcium pump regulation in the heart.* Biophys J, 1994. **67**(1): p. 190-6.
135. Thomas, D.D., L.R. Dalton, and J.S. Hyde, *Rotational diffusion studied by passage saturation transfer electron paramagnetic resonance.* J Chem Phys, 1976. **65**: p. 3006-3024.
136. Thomas, D.D., *Rotational Diffusion of Membrane Proteins*, in *Techniques for the Analysis of Membrane Proteins*, R.J.C. C.I. Ragan, Editor 1986, Chapman and Hall: London.
137. Karim, C.B., et al., *Synthetic null-cysteine phospholamban analogue and the corresponding transmembrane domain inhibit the Ca-ATPase.* Biochemistry, 2000. **39**(35): p. 10892-7.

138. Eletr, S. and G. Inesi, *Phospholipid orientation in sarcoplasmic membranes: spin-label ESR and proton NMR studies.* Biochim Biophys Acta, 1972. **282**(1): p. 174-9.
139. Coll, R.J. and A.J. Murphy, *Purification of the CaATPase of sarcoplasmic reticulum by affinity chromatography.* J Biol Chem, 1984. **259**(22): p. 14249-54.
140. Reddy, L.G., et al., *Defining the molecular components of calcium transport regulation in a reconstituted membrane system.* Biochemistry, 2003. **42**(15): p. 4585-92.
141. Levy, D., et al., *Reconstitution of the sarcoplasmic reticulum Ca(2+)-ATPase: mechanisms of membrane protein insertion into liposomes during reconstitution procedures involving the use of detergents.* Biochim Biophys Acta, 1992. **1107**(2): p. 283-98.
142. Thomas, D.D. and C. Hidalgo, *Rotational motion of the sarcoplasmic reticulum Ca2+-ATPase.* Proc Natl Acad Sci U S A, 1978. **75**(11): p. 5488-92.
143. Baroin, A., A. Bienvenue, and P.F. Devaux, *Spin-label studies of protein-protein interactions in retinal rod outer segment membranes. Saturation transfer electron paramagnetic resonance spectroscopy.* Biochemistry, 1979. **18**(7): p. 1151-5.
144. Karim, C.B., et al., *Role of cysteine residues in structural stability and function of a transmembrane helix bundle.* J Biol Chem, 2001. **276**(42): p. 38814-9.
145. Ablorh, N.A., et al., *Accurate quantitation of phospholamban phosphorylation by immunoblot.* Anal Biochem, 2012.
146. Mason, R.P. and J.H. Freed, *Estimating Microsecond Rotational Correlation Times from Lifetime Broadening of Nitroxide Electron Spin Resonance Spectra Near the Rigid Limit.* J Phys Chem, 1974. **78**(13): p. 1321-1323.
147. Scarpelli, F., et al., *Aggregation of transmembrane peptides studied by spin-label EPR.* J Phys Chem B, 2009. **113**(36): p. 12257-64.
148. Uhrikova, D., et al., *Small-angle neutron scattering study of the n-decane effect on the bilayer thickness in extruded unilamellar dioleoylphosphatidylcholine liposomes.* Biophys Chem, 2000. **88**(1-3): p. 165-70.
149. Cherry, R.J. and R.E. Godfrey, *Anisotropic rotation of bacteriorhodopsin in lipid membranes. Comparison of theory with experiment.* Biophys J, 1981. **36**(1): p. 257-76.
150. Howard, E.C., et al., *Simulation of saturation transfer electron paramagnetic resonance spectra for rotational motion with restricted angular amplitude.* Biophys J, 1993. **64**(3): p. 581-93.
151. Marsh, D., et al., *TOAC spin labels in the backbone of alamethicin: EPR studies in lipid membranes.* Biophys J, 2007. **92**(2): p. 473-81.
152. Marsh, D., *Saturation transfer EPR studies of slow rotational motion in membranes.* Appl Magn Reson, 2007. **31**: p. 387 - 410.
153. Hustedt, E.J. and A.H. Beth, *The sensitivity of saturation transfer electron paramagnetic resonance spectra to restricted amplitude uniaxial rotational diffusion.* Biophys J, 2001. **81**(6): p. 3156-65.

154. Fujii, J., et al., *Expression and site-specific mutagenesis of phospholamban. Studies of residues involved in phosphorylation and pentamer formation.* J Biol Chem, 1989. **264**(22): p. 12950-5.
155. Hughes, E., et al., *Probing the oligomeric state of phospholamban variants in phospholipid bilayers from solid-state NMR measurements of rotational diffusion rates.* Biochemistry, 2005. **44**(10): p. 4055-66.
156. Reddy, L.G., L.R. Jones, and D.D. Thomas, *Depolymerization of phospholamban in the presence of calcium pump: a fluorescence energy transfer study.* Biochemistry, 1999. **38**(13): p. 3954-62.
157. Yao, Q., et al., *Oligomeric interactions between phospholamban molecules regulate Ca-ATPase activity in functionally reconstituted membranes.* Biochemistry, 2001. **40**(21): p. 6406-13.
158. Mahaney, J.E., J.P. Froehlich, and D.D. Thomas, *Conformational transitions of the sarcoplasmic reticulum Ca-ATPase studied by time-resolved EPR and quenched-flow kinetics.* Biochemistry, 1995. **34**(14): p. 4864-79.
159. Mahaney, J.E., et al., *Phospholamban inhibits Ca2+ pump oligomerization and intersubunit free energy exchange leading to activation of cardiac muscle SERCA2a.* Ann N Y Acad Sci, 2003. **986**: p. 338-40.
160. Froehlich, J.P., et al., *Complex kinetic behavior in the Na,K- and Ca-ATPases. Evidence for subunit-subunit interactions and energy conservation during catalysis.* Ann N Y Acad Sci, 1997. **834**: p. 280-96.
161. Squier, T.C., S.E. Hughes, and D.D. Thomas, *Rotational dynamics and protein-protein interactions in the Ca-ATPase mechanism.* J Biol Chem, 1988. **263**(19): p. 9162-70.
162. Voss, J., et al., *Effects of melittin on molecular dynamics and Ca-ATPase activity in sarcoplasmic reticulum membranes: time-resolved optical anisotropy.* Biochemistry, 1991. **30**(30): p. 7498-506.
163. Mahaney, J.E., et al., *Effects of melittin on lipid-protein interactions in sarcoplasmic reticulum membranes.* Biophys J, 1992. **63**(6): p. 1513-22.
164. Karon, B.S., et al., *Anesthetics alter the physical and functional properties of the Ca-ATPase in cardiac sarcoplasmic reticulum.* Biophys J, 1995. **68**(3): p. 936-45.
165. Cornea, R.L. and D.D. Thomas, *Effects of membrane thickness on the molecular dynamics and enzymatic activity of reconstituted Ca-ATPase.* Biochemistry, 1994. **33**(10): p. 2912-20.
166. Karon, B.S., J.E. Mahaney, and D.D. Thomas, *Halothane and cyclopiazonic acid modulate Ca-ATPase oligomeric state and function in sarcoplasmic reticulum.* Biochemistry, 1994. **33**(46): p. 13928-37.
167. Birmachu, W., et al., *Protein and lipid rotational dynamics in cardiac and skeletal sarcoplasmic reticulum detected by EPR and phosphorescence anisotropy.* Biochemistry, 1993. **32**(36): p. 9445-53.
168. Fujii, J., et al., *Co-expression of slow-twitch/cardiac muscle Ca2(+)-ATPase (SERCA2) and phospholamban.* FEBS Lett, 1990. **273**(1-2): p. 232-4.

169. Ram, P. and J.H. Prestegard, *Magnetic field induced ordering of bile salt/phospholipid micelles: new media for NMR structural investigations.* Biochimica et biophysica acta, 1988. **940**(2): p. 289-94.
170. Cho, G., B.M. Fung, and V.B. Reddy, *Phospholipid bicelles with positive anisotropy of the magnetic susceptibility.* Journal of the American Chemical Society, 2001. **123**(7): p. 1537-8.
171. Prosser, R.S., V.B. Volkov, and I.V. Shiyanovskaya, *Solid-state NMR studies of magnetically aligned phospholipid membranes: taming lanthanides for membrane protein studies.* Biochemistry and cell biology = Biochimie et biologie cellulaire, 1998. **76**(2-3): p. 443-51.
172. De Angelis, A.A. and S.J. Opella, *Bicelle samples for solid-state NMR of membrane proteins.* Nature Protocols, 2007. **2**(10): p. 2332-8.
173. Landau, E.M. and J.P. Rosenbusch, *Lipidic cubic phases: a novel concept for the crystallization of membrane proteins.* Proceedings of the National Academy of Sciences, 1996. **93**(25): p. 14532-5.
174. Shi, L., et al., *Tilt and azimuthal angles of a transmembrane peptide: a comparison between molecular dynamics calculations and solid-state NMR data of sarcolipin in lipid membranes.* Biophysical journal, 2009. **96**(9): p. 3648-62.
175. De Angelis, A.A., et al., *Structure determination of a membrane protein with two trans-membrane helices in aligned phospholipid bicelles by solid-state NMR spectroscopy.* Journal of the American Chemical Society, 2006. **128**(37): p. 12256-67.
176. Inbaraj, J.J., et al., *Determining the topology of integral membrane peptides using EPR spectroscopy.* Journal of the American Chemical Society, 2006. **128**(29): p. 9549-54.
177. Garber, S.M., G.A. Lorigan, and K.P. Howard, *Magnetically oriented phospholipid bilayers for spin label EPR studies.* Journal of the American Chemical Society, 1999. **121**(13): p. 3240-3241.
178. Lu, J.X., M.A. Caporini, and G.A. Lorigan, *The effects of cholesterol on magnetically aligned phospholipid bilayers: a solid-state NMR and EPR spectroscopy study.* Journal of Magnetic Resonance, 2004. **168**(1): p. 18-30.
179. Caporini, M.A., et al., *Investigating magnetically aligned phospholipid bilayers with various lanthanide ions for X-band spin-label EPR studies.* Biochimica et biophysica acta, 2003. **1612**(1): p. 52-8.
180. Harroun, T.A., et al., *Comprehensive examination of mesophases formed by DMPC and DHPC mixtures.* Langmuir : the ACS journal of surfaces and colloids, 2005. **21**(12): p. 5356-61.
181. Cardon, T.B., E.K. Tiburu, and G.A. Lorigan, *Magnetically aligned phospholipid bilayers in weak magnetic fields: optimization, mechanism, and advantages for X-band EPR studies.* Journal of Magnetic Resonance, 2003. **161**(1): p. 77-90.
182. Nieh, M.P., et al., *Structural phase behavior of high-concentration, alignable biomimetic bicelle mixtures.* Macromolecular Symposia, 2004. **219**: p. 135-145.

183. Bigelow, D.J., T.C. Squier, and D.D. Thomas, *Temperature dependence of rotational dynamics of protein and lipid in sarcoplasmic reticulum membranes*. Biochemistry, 1986. **25**(1): p. 194-202.
184. Cho, H.S., J.L. Dominick, and M.M. Spence, *Lipid domains in bicelles containing unsaturated lipids and cholesterol.* The journal of physical chemistry. B, 2010. **114**(28): p. 9238-45.
185. Lin, A.Y., et al., *Large-scale opening of utrophin's tandem CH domains upon actin binding, by an induced-fit mechanism.* Proc Natl Acad Sci U S A, 2011: p. accepted.
186. Durer, Z.A., et al., *Structural states and dynamics of the D-loop in actin.* Biophysical journal, 2012. **103**(5): p. 930-9.
187. Gaffney, B.J.M., H. M., *The Paramagnetic Resonance Spectra of Spin Labels in Phospholipid Membranes.* Journal of Magnetic Resonance, 1974. **16**(1): p. 1-28.
188. Schneider, D.J.F., J. H., *Calculating Slow Motional Magnetic Resonance Spectra*. Biological Magnetic Resonance, ed. L.J.R. Berliner, J. Vol. 8. 1989, New York: Springer US.
189. Cardon, T.B., et al., *Magnetically aligned phospholipid bilayers at the parallel and perpendicular orientations for X-band spin-label EPR studies.* J Am Chem Soc, 2001. **123**(12): p. 2913-4.
190. Lau, T.L., et al., *Structure of the integrin beta3 transmembrane segment in phospholipid bicelles and detergent micelles.* Biochemistry, 2008. **47**(13): p. 4008-16.
191. Vostrikov, V.V., et al., *Structural dynamics and topology of phosphorylated phospholamban homopentamer reveal its role in the regulation of calcium transport.* Structure, 2013. **21**(12): p. 2119-30.
192. Cardon, T.B., et al., *Magnetically aligned phospholipid bilayers at the parallel and perpendicular orientations for X-band spin-label EPR studies.* Journal of the American Chemical Society, 2001. **123**(12): p. 2913-4.
193. Ghimire, H., et al., *Probing the helical tilt and dynamic properties of membrane-bound phospholamban in magnetically aligned bicelles using electron paramagnetic resonance spectroscopy.* Biochimica et biophysica acta, 2012. **1818**(3): p. 645-50.
194. Storm, A.R., et al., *Incorporation of a Rigid TOAC Spin-Label as a Non-Native Amino Acid into a Full-Length Protein by In Vitro Translation using Amber Codon Suppression.* Biophysical journal, 2013. **104**(2): p. 343a-343a.
195. Moen, R.J., D.D. Thomas, and J.C. Klein, *Conformationally trapping the actin-binding cleft of myosin with a bifunctional spin label.* J Biol Chem, 2013. **288**(5): p. 3016-24.
196. Thompson, A.R., et al., *Structural dynamics of the actomyosin complex probed by a bifunctional spin label that cross-links SH1 and SH2.* Biophys J, 2008. **95**(11): p. 5238-46.
197. Mello, R.N. and D.D. Thomas, *Three distinct actin-attached structural states of myosin in muscle fibers.* Biophys J, 2012. **102**(5): p. 1088-96.

198. Sahu, I.D., et al., *DEER EPR measurements for membrane protein structures via bifunctional spin labels and lipodisq nanoparticles.* Biochemistry, 2013. **52**(38): p. 6627-32.
199. Li, Q., et al., *Structural basis of lipid-driven conformational transitions in the KvAP voltage-sensing domain.* Nat Struct Mol Biol, 2014. **21**(2): p. 160-6.
200. MacLennan, D.H. and E.G. Kranias, *Phospholamban: a crucial regulator of cardiac contractility.* Nature reviews, 2003. **4**(7): p. 566-77.
201. Mascioni, A., et al., *Solid-state NMR and rigid body molecular dynamics to determine domain orientations of monomeric phospholamban.* Journal of the American Chemical Society, 2002. **124**(32): p. 9392-3.
202. Buck, B., et al., *Overexpression, purification, and characterization of recombinant Ca-ATPase regulators for high-resolution solution and solid-state NMR studies.* Protein Expr Purif, 2003. **30**(2): p. 253-61.
203. Blommel, P.G. and B.G. Fox, *A combined approach to improving large-scale production of tobacco etch virus protease.* Protein Expr Purif, 2007. **55**(1): p. 53-68.
204. Douglas, J.L., et al., *Rapid, high-yield expression and purification of Ca2+-ATPase regulatory proteins for high-resolution structural studies.* Protein Expr Purif, 2005. **40**(1): p. 118-25.
205. Veglia, G., et al., *What can we learn from a small regulatory membrane protein?* Methods Mol Biol, 2010. **654**: p. 303-19.
206. Columbus, L., et al., *Molecular motion of spin labeled side chains in alpha-helices: analysis by variation of side chain structure.* Biochemistry, 2001. **40**(13): p. 3828-46.
207. Traaseth, N.J., et al., *Structural dynamics and topology of phospholamban in oriented lipid bilayers using multidimensional solid-state NMR.* Biochemistry, 2006. **45**(46): p. 13827-34.
208. Nesmelov, Y.E., et al., *Rotational dynamics of phospholamban determined by multifrequency electron paramagnetic resonance.* Biophys J, 2007. **93**(8): p. 2805-12.
209. Knol, J., K. Sjollema, and B. Poolman, *Detergent-mediated reconstitution of membrane proteins.* Biochemistry, 1998. **37**(46): p. 16410-5.
210. Ottiger, M. and A. Bax, *Characterization of magnetically oriented phospholipid micelles for measurement of dipolar couplings in macromolecules.* Journal of biomolecular NMR, 1998. **12**(3): p. 361-72.
211. Rowe, B.A. and S.L. Neal, *Fluorescence probe study of bicelle structure as a function of temperature: Developing it practical bicelle structure model.* Langmuir, 2003. **19**(6): p. 2039-2048.
212. Dong, X. and D.D. Thomas, *Time-resolved FRET reveals the structural mechanism of SERCA-PLB regulation.* Biochemical and biophysical research communications, 2014. **449**(2): p. 196-201.
213. Borchman, D., D. Tang, and M.C. Yappert, *Lipid composition, membrane structure relationships in lens and muscle sarcoplasmic reticulum membranes.* Biospectroscopy, 1999. **5**(3): p. 151-67.